GEORG-AUGUST-UNIVERSITÄT GÖTTINGEN

GGNB

Super-resolution of PSD95 remodelling during synaptic plasticity

Dissertation

for the award of the degree

“Doctor rerum naturalium”

of the Georg-August-Universität Göttingen

within the doctoral program **“Sensory and Motor Neuroscience”**

of the Georg-August University School of Science (GAUSS)

submitted by

Valérie Clavet-Fournier

Born in Gaspé, Québec, Canada, 15.01.1991

Göttingen, November 2020

Thesis Committee

Dr. Katrin Willig
Nanoscale Microscopy and Molecular Physiology of the Brain,
Max Planck Institute of Experimental Medicine

Prof. Siegrid Löwel
Systems Neuroscience
Institute for Zoology and Anthropology, University of Göttingen

Prof. Jeong Seop Rhee
Molecular Neurobiology
Max Planck Institute of Experimental Medicine

Members of the Examination Board

Prof. Fred Wolf
Theorectical Neurophysics
Max Planck Institute for Dynamics und Self-Organization

Dr. Oliver Schlüter
Molecular Neurobiology
European Neuroscience Institute Göttingen

Prof. Ralf Heinrich
Dept. of Cellular Neurobiology
University of Göttingen

Date of oral examination: 14th of January 2021

Abstract

Strengthening and weakening of synapses are a fundamental information processing unit within the neuronal circuit of the brain. It has been shown that the most abundant scaffold protein of the postsynaptic density (PSD), PSD95, undergoes structural remodeling during long-term potentiation (LTP). With superresolution microscopy techniques, it was recently shown that the nanoorganization of PSD95 often appears in clusters or perforations, which has been revealed in living mice using in vivo STED microscopy. Moreover, recent evidence suggests that also other synaptic proteins show a clustered nanoorganization and that pre- and postsynaptic proteins and glutamate AMPA receptors align in so-called nanocolumns trans-synaptically. However, the impact of these nanoorganization on synaptic strength as well as their changes after activity remains ellusive. Therefore, my project aims to investigate the remodeling of pre- and postsynaptic structures after chemical LTP induction using STED nanoscopy. I performed live-cell STED imaging of endogenous PSD95 assemblies for up to 2h after chemical LTP induction of CA1 hippocampal neurons to reveal the morphological changes of PSD95 organization at nanoscale resolution. Moreover, I explored the assembly of the active zone protein Bassoon and AMPA receptor nanodomains in correlation with structural changes of PSD95 assemblies after LTP in hippocampal culture neurons using immunohistochemistry and two-color STED microscopy. For different time-points, before and after LTP, I analyzed the area of PSD95, AMPA receptor and Bassoon assemblies. The shape of their nanoorganization was analyzed qualitatively by classification of different shapes of protein assemblies and quantitatively by calculating a filling factor of these proteins per synapse. My data shows that the PSD95 area undergoes an increase with a delay of 1h following LTP induction and that this change is accompanied by the formation of segmented 2 and later perforated PSD95. Furthermore, the area of PSD95 assembly increases simultaneously with AMPA receptor nanodomain and Bassoon assembly. Bassoon assemblies show a similar shape as PSD95 organizations, and their remodeling is correlated after LTP induction. Finally, the increase of the number of AMPA receptor nanodomain is correlated with the formation of perforated and segmented 2 PSD95 2h following LTP stimulation and as well with the activation of silent synapses. Therefore, remodeling of PSD95 is accompanied by an increase of the number and the area of AMPA receptor cluster, as well as an increase of the area of Bassoon assembly. Thus, those results suggest that the structural plasticity of PSD95 is an important feature to improve the synaptic strength of the synapse.

Acknowledgments

The work of my thesis would not have been possible without the support and help of many great people that I would like to thank.

First of all, I would like to thank my supervisor Katrin Willig for giving me the chance to achieve my Ph.D. in your group. Thank you for taking the time to show me the physics of STED microscopy, bringing new ideas, continuously helping me to improve myself and my work, and supporting me during these 3 years. You helped me grow and become a good scientist.

I would also like to thank the members of my thesis committee, Jeong Seop Rhee and Siegrid Löwel, for their good ideas and the orientation of my project. It was really helpful. I would like to thank my collaborators, ChungKu Lee and Erinn Gideons. Thank you for helping me with the mEPSC experiments and for your good advice. A special mention for Erinn Gideons, thank you so much for helping me improve my English writing! I want also to thank the Nanoscale Microscopy and Molecular Physiology of the Brain (CNMPB), the Graduate Center for Neurosciences, Biophysics, and Molecular Biosciences (GGNB), my doctoral program Sensory and Motor Neuroscience, SFB889 and Tobias Moser for the financial support.

Furthermore, I would like to thank my colleague Waja Wegner for always being there for me, answering all my questions, sharing your knowledge, and helping me improve the experimental design for my experiments. Finally, thank you for guiding me to become a good scientist. I would like to thank my colleagues Joris van Dort, Antonia Müller, and Alexander Charles Mott for showing me the techniques used and for the good times and discussions in the office. I would like to thank Heinz Steffens for showing me how to do a craniotomy on a living mouse. I want also to thank my friends, especially Heba Ali, Anouk Meeuwissen, and Sofia Eliza Rova, for helping me with the corrections of the thesis and, most importantly, for your constant support during these 3 years. A special mention for Heba Ali, thank you for taking the time to build a macro for my analysis, you saved me a lot of work! Finally, thank you so much to all of you that been there and for the nice discussions, I have learned a lot from you!

At last, I want to thank my family, my dear friend Chloé Juneau and Phillipp Tonch for mental support during the hard times and for always encouraging me and believing in me to achieve my goal.

Abbreviations

AAV	Adeno-associated viral particles
AC	Calcium/CaM sensitive adenyl cyclase
ACSF	Artificial cerebrospinal fluid
Aip1	Actin-interacting protein 1
AMPA	α-amino-3-hydroxy-5-methyl-4-isoxazolepropionic acid
ANCOVA	Analysis of covariance
ANOVA	Analysis of variance
APV	*D-2-amino-5-phosphonovaleric acid*
Arp2/3	Actin Related Protein 2/3
AZ	Active Zone
CA1	*Cornu ammonis* 1
Ca^{2+}	Calcium
CA3	*Cornu ammonis* 3
CaM	Calcium sensor calmodulin
CaMKII	Calcium/calmodulin-dependent protein kinase II
cAMP	Cyclic Adenosine Monophosphate
CI	Confidence interval
CO_2	Carbon dioxide
CREB	cAMP response element-binding protein
DG	Dentate gyrus
DIO	Double inverted open reading frames
DIV	Days *in vitro*
EC	Entorhinal cortex
ELKS	Protein rich in the amino acids E, L, K and S
E-LTP	Early-LTP
EM	Electron microscopy
EPSC	Excitatory post synaptic current
ERK	Extracellular signal-regulated kinases
F-actin	Actin filament
FingR	Fibronectin intrabodies generated with mRNA
FWHM	Full width at half maximum
GKAP	Guanylate kinase-associated protein
GuK	Guanylate kinase
hSyn	human synapsin-1 promoter
IEG	Immediate early genes
K^+	Potassium
K-S	Kolmogorov-Smirnov
K-W	Mann-Whitney
LDLR	Low density lipoprotein receptor
L-LTP	Late-LTP
LTP	Long-term potentiation
MAGUKs	Membrane-associated guanylate kinase
MAPK	Mitogen-activated protein kinase

mEPSC	miniature excitatory postsynaptic currents
MF	Mossy fiber
Munc13	Mammalian uncoordinated-13
M-W	Mann-Whitney
myr	Myristoylation motif
Na^{2+}	Sodium
NMDA	N-methyl-D-aspartate
NT	Neurotransmitters
O_2	Oxygen
PALM	Photoactivation localization microscopy
PBS	Phosphate buffered saline
PFA	Paraformaldehyde
PKA	Protein kinase A
PKMζ	Protein kinase M zeta
Pr	Probability of neurotransmitter release
PSC	Postsynaptic current
PSD	Postsynaptic density
PSD93	Postsynaptic density 93
PSD95	Postsynaptic density 95
PSF	Point-spread function
Q	Quantal amplitude
rAAV	recombinant adeno associated virus
RESOLFT	Reversible saturable optical fluorescence transition
RIM	Rab3-interacting molecule
RIM-BP	RIM-Binding Protein
RNAi	Ribonucleic acid interference
rs	reversible photoswitchable
SAP102	Synapse-associated protein 90
SC	Schaffer collaterals
SD	Standard deviation
SEM	Standard deviation of the mean
SER	Smooth endoplasmic reticulum
SH3	Src-homology-3
Shank	SH3 domain and ankyrin repeat-containing protein
SM	Sec1/Munc18-like
SNAREs	Soluble *N*-ethylmaleimide-sensitive factor attached protein receptor
STED	Stimulated Emission Depletion Microscopy
STORM	Stochastic optical reconstruction microscopy
SUB	Subiculum
SV	Synaptic vesicles
SynGAP	Ras/Rap GTPase-activation protein GAP
t286	Threonine 286
TARPs	Transmembrane AMPA receptor regulatory proteins
TTX	Tetrodotoxin
VGCCs	Voltage-gated calcium channels
α-liprin	Liprin-alpha-1

Contents

1.Introduction

1.1 Memory via hippocampus

One of the most unique features of the brain is its ability to store information in the form of long-lasting memories. For centuries, humankind sought to understand how memory is encoded in the brain in a quest that started approximately 2000 years ago and is still ongoing. Particularly, the study of memory began when Aristotle published in his treatise "On the soul" that every human being is born without any knowledge and that he/she is the summation of his/her own experiences (Aristotle, 1994). Hence, it is the sensory and cognitive experiences that allow the encoding of information in memory and, in the same time, make an individual unique.

A key player in the formation of new memories, the hippocampus, was discovered by Scoville and Milner in 1957. They describe severe memory loss following lesions of the hippocampal region, an integral part of the limbic system. Nowadays, this region of the brain is well known to be involved in declarative and spatial memory (O'Keefe & Dostrovsky, 1971; Squire, 1992). To ensure its role, the hippocampus possesses a well-organized structure that is divided into three major subregions based on the cell types, connectivity, and anatomical location, namely, dentate gyrus (DG), *cornu ammonis* (CA) 3 and CA1 (Figure 1.1). The neural circuit between those three major subregions is organized as a tri-synaptic loop where sensory information comes in and out through the entorhinal cortex (EC). The perforant path and subiculum are two other sub-regions of the hippocampus important for the exchange of the information through EC. Precisely, the entorhinal cortex relays the sensory information to the DG through the perforant path (Figure 1.1). Afterwards, perforant path axons connect with the granule cells of the dentate gyrus where the information is relayed to the pyramidal cells of the CA3 by the mossy fibers and then to the CA1 pyramidal cells by the Schaffer collaterals (Figure 1.1) (Lavenex & Amaral, 2000; Ramón & Cajal, 1934). The trisynaptic loop of the hippocampus end when the information from the CA1 pyramidal cells, through the subiculum, re-enter the entorhinal cortex, where the initial sensory input comes from. Finally, after being processed by the hippocampus, the information returns to the sensory cortex via the communication of the entorhinal cortex with different associative neocortical areas (Lavenex & Amaral, 2000)

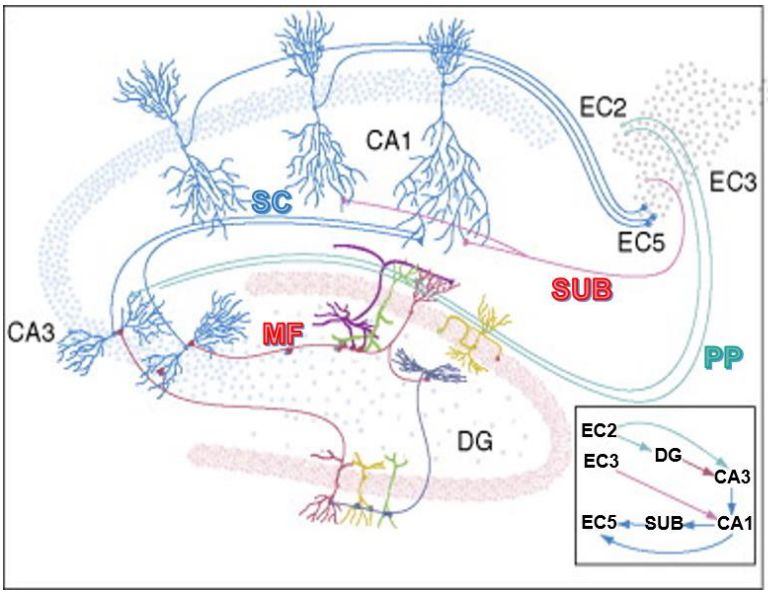

Figure 1.1 Neural circuit of the hippocampus: The entorhinal cortex (EC) relays information to the dentate gyrus (DG) via the perforant path (PP). DG connects with the pyramidal neurons of CA3 through the mossy fiber (MF) pathway and then to CA1 by the Schaffer collaterals (SC). (4) Finally, the information comes back to the EC via the subiculum (SUB). Image adapted from Li, Mu, & Gage, 2009.

The pyramidal neurons of the hippocampus play an important role in neural communication They can connect up to 10,000 other neurons via electrochemical signaling with their highly developed dendritic arborizations (Kennedy, 2016). In the hippocampus, to relay the information after a sensory experience, the neurons in the network must be electrically excited. The dendrites, via their small protrusions called dendritic spines, are responsible for carrying the current to the cell body. This process is triggered by the opening of sodium (Na^{2+}) and potassium (K^{+}) voltage-gated ion channels during depolarization of the dendritic membrane. When the voltage passes a specific threshold due to the influx of sodium, an action potential is transmitted along the dendrite to the soma (Golding & Spruston, 1998). Afterward, the current is summed at the axon initial segment located at the proximal part of the axon. When the axon initial segment reaches the threshold potential, an action potential is propagated along the axon that results in the release of neurotransmitter (Colbert & Johnston, 1996). Furthermore, when the action potential occurs repeatedly in the same neuron, there is an increase in the efficiency of synaptic transmission. The Canadian Donald Hebb (1949) described the strengthening of synaptic connections between neurons who fire together to be a key to memory formation (Hebb, 1949). In the hippocampus, the neurons engaged in the trisynaptic loop undergo structural and biochemical changes that will affect the efficiency of the synaptic transmission necessary for the learning and memory process (Izquierdo & Medina, 1997).

1.2 The synapse: the unit of communication

Brain function is controlled by synapses, which are the fundamental information processing units within the neuronal circuit. They are classified into two subtypes in the central nervous system: electrical and chemical synapses. In the hippocampus, the commonly found type is the chemical synapse. When two neurons are connected via a chemical synapse, the electrical activity generated in the first neuron is converted at the level of the synapse to a chemical signal by release of chemical messengers called neurotransmitters (NT). When neurotransmitters are released by the first neuron, they activate surface receptors on the second neuron leading to transmission of the signal (Nagatsu, Mogi, Ichinose, & Togari, 2000). To fulfill its role, the synapse is composed of three distinctive parts: a presynaptic element, which corresponds to the membrane of the axon terminal, a synaptic cleft, which is an inter-synaptic space of ~20nm, and a postsynaptic site mainly found on the dendritic spine of the adjacent neuron (Figure 1.2.A) (T. Schikorski & Stevens, 1999).

Chemical synapses can be excitatory or inhibitory. Excitatory via membrane depolarization, opening of sodium voltage-gated ion channels and generation of action potential, or inhibitory by opening of potassium and chloride channels which produce the hyperpolarization of the membrane (Hartzell, 1981). In the context of learning and memory, the major role for the flow of information is played by excitatory synapses that depend on glutamatergic transmission. In this process, the neurotransmitter glutamate is synthesized and stored into synaptic vesicles in the presynaptic bouton of the axon terminal (Figure 1.2). Following an action potential, the voltage-sensitive calcium channels open and allow the calcium ions (Ca^{2+}) to flow into the cell. The calcium ions then lead the vesicles to fuse with the presynaptic membrane and release the glutamates they carry in the synaptic cleft (Shin, Xu, Rizo, & Südhof, 2009; Südhof & Rizo, 2011).

On the other side of the synapse, we find the postsynaptic area which is characterized by an electron-dense region (observed with electron microscopy) due to the presence of multiple receptors, scaffold proteins, and synaptic proteins creating the postsynaptic density (PSD) (Figure 1.2.B). After the release of glutamate in the synaptic cleft, specific ionotropic glutamate receptors located in the PSD can be activated such as α-

amino-3-hydroxy-5-methyl-4-isoxazolepropionic acid (AMPA) receptors and N-methyl-D-aspartate (NMDA) receptors. Their activation allows calcium and sodium ions to enter the cell and activate signaling proteins important for the storage of information through long-lasting modifications of the postsynaptic structure and molecular composition. After being released from their receptors, the glutamate molecules are recycled and/or degraded by the presynaptic compartment or by a neighboring astrocyte.

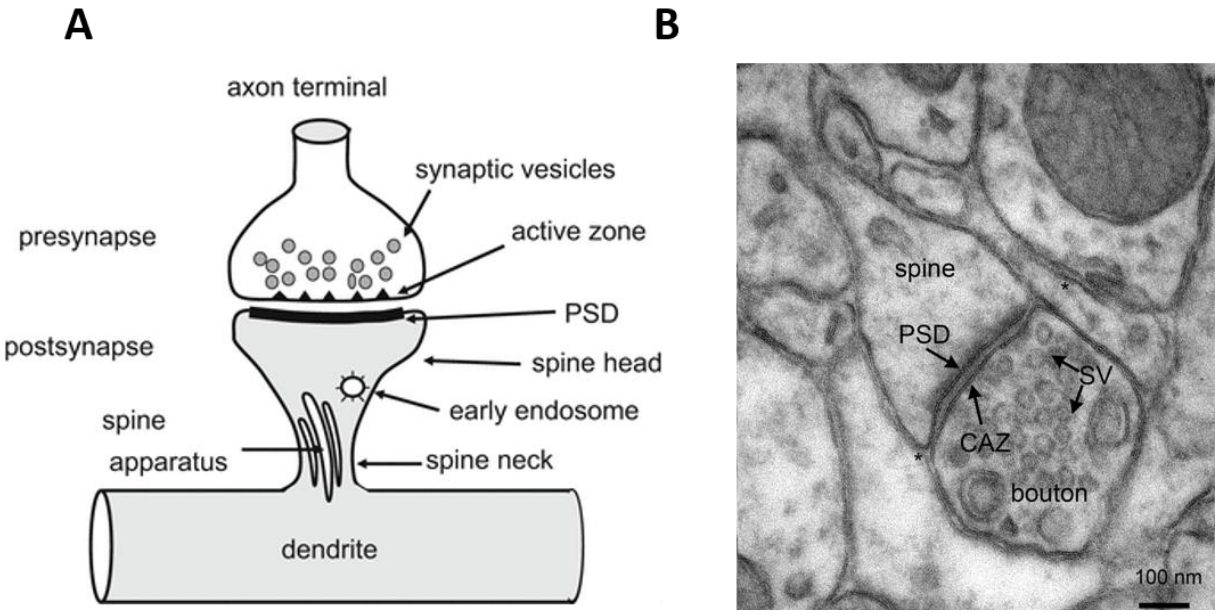

Figure 1.2 The excitatory synapse. (A) The structure of an excitatory synapse. The presynaptic compartment corresponds to the axon terminal of the neuron. The synaptic vesicles are filled with neurotransmitters and can fuse with the presynaptic membrane of the active zone for the release of neurotransmitters upon an action potential. The postsynaptic compartment is mostly located on the spine head of the dendritic spine. The postsynaptic density (PSD) is juxtaposed in front of the active zone for activation of receptors after neurotransmitter release. The postsynaptic spine contains an early endosome for the endocytosis of receptors and lipids from the plasma membrane. The mature spine can also include a spine apparatus, which is a stack of endoplasmic reticulum located in the spine neck. Adapted from (Iwasaki, Tanaka, & Okabe, 2016). **(B)** Electron microscopy image of an excitatory synapse. The PSD contains several ionotropic receptors, scaffold, and signaling proteins that form an electron dense-region. The presynaptic bouton is filled with synaptic vesicles (SV), some of which are docked at the active zone (CAZ) for the release of neurotransmitters. Adapted from Dieterich & Kreutz, 2016.

1.3 The presynapse

In the presynaptic compartment of the synapse, the transfer of information is regulated by the vesicle release and the molecular organization of the presynaptic proteins. These vesicles, ~ 40 nm in diameter, can cluster in the presynaptic terminal in three distinct pools: “the recycling pool” which proceed to exocytosis following a moderate stimulation; "the readily releasable pool" which correspond to a fraction of recycling pool docked at the plasma membrane where the vesicles fuse to release NT and "the

reserve pool" which cannot be released even upon a strong stimulation (Figure 1.3) (De Robertis, E D and Bennett, 1955; GRAY, 1959; PALAY, 1956; Rizzoli & Betz, 2005). Historically, the efficiency of the neurotransmission relies on the quantity of neurotransmitters released at the presynapse (Fatt and Katz, 1951, Del Castillo and Katz 1954). However, it is now well known that postsynaptic ionotropic glutamate receptors also influence neuronal transmission efficiency (section 1.5). Katz introduced the quantal hypothesis, where he stipulated that the postsynaptic current (PSC) depends on the probability of neurotransmitter release (Pr) combined with the number of activated synapses (N) and the quantal amplitude (Q) which was defined as the quantity of neurotransmitter released by one vesicle. To define the strength of the postsynaptic response from the presynaptic event, he developed the equation: PSC = Q * Pr * N (del Castillo & Katz, 1954; Fatt & Katz, 1951). Therefore, the recruitment of the vesicles near the release site and their fusion with the presynaptic plasma membrane are two crucial steps to trigger neuronal communication.

1.3.1 The active zone

The active zone (AZ) is the area where vesicles fuse with the plasma membrane to release the neurotransmitter into the synaptic cleft (Figure 1.2). This zone has four main functions in the NT release process. First of all, before being released, the vesicles need to be recruited near the AZ. This mechanism is termed docking and is mediated by a large complex composed of five core proteins of the active zone: Rab3-interacting molecule (RIM), Mammalian uncoordinated-13 (Munc13), RIM-Binding Protein (RIM-BP), Liprin-alpha-1 (α-liprin), and protein rich in the amino acids E, L, K and S (ELKS) (Figure 1.3) (Dulubova et al., 2005; Südhof, 2012). These five core proteins are also involved in vesicle priming, recruiting the voltage-gated calcium channels (VGCCs) to the plasma membrane, aligning of the pre- and postsynapse into a nanocolumn via cell-adhesion molecules to optimize neurotransmitters release with postsynaptic receptors, and reorganizing the presynapse during synaptic activity (Bourne, Chirillo, & Harris, 2013; Südhof, 2012). In addition to those core proteins, two large scaffold proteins of the AZ, Bassoon and Piccolo, are also involved in various mechanisms of presynapse organization such as: the assembly of the active zone, organization of the machinery for NT release, the maintenance of the synaptic vesicle pools and signaling from the presynapse to the nucleus (Gundelfinger, Reissner, & Garner, 2016; Südhof, 2012). The five core

proteins of the AZ accompanied by Bassoon and Piccolo constitute the building blocks of the active zone (Figure 1.3). Lastly, soluble *N*-ethylmaleimide-sensitive factor attached protein receptor (SNAREs) and Sec1/Munc18-like (SM) proteins are the machinery required to fuse the synaptic vesicle with the plasma membrane in order to release the NT in the synaptic cleft (Figure 1.3) (Südhof, 2012).

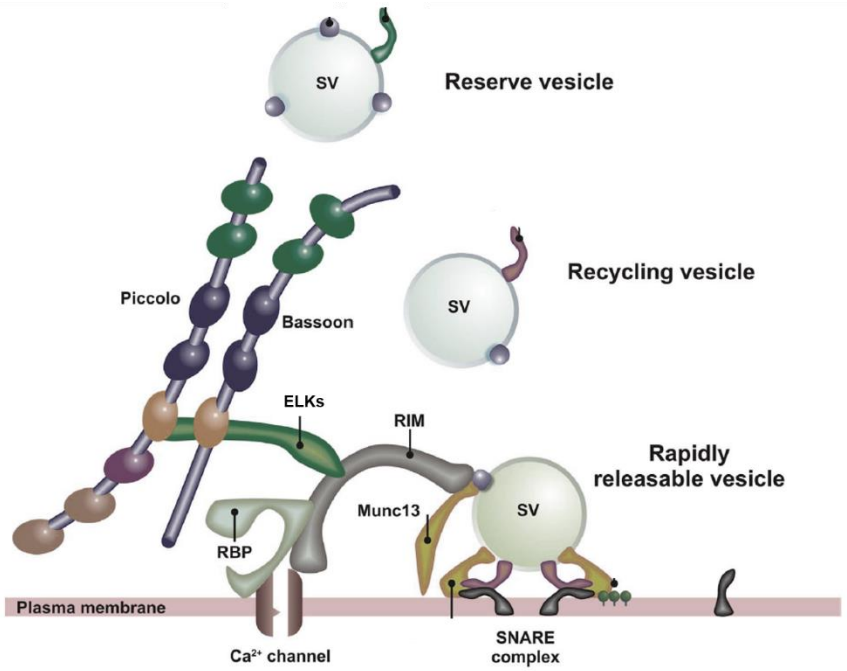

Figure 1.3. Molecular assembly of the active zone. The synaptic vesicles (SV) filled with neurotransmitters are divided into three different pools: reserve vesicles, recycling vesicles, and rapidly releasable vesicles. The recycling vesicles are docked at the active zone by the large complex formed with RIM, Munc13, RIM-BP (RBP), α-liprin, and ELKS. The docked recycling vesicles become rapidly releasable vesicles. They can fuse to the plasma membrane of the presynapse via the SNARE complex to release neurotransmitter into the synaptic cleft. Scaffold proteins Bassoon and Piccolo are involved in the assembly and organization of the active zone. Adapted from Holt, 2017.

1.3.2 Scaffold protein Bassoon

One of the largest proteins enriched in the active zone is the scaffold protein Bassoon (Dani, Huang, Bergan, Dulac, & Zhuang, 2010). This presynaptic protein plays a major role in the assembly of the AZ. Bassoon is one of the first proteins to reach the newly formed AZ during synaptogenesis (Friedman, Bresler, Garner, & Ziv, 2000; Zhai et al., 2001). Bassoon takes part in the recruitment of synaptic vesicles from the backfield and leads them to the release site as evidenced in the bassoon knockout mice that show a deficit in vesicle reloading at the AZ (Fejtova et al., 2010; Mukherjee et al., 2010). Furthermore, Bassoon participates in the positioning of VGCCs in the AZ to achieve optimal vesicle priming (Davydova et al., 2014). On the other hand, Altrock et

al., explored the impact of inactivated Bassoon on the number of the functional synapses (Altrock et al., 2003). Indeed, when Bassoon is not functional, i.e. cannot be anchored to the AZ, the strength of synaptic transmission is reduced because of the inactivation of a significant number of synapses while the quantal amplitude and synaptic release probability are unaffected (Altrock et al., 2003). The vesicles are unable to fuse in the inactivated synapses, but vesicles can be docked and clustered at the active zone. Therefore, Bassoon plays a fundamental role in the regulation of NT release machinery.

1.4 The postsynapse

While synapses can be formed onto cell bodies and axons, the majority of glutamatergic synapses are formed onto dendrites where the postsynaptic compartment is the dendritic spine. Spines are small membranous protrusions that are enriched in actin and possess different shapes and sizes. The size of the spine can vary from the small-thin spines (mean area: 0.44 ± 0.26μm²) to the big-mushroom spines (mean area: 1.50 ± 0.52μm²) (Harris, Jensen, & Tsao, 1992). The size of the spine is an important measure of its function as it reflects the efficiency of the synaptic transmission in the synapse formed by the spine. Put simply, a bigger spine has a stronger synapse than the smaller one (Bourne & Harris, 2011; Harris et al., 1992; Matsuzaki et al., 2001). Moreover, the presence of polyribosomes in the dendritic spine promotes local protein synthesis that is necessary for synapse remodeling in response to input (Ostroff, Fiala, Allwardt, & Harris, 2002). In a mature spine, the smooth endoplasmic reticulum (SER) and its extension into the spine apparatus (stack of SER containing dense plates) can also be found (Figure 1.2). They are involved in the regulation of intracellular calcium levels and local protein synthesis (Fifková, Markham, & Delay, 1983; Pierce, Van Leyen, & McCarthy, 2000).

1.4.1 The postsynaptic density

The postsynaptic density is a network of proteins located at the synapse and adhered to the postsynaptic membrane of the dendrite. The PSD possesses a highly complex molecular structure that comprises scaffold and cytoskeletal proteins, signaling enzymes, glutamate receptors, ion channels, and cell adhesion molecules. However, the key players for the regulation of synaptic function are the following PSD proteins:

the scaffold protein postsynaptic density 95 (PSD95), the glutamate receptors AMPA and NMDA, calcium/calmodulin-dependent protein kinase II (CaMKII) and actin (Herring & Nicoll, 2016). The amounts of these proteins are regulated in an activity-dependent manner and contribute to the efficiency of synaptic transmission (refer to section 1.6). Similar to the dendritic spine, the size and morphology of the PSD reveals the strength of the synapse (Arellano, Benavides-Piccione, DeFelipe, & Yuste, 2007; Desmond & Levy, 1986; Harris & Stevens, 1989; Thomas Schikorski & Stevens, 1997). Using electron microscopy, the pioneer in the field, Dr. Kristen Harris has shown that the PSD can be observed in different morphologies (Harris et al., 1992). The most common form is the macular form, which is described as a continuous disk-like morphology that composes ~ 70% of the PSD in young hippocampal neurons (Figure 1.4) (Toni et al., 2001). The other morphology revealed by electron microscopy (EM) is perforated PSDs and can be divided into three subtypes: U-shape, a ring-like structure termed perforated, and two or more clusters termed segmented (Figure 1.4) (Stewart et al., 2005). The perforated form of the PSD has been reported to be approximately three times larger than the macular PSD and is usually located on mushroom spines. On the other hand, the macular PSD composes 99% of the thin spines at 15 days post-natal (Harris et al., 1992; Popov et al., 2004; Stewart et al., 2005). The Harris laboratory has also discovered that the proportion of perforated PSDs increases during development. Indeed, at 15 days post-natal, 88% of the spines contain a macular PSD whilst in mature hippocampal neurons of an adult rat (40 and 70 days old), 81% of the spines have a perforated PSD (Harris et al., 1992). During development the occurrence of a spine apparatus increases and they are usually formed on mushroom spine containing perforated PSDs (Harris et al., 1992; Spacek & Harris, 1997). Moreover, when the number of cisterna (stacks of SER) in the spine apparatus increases, the size of PSD becomes larger (Spacek & Harris, 1997). The size of PSD is also tightly correlated with the size of the spine head (Harris et al., 1992; Harris & Stevens, 1989). Finally, the size of the active zone goes hand in hand with the number of docked vesicles of the presynaptic bouton and PSD size (Thomas Schikorski & Stevens, 1997). Altogether this suggests a role for PSD in the modulation of synaptic strength.

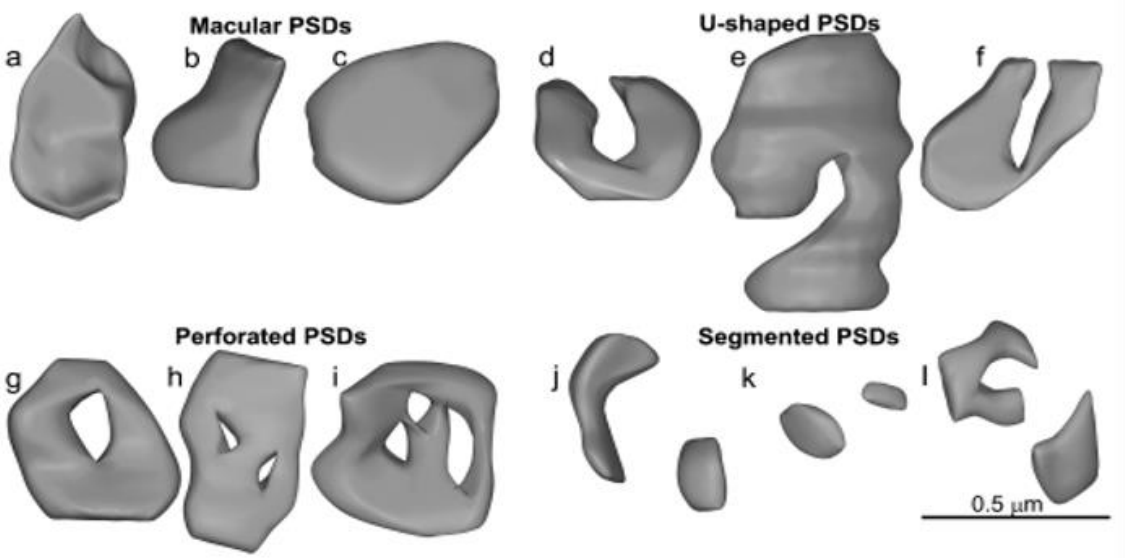

Figure 1.4 PSD morphologies: (a-c) Macular PSDs, (d-f) U-shaped PSDs, (g-i) Perforated PSDs and (j-l) Segmented PSDs. Adapted from Stewart et al., 2005.

1.4.2 The scaffold protein PSD95

The most abundantly found scaffold protein in the postsynaptic density is PSD95, a membrane-associated guanylate kinase (MAGUKs) family member. This scaffold protein, similar to the other MAGUK molecules, is composed of three PDZ domains, one Src-homology-3 (SH3) and one guanylate kinase (GuK) domain (Figure 1.5.A) (Funke, Dakoji, & Bredt, 2005; E. Kim & Sheng, 2004). Through its PDZ domain, PSD95 can interact with several synaptic proteins to regulate the strength of neurotransmission (Figure 1.5.B) (Irie et al., 1997). For instance, the PDZ domain interacts with glutamate ionotropic receptor NMDA type subunit 2B (GluN2B) and with the transmembrane AMPA receptor regulatory proteins (TARPs) to mediate the ratio of NMDA and AMPA receptors at the synapse, which I will explain in detail in the next section (Figure 1.5.B) (Kornau, Schenker, Kennedy, & Seeburg, 1995; Scannevin & Huganir, 2000; Schnell et al., 2002). Furthermore, PSD95 can also interact with proteins involved in the modulation of spine morphology such as kalirin-7, which promotes the polymerization of actin filament (F-actin), see section 1.6.1 (Figure 1.5.B) (Bosch & Hayashi, 2012; Penzes, Johnson, Kambampati, Mains, & Eipper, 2001). Binding of guanylate kinase-associated protein (GKAP) to the GuK domain of PSD95 also influences spine morphology by the recruitment of the scaffold protein SH3 domain and ankyrin repeat-containing protein (Shank). Shank interacts with the actin-binding protein cortactin and scaffold protein Homer, which in turn control spine morphology via binding with actin filament (Figure 1.5.B) (E. Kim et al., 1997; Naisbitt

et al., 1999; Sheng & Kim, 2002). Therefore, knockdown of PSD95 reduces the level of GKAP and Shank, as well as the number of excitatory synapses (Gerrow et al., 2006). Another binding partner of PSD95, α-actinin, is an actin-binding protein that also influences spine morphology (Matt et al., 2018). This actin partner is known to induce the stabilization of actin filament via cross-linking of F-actin after polymerization (Djinović-Carugo, Young, Gautel, & Saraste, 1999; Falzone, Lenz, Kovar, & Gardel, 2012; Matt et al., 2018; Sjöblom, Salmazo, & Djinović-Carugo, 2008). Via its interaction with the N-terminus of PSD95, α-actinin anchors and stabilizes PSD95 at the synapse (Matt et al., 2018). While a mutation in the binding site of α-actinin for PSD95 provokes the destabilization of PSD95 at the synapse which affects the AMPA receptors localization (Matt et al., 2018).

On the other hand, the binding of the PDZ domain of PSD95 with the adhesion molecule neuroligin-1 is another important process for PSD95 localization as it triggers the recruitment of PSD95 to the PSD (Barrow et al., 2009; Chih, Engelman, & Scheiffele, 2005; Giannone et al., 2013; Graf, Zhang, Jin, Linhoff, & Craig, 2004; Irie et al., 1997; Nam & Chen, 2005). Moreover, the PSD95-neuroligin-1 complex also mediates presynaptic release probability via retrograde modulation of extracellular calcium sensitivity (Futai et al., 2007). Therefore, the interaction of PSD95 with neuroligin-1 influence pre and postsynaptic function (Futai et al., 2007).

Furthermore, the palmitoylation of the N-terminal cysteine residue of PSD95 is also involved in the recruitment of PSD95 to the synapse. A mutant form of PSD95 that is palmitoylation-deficient was found to be not enriched in the PSD but was freely diffused in the dendrites and soma (Topinka & Bredt, 1998). Local palmitoylation activity organizes PSD95 into subsynaptic nanodomains of ~200 nm as seen by superresolution Stimulated Emission Depletion Microscopy (STED) (Fukata et al., 2013). The turnover of the non-palmitoylated PSD95 is slow and nearly immobile with a recovery rate of ~15% at 1h after the bleaching of the protein (Blanpied, Kerr, & Ehlers, 2008; Fukata et al., 2013; Kuriu, Inoue, Bito, Sobue, & Okabe, 2006). Nevertheless, palmitoylation increased the mobility of the PSD95 with a recovery rate of 56% at 1h after bleaching event (Fukata et al., 2013). Perhaps the gain of mobility induces morphological changes in the protein organization of PSD95.

As PSD95 is the most abundant protein of the PSD, it has been recently reported by my laboratory to have a similar morphology as the PSD *in vivo* using STED nanoscopy. Specifically, PSD95 assemblies can also be found with a perforation and segmentation while its size, like the PSD, is well correlated with the spine head area (Masch et al., 2018; Wegner, Mott, Grant, Steffens, & Willig, 2018). However, the formation and function of the perforated PSD95 remains unclear. Interestingly, the overexpression of PSD95 produces a larger and more complex form of PSD95 nanoarchitecture that is mostly accompanied by a perforation in its structure (Nikonenko et al., 2008).

Finally, PSD95 is a scaffold protein important for the development of excitatory synapses. An acute knockdown of PSD95 via Ribonucleic acid interference (RNAi) has both functional and morphological impacts on the glutamatergic synapse. PSD95 knockdown reduces the amplitude of excitatory post synaptic current (EPSC) mediated by AMPA and NMDA receptors as well as the size of the spine head (Ehrlich, Klein, Rumpel, & Malinow, 2007). Furthermore, behavior experiments on mice lacking PSD95 found that the knockout mice have learning and working memory deficits (Coley & Gao, 2019). Therefore the appropriate level of the scaffold protein is required to improve the strength of the synapse.

On the other hand, synaptic transmission is still present in knockout PSD95 mice (Elias et al., 2006). Deletion of PSD95 affects the targeting of AMPA receptors at the synapse but not NMDA receptors (Béïque et al., 2006; Carlisle, Fink, Grant, & O'dell, 2008; Chen et al., 2011; Elias et al., 2006). Finally, it has been shown that in mice lacking both PSD95 and PSD93 (a MAGUK protein similar to PSD95) increased expression of the synapse-associated protein 90 (SAP102), the remaining homolog MAGUK proteins at the synapse, is seen. (Figure 1.5.A) (Elias et al., 2006).

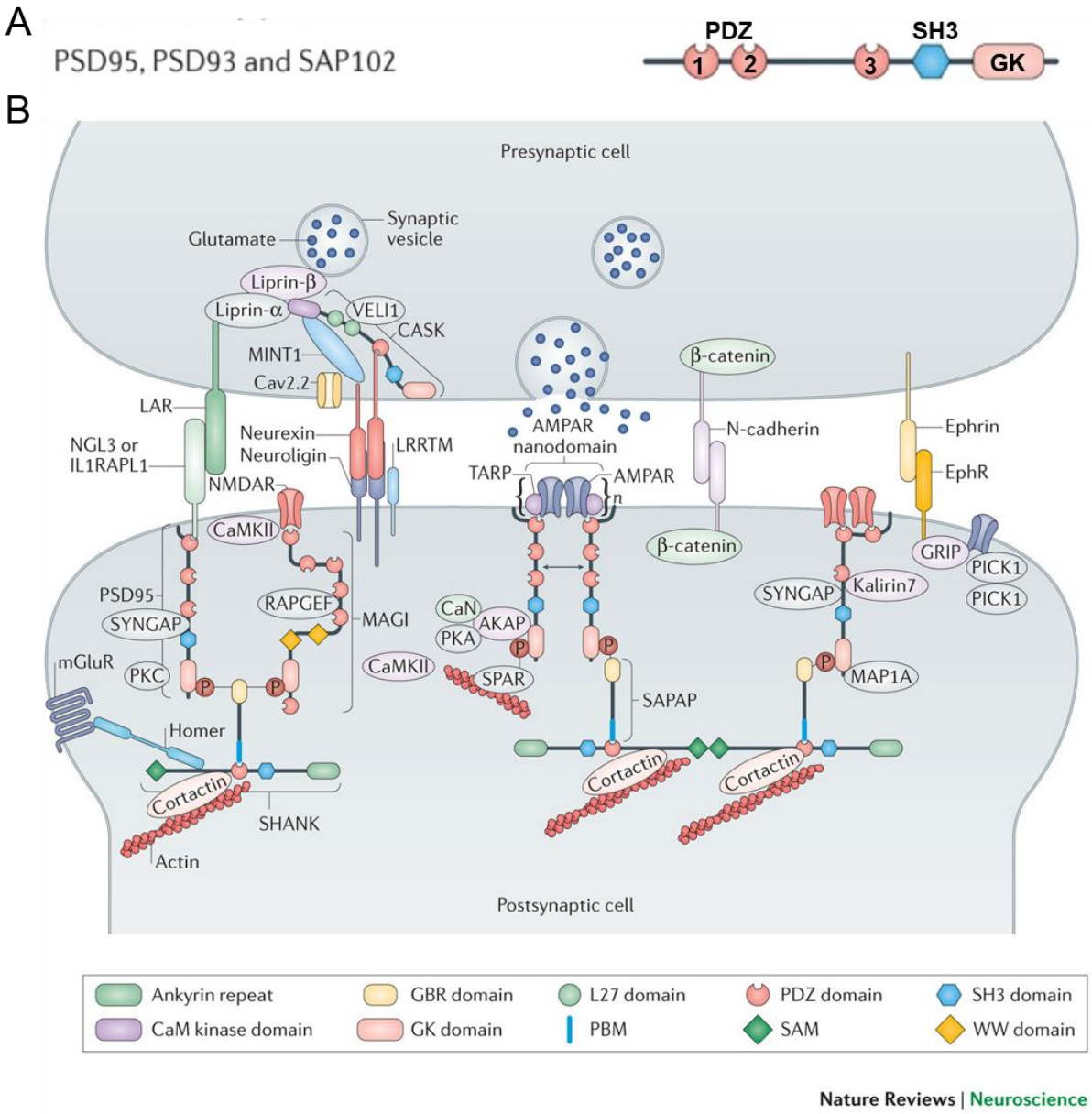

Figure 1.5 PSD95 signaling complex. (A) Domain organization of membrane-associated guanylate kinase (MAGUKs) family members postsynaptic density (PSD)95, PSD93 and synapse-associated protein 90 (SAP102). These scaffold protein possess three PDZ domains, one Src-homology-3 (SH3) and one guanylate kinase (GK) domain. **(B)** Complex organization of the postsynapse and binding partners of PSD95. Adapted from J. Zhu, Shang, & Zhang, 2016

1.5 Post-synaptic ionotropic glutamate receptors

The transmission of information is regulated by the ionotropic glutamate receptors located on the PSD. They have the capacity to induce changes in the electrical potential of the neuron by their cation permeability and thereby modulate the efficiency of synaptic transmission (Dingledine, Borges, Bowie, & Traynelis, 1999). According the original Katz model, quantal amplitude was attributed exclusively to the presynapse, however, it is now accepted that quantal amplitude is also highly dependent on

glutamate receptors. According to their number, synaptic localization, and molecular composition, glutamate receptors influence the quantal amplitude and the strength of the synapse (Glasgow, McPhedrain, Madranges, Kennedy, & Ruthazer, 2019; MacGillavry, Song, Raghavachari, & Blanpied, 2013; Nair et al., 2013). The two most important glutamate receptors for memory function are NMDA and AMPA receptors. They have the ability to form signaling complexes with postsynaptic proteins and to participate in the formation, maturation, and regulation of the synapse (Sheng & Kim, 2011).

1.5.1 NMDA receptors

The NMDA ligand-gated ion channel plays a fundamental role in learning and memory process. During activation, the NMDA receptor allows extracellular Ca^{2+} and Na^{2+} to flow into the cell according to its concentration gradient while intracellular K^{+} comes out. This cation exchange creates an excitatory postsynaptic potential and raises the intracellular level of calcium, which acts as a second messenger in diverse signaling pathways. The special feature of the NMDA receptor is its ability to detect the synchronous activity of the pre- and post-synapse. Due to these properties, the NMDA receptor is called a coincidence detector. During the inactive state, the NMDA receptor is blocked by extracellular magnesium (Mg^{2+}) ions. The channel can only be opened when the binding of glutamate to NMDA receptor is coupled with post synaptic depolarization that removes the Mg^{2+} block (Dingledine et al., 1999). Other factors that are essential for NMDA receptor activation are the co-agonists glycine and D-serine, which are released into the extracellular space by surrounding glial cells (Panatier et al., 2006).

Furthermore, the subunit composition of NMDA receptor and their different properties influence the efficiency of neuronal transmission. This coincidence receptor is divided into three categories of subunits: GluN1, GluN2A-D, and GluN3A-B. NMDA receptors containing the GluN3 A/B subunits are not functional as their activity is completely abolished (Henson, Roberts, Pérez-Otaño, & Philpot, 2010; Low & Wee, 2010). To form a functional a NMDA receptor, the subunits must be organized into a heterotetramer containing two GluN1 and two GluN2 subunits. While glutamate binds to GluN2 subunits, the co-agonists glycine and D-serine bind with GluN1 (Anson, Chen, Wyllie, Colquhoun, & Schoepfer, 1998; Laube, Hirai, Sturgess, Betz, & Kuhse, 1997; Meguro et al., 1992; Monyer et al., 1992). Additionally, the biophysical properties of NMDA

receptor change according to its subunit composition. For example, the di-heteromers of GluN1/GluN2A and GluN1/GluN2B have more efficient neurotransmission than their homologs GluN1/GluN2C and GluN1/GluN2D. Specifically, the receptor comprised of GluN1/GluN2A and GluN1/GluN2B is more sensitive to membrane potential, which improves the channel conductance and its calcium permeability compared to the NMDA receptor made of GluN2C and GluN2D (Kuner, Wollmuth, Karlin, Seeburg, & Sakmann, 1996; Schneggenburger, 1996; Stern, Behe, Schoepfer, & Colquhoun, 1992; Wyllie, Behe, Nassar, Schoepfer, & Colquhoun, 1996). Finally, every GluN2 subunit possesses a distinct intracellular C-terminal domain that is the interaction site for proteins essential for synaptic function, like PSD95 and CaMKII. For example, PSD95 can modulate the insertion and retention of NMDA receptor at the synapse via the interaction of its PDZ domain with the C-terminal tail of the GluN2 subunit (Lim, Hall, & Hell, 2002; Lin, Skeberdis, Francesconi, Bennett, & Zukin, 2004; Roche et al., 2001). On the other hand, CaMKII triggers a signaling cascade that is necessary for the learning and memory process through its interaction with the C-terminal of the GluN2 subunit (Bayer, De Koninck, Leonard, Hell, & Schulman, 2001; Lin et al., 2004; Prybylowski et al., 2005; Scannevin & Huganir, 2000)

1.5.2 AMPA receptors

AMPA and NMDA receptors constitute the main players in the neurotransmission of excitatory synapses. They modulate the majority of the postsynaptic excitatory currents of glutamatergic transmission (Henley & Wilkinson, 2013). As a cation channel, AMPA receptors are permeable to Na^+, K^+, and Ca^{2+} ions, but the presence of the GluA2 subunit in the composition of the synaptic AMPA receptor makes this channel impermeable to calcium (Bredt & Nicoll, 2003). Thus, when activated, they quickly allow a considerable quantity of sodium ions to enter the cell and quickly induce the depolarization of the postsynaptic membrane due to their large opening probability and rapid binding kinetics (Raghavachari & Lisman, 2004). Thus, they are responsible for the majority of the rapid excitatory currents of synaptic transmission. Additionally, the conductance of the AMPA channel varies in a range of <1 pS to ~30 pS depending on its subunit composition (Swanson, Kamboj, & Cull-Candy, 1997). Similar to NMDA receptor, AMPA receptor subunit composition is important to achieve its role. This receptor contains four subunits: GluA1 to GluA4. To form a functional channel, AMPA subunits must be organized into a tetramer, where most of the receptors have a dimeric

dimer structure. Under basal conditions, ~80% of synaptic AMPA receptors consist of GluA1/ GluA2 subunits and ~16% with GluA2/ GluA3 heterotetramers (W. Lu et al., 2009). It is important to note that the receptor made with homomeric GluA1 subunits (4 X GluA1 subunits) represents only a minority of about 8% of the total AMPA receptor population at the synapse and the majority of extrasynaptic AMPA receptor (~95%) are composed of GluA1/ GluA2 subunits (W. Lu et al., 2009; Wenthold, Petralia, Blahos, & Niedzielski, 1996). All subunits possess a binding site for its agonist glutamate and only two sites need to be occupied to obtain an open conformation (Rosenmund, Stern-Bach, & Stevens, 1998). AMPA receptors formed by a GluA1 homomer are calcium-permeable and have a higher conductance and open probability compared to those containing GluA2 (Swanson et al., 1997). The conductance of the receptor is also proportional to the quantity of glutamate bound to its subunits (Rosenmund et al., 1998). This highlights the importance of a proper AMPA receptor localization in precise apposition to the glutamate release site to obtain an optimal postsynaptic response. Thus, the quantal amplitude depends also on the specific localization of the AMPA receptor to be aligned with the AZ.

One way to measure synaptic strength is by recording miniature excitatory postsynaptic currents (mEPSCs) in neurons via whole-cell patch-clamp. When combined with the voltage-gated sodium channel blocker tetrodotoxin (TTX) to eliminate any action potentials, this technique allows us to measure the ionic flux through postsynaptic receptors triggered by the spontaneous fusion of vesicles (Glasgow et al., 2019). Using this technique, it has been shown that knockdown and knockout of PSD95 reduced the amplitude of postsynaptic response of the AMPA receptor by 40% (Chen et al., 2015; Ehrlich et al., 2007; Schlüter, Xu, & Malenka, 2006). Therefore, PSD95 is integral in optimizing the efficiency of synaptic transmission mediated by the AMPA receptor. Indeed, PSD95 is necessary to anchor and stabilize the AMPA receptor at the synapse via TARPs (Figure 1.5.B) (Bats, Groc, & Choquet, 2007; Opazo, Sainlos, & Choquet, 2012). The best-characterized TARP proteins are stargazing (TARP γ2) and TARP γ8. They bind to the PDZ domain of PSD95 to immobilize AMPA receptors at the synapse during lateral diffusion and for optimal alignment with glutamate release from the presynapse. Therefore, PSD95 serves as a slot for the insertion of new AMPA receptors at the PSD (Opazo et al., 2012). This anchoring mechanism of PSD95-mediated slotting is further controlled by CaMKII,

which triggers the trapping of AMPA receptor into the PSD95 slot by phosphorylation of TARP. This modification strengthens the binding of TARP with PSD95 to maintain AMPA receptors in the available slot (Opazo et al., 2010). Furthermore, a new publication from July 2020 reports the crucial role of TARP γ8 in the enrichment of AMPA receptor at the synapse via interaction with the PDZ domain of PSD95 (Jake F. Watson, Alexandra Pinggera, Hinze Ho, 2020a). They also report an important role for the extracellular N-terminal domain of AMPA receptor subunits, which fine-tune the positioning of the functional receptor (Jake F. Watson, Alexandra Pinggera, Hinze Ho, 2020b). Another key player is neuroligin-1, which is not only crucial for the localization of PSD95 at the synapse, but is also important for the precise localization of the AMPA receptor. A truncated form of neuroligin-1, where the C-terminal is unable to bind to the PDZ domain of PSD95, induces a deviation of ~100 nm of AMPA receptor alignment with the presynaptic protein RIM, which provokes a significant reduction of mEPSC amplitude mediated by AMPA receptor (Haas et al., 2018).

Similar to PSD95, AMPA receptors are also organized into a nanodomain of ~70 nm that contains around 20 receptors and remains practically immobile at the synapse (Nair et al., 2013). The size and number of AMPA receptor nanodomains, as well as the amplitude of mEPSCs, are affected by PSD95 expression. Overexpression of PSD95 promotes the enlargement of a single AMPA receptor nanodomain and an increase in the number of nanodomains (Nair et al., 2013). However, overexpression of PSD95 can cause artifacts. It is still unknown if the number of AMPA receptors increase during learning and memory process or if the content of one nanodomain increases. A computational simulation predicts an augmentation of mEPSC frequency if the number of AMPA receptor nanodomains is increased and augmentation of mEPSC amplitude if the content of one nanodomain grows (Scheefhals & MacGillavry, 2018). Moreover, the number of AMPA receptor nanodomains is also correlated with the size of PSD95 assembly. The silent synapse, which corresponds to a synapse without AMPA receptors, shows smaller PSD95 assemblies than those populated with AMPA receptor nanodomains (Nair et al., 2013). Those silent synapses are mostly found in the immature spine and are unable to carry out the excitatory current even upon presynaptic glutamate release (Kerchner & Nicoll, 2008). Nonetheless, they are transformed into a functional synapse during development and synaptic activity (Gomperts, Rao, Craig, Malenka, & Nicoll, 1998; W. Y. Lu et al., 2001). The size of

PSD is positively correlated with the number of AMPA receptors (Takumi, Ramírez-León, Laake, Rinvik, & Ottersen, 1999). Finally, all perforated PSDs contain AMPA receptors in adult CA1 hippocampal neurons, while only 64% of the synapses with a macular PSD have AMPA receptors (Ganeshina, Berry, Petralia, Nicholson, & Geinisman, 2004). Therefore, the increased number of synaptic AMPA receptors, their localization opposed to glutamate release sites, and high conductance of the receptor boost the postsynaptic membrane potential and improve the transmission efficiency between neurons, an essential process for memory formation (Lisman & Raghavachari, 2006).

1.6 Long-term potentiation

In 1949, Donald Hebb postulated a relationship between memory process and synaptic strength changes where pre and postsynaptic modification appear to coincide together (Hebb, 1949). Almost 20 years later, Terje Lomo was the first to prove his theory using an experimental strategy (Lomo, 1966). By applying a high-frequency stimulation to hippocampal excitatory neurons, he reported plastic changes of stimulated synapses and a long-lasting increase of transmission efficiency that occurred for four hours (Lomo, 1966). His discovery introduced the notion of long-term potentiation (LTP) and until today, it is one of the most prominent molecular models for learning and memory. The process is divided into two phases: early-LTP (E-LTP), which is independent of proteins synthesis and involves CaMKII activity, and late-LTP (L-LTP), which requires the activation of transcription factors and synthesis of new proteins. E-LTP can be generated by single tetanus of 100-Hz per second, inducing a long-lasting increase of the synaptic strength for 1 to 3h, while L-LTP is caused by repetitive application of tetanus or by one strong tetanus which boosts the transmission efficiency for over 24h (Abel et al., 1997; Frey, Huang, & Kandel, 1993).

1.6.1 Early-LTP through CaMKII activity

The LTP produced at the Schaffer collateral-CA1 synapses of the hippocampus is the most accepted and studied model that exhibits a long-lasting increase in synaptic strength and mainly occurs through the incorporation of AMPA receptors (Herring & Nicoll, 2016). The induction of LTP is triggered by the activation of NMDA receptors, after which the NMDA channel mediates the influx of calcium ions into the synapse. Calcium ions bind in turn to the calcium sensor calmodulin (CaM), which activates the

translocation of CaMKII into the synapse. While the influx of calcium through the NMDA receptor is transient, the following autophosphorylation of CaMKII at threonine 286 (t286) initializes autonomous activity of CaMKII (Chao et al., 2010; De Koninck & Schulman, 1998; Pi et al., 2010). The CaMKII kinase activity persists for a short period even after the calcium concentration returns to the basal state (Miller & Kennedy, 1986; Pi et al., 2010). When activated, CaMKII interacts with the NMDA receptor GluN2B subunit to induce post-translational modifications of specific postsynaptic proteins necessary for LTP, such as AMPA receptors (Baltaci, Mogulkoc, & Baltaci, 2019; Bayer et al., 2001). LTP is impaired when either the CaMKII binding site for GluN2B is mutated or the phosphorylation of T286 is disrupted (Bayer et al., 2001; Giese, Fedorov, Filipkowski, & Silva, 1998; Lucchesi, Mizuno, & Giese, 2011). Activated CaMKII is then necessary and sufficient to ensure LTP (Lisman & Raghavachari, 2015).

More specifically, through phosphorylation, CaMKII is able to regulate the function of several proteins, with the best documented being AMPA receptors. For instance, the translocation of CaMKII into the synapse causes an increase in AMPA ion channel conductance by direct phosphorylation of serine831 on the GluA1 C-tail and thereby enhances synaptic strength (Kristensen et al., 2011; Lee, Barbarosie, Kameyama, Bear, & Huganir, 2000; Mammen, Kameyama, Roche, & Huganir, 1997). Activation of CaMKII also increases the number of AMPA receptors present at the synapse by inducing their stabilization with the scaffold protein PSD95. As mentioned in the last chapter, CaMKII phosphorylates the C-tail of TARP, which allows TARP to interact with the PDZ domain of PSD95 and stabilizes AMPA receptors at the synapse (Hafner et al., 2015; Opazo et al., 2010). It has been proposed that following LTP induction, free slots for AMPA receptors become available in PSD95 via interaction with TARP (Baltaci et al., 2019; Walkup et al., 2016). As such, PSD95 interacts through its PDZ domain with the Ras/Rap GTPase-activation protein (GAP), also called SynGAP (Walkup et al., 2016). At rest, SynGap is enriched at the synapse, but following LTP stimulation, its affinity for PSD95 is highly reduced through phosphorylation by CaMKII (Walkup et al., 2016). This loss of affinity between PSD95 and SynGAP gives rise to the dispersion of SynGAP out of the synapse, which allows TARP to interact with PSD95 to stabilize AMPA receptor at the PSD (Walkup et al., 2016).

Furthermore, the dispersion of SynGap produces Ras activation by the reduction of RasGAP activity (Araki, Zeng, Zhang, & Huganir, 2015). Ras activation generates a signaling cascade that activates mitogen-activated protein kinase (MAPK), also called extracellular signal-regulated kinases (ERK) (Ye & Carew, 2010). The Ras-ERK pathway leads to the exocytosis of GluA1 containing AMPA receptors into the perisynaptic site of the spine. The rate of AMPA receptor exocytosis increases by 5-fold following LTP stimulation and returns to a basal level within ~1 minute following stimulation (Patterson, Szatmari, & Yasuda, 2010). After exocytosis, extrasynaptic AMPA receptors reach the synapse by lateral diffusion before being trapped by PSD95 via TARP interaction (Opazo et al., 2010). LTP stimulation has been reported to generate a transient insertion primarily of synaptic homomeric GluA1 AMPA receptors, which possess a higher conductance than GluA2 (Plant et al., 2006). About 25 minutes after LTP induction, receptor subunit recomposition of occurs and replaces a fraction of the GluA1 subunits with GluA2 to form GluA1/2 synaptic AMPA receptors (Plant et al., 2006). Moreover, SynGap knockdown, which frees a slot at PSD95 PDZ domain to interact with TARP, gives rise to increased AMPA receptor expression at the synapse and spine head enlargement (Araki et al., 2015). Additionally, CaMKII is also crucial for spine expansion during LTP. By phosphorylation, CaMKII induces modification of Kalirin-7 and Trio-9 proteins that activate Rho GTPases. Eventually, the activation of those Rho GTPases promotes actin polymerization, a necessary mechanism for spine head enlargement during LTP (Bosch & Hayashi, 2012; Herring & Nicoll, 2016). Consequently, using an actin polymerization inhibitor, like latrunculin A, prevents spine head expansion after LTP stimulation (C. H. Kim & Lisman, 1999; Matsuzaki, Honkura, Ellis-Davies, & Kasai, 2004).

1.6.2 Protein synthesis and maintenance of LTP

The late phase of LTP on the other hand is ensured by de novo protein synthesis and requires the activity of protein kinase A (PKA), cyclic adenosine monophosphate (cAMP) response element-binding protein (CREB), and MAPK (Baltaci et al., 2019; Kuriu et al., 2006; Naisbitt et al., 1999). The signaling from the synapse to the nucleus begins with the activation of the cAMP/PKA pathway, which is triggered by two mechanisms. First, through the activation of calcium/CaM sensitive adenyl cyclase (AC) by Ca^{2+}/CaM and second, via the stimulation of AC by the activation of G-protein-coupled receptors (Baltaci et al., 2019; Elliot, Dudai, Kandel, & Abrams, 1989; W. J.

Tang & Gilman, 1991). More precisely, when the concentration of cAMP increases, cAMP molecules can bind the regulatory subunits of PKA, causing their dissociation from catalytic subunits. PKA is then free to move to the nucleus and induce the phosphorylation of CREB, which generates the activation of transcription factors necessary for new protein synthesis (Baltaci et al., 2019; Nguyen & Woo, 2003). When PKA and CREB are genetically mutated in mice, the transgenic mice develop a severe deficit in L-LTP, although E-LTP remains normal (Abel et al., 1997; Baltaci et al., 2019; Bourtchuladze et al., 1994).

Furthermore, the activation of MAPK is also essential for the late phase of LTP. It can be activated through phosphorylation initially triggered by PKA via cAMP or by CaMKII activation (Baltaci et al., 2019; Vossler et al., 1997; J. J. Zhu, Qin, Zhao, Van Aelst, & Malinow, 2002). The two main targets of MAPK are the transcription factors CREB and Elk-1 (Bozon, Davis, & Laroche, 2003; Veyrac, Besnard, Caboche, Davis, & Laroche, 2014). When activated, those transcription factors generate the transcription of the immediate early genes (IEG) related to synaptic activity (Bozon et al., 2003; Veyrac et al., 2014). One of the IEGs important for L-LTP is the plasticity-related transcription factor Zif268, where transcription of Zif268 mRNA increases strongly between 10 min to 2h in following LTP stimulation (Abraham, Dragunow, & Tate, 1991; Richardson & Richardson, 1992). In contrast, L-LTP is abolished in transgenic mice with mutated Zif268, while E-LTP is not affected (Baltaci et al., 2019; James, Conway, & Morris, 2005; Jones et al., 2001; Veyrac et al., 2014).

Moreover, following transcription in the nucleus, several mRNAs are transported into the dendrite and dendritic spines to undergo activity-dependent translation of proteins essential for LTP, such as CaMKII, GluA1, GluA2, and PSD95 (Grooms et al., 2006; Ifrim, Williams, & Bassell, 2015; Mayford et al., 1996). The synthesis of new proteins by local translation in the spine head is performed by polyribosomes (Ostroff et al., 2017, 2002; Sutton & Schuman, 2006). LTP causes the translocation of polyribosomes from the dendrite to stimulated spines (Ostroff et al., 2002). This in turn increases the rate of local synthesis of synaptic proteins in response to synaptic activity (Ostroff et al., 2002).

Finally, the maintenance of LTP is further controlled by protein kinase M zeta (PKMζ). PKMζ does not possess any autoinhibitory regulatory domain; therefore, the kinase is constitutively active, which is an important property for the maintenance of LTP (Sacktor, 2011). Through this characteristic, PKMζ blocks the endocytosis process of AMPA receptors and prevents the lateral diffusion of synaptic AMPA receptors out of the synapse (Sacktor, 2011; Yu et al., 2017). Thus, the maintenance of LTP is guaranteed by the kinase through the stabilization of new AMPA receptors at the synapse.

1.7 Structural LTP

One of the striking features of LTP is the persistent and physical enlargement of the spine after activity-driven plasticity, which is termed structural LTP (Herring & Nicoll, 2016). The spine head is enriched with actin filaments, which is a cytoskeletal protein that dynamically regulates the morphology of the spine head (Figure 1.5.B) (Honkura, Matsuzaki, Noguchi, Ellis-Davies, & Kasai, 2008). Following activation of the NMDA receptor, a fast and persistent increase of the spine head occurs (Bosch et al., 2014). This process is promoted by rapid F-actin polymerization accompanied by a reduction of the depolymerization rate, which leads to an increase in the size of the spine head (Bamburg, 1999; Borovac, Bosch, & Okamoto, 2018). Precisely, in the first 5 minutes following LTP stimulation, CaMKII promotes the remodeling of the actin cytoskeleton via disassembly of actin filaments that is rapidly followed by polymerization of F-actin. After the first 5 minutes following LTP induction, stabilization and consolidation of the F-actin assemblies occurs, which is mediated by actin-binding proteins Actin Related Protein 2/3 (Arp2/3) , Actin-interacting protein 1 (Aip1), Debrin and α-actinin (Bosch et al., 2014; J. Kim et al., 2015; Okamoto, Bosch, & Hayashi, 2009). Furthermore, it has been shown that only small spines are selectively enlarged after LTP induction (Matsuzaki et al., 2004), while another finding shows that the absolute volume changes of the spine head occur for both small and larger spines (Kopec, Li, Wei, Boehm, & Malinow, 2006). It has been also suggested that only spines containing SER enlarge (Borczyk, Śliwińska, Caly, Bernas, & Radwanska, 2019).

Furthermore, spine head size is positively correlated with the PSD area, the size of the active zone, the number of AMPA receptors, and the efficiency of synaptic transmission (Harris & Stevens, 1989; Matsuzaki et al., 2001; Takumi et al., 1999). Therefore, when

the spine head enlarges, the size of PSD is also expected to increase. It has been shown by the laboratory of Prof. Kristen Harris that the PSD area increases 2h after LTP stimulation, but only in the spines containing subcellular resources like SER and/ or polyribosomes (Chirillo, Waters, Lindsey, Bourne, & Harris, 2019). Moreover, their research also shows that the enlargement of the PSD is accompanied by the SER moveing into the spine apparatus, which occurs at 2h after LTP inducement (Chirillo et al., 2019). Interestingly, only 10% to 20% of the spines possess SER, which is usually located in larger spine heads (Chirillo et al., 2019; Spacek & Harris, 1997). Additionally, the importance of the spine apparatus has been also emphasized during LTP. It is mostly found in the neck of the spine and it is involved in the regulation of calcium and local protein synthesis (Deller, Merten, Roth, Mundel, & Frotscher, 2000). For instance, the inhibition of the spine apparatus in mice via suppression of the actin-binding protein synaptopodin, an essential protein for spine apparatus formation, leads to impairment in spatial learning and a failure to increase the field EPSC amplitude 1h after LTP induction (Deller et al., 2003). Thus, the spine apparatus is another structural modification that arises during synaptic plasticity.

Most of the spine heads that contain a spine apparatus also possess a perforated PSD(Harris et al., 1992; Spacek & Harris, 1997). Perforated PSDs also emerge during LTP, as seen by electron microscopy, most commonly at 30 min after stimulation (Buchs & Muller, 1996; Nicolas Toni et al., 2001). Toni et al. suggest that non-macular PSDs (Figure 1.4 d-l), notably the number of segmented PSDs (Figure 1.4.j-l), increase 30 min after LTP (Nicolas Toni et al., 2001). The level of non-macular PSDs returns to control levels between 45 to 120 min after LTP induction (Nicolas Toni et al., 2001). Furthermore, Stewart et al. found a significant decrease of macular PSDs (Figure 1.4.a-c) at 1h after LTP, which is mainly associated with an increase in number of perforated PSDs (Figure 1.4.d -i), not segmented PSDs (Figure 1.4.j-l) (Stewart et al., 2005). Moreover, the augmentation of perforated PSDs is accompanied by enlargement of PSDs, spine heads, and the pool of readily releasable vesicles (Toni et al., 2001). This implies that the perforated PSD has the ability to strengthen the synapse. However, electron microscopy cannot reveal the dynamic formation of perforated PSDs due to sample fixation, thus the role of this structural modification in synaptic transmission remains unclear.

Moreover, PSD95 assembly, the most abundant scaffold protein found in the PSD, shows similar structural and size modifications following LTP induction. Indeed, it has been demonstrated using two-photon microcopy that PSD95 assembly increases in size approximately 1h after LTP (Bosch et al., 2014; Meyer, Bonhoeffer, & Scheuss, 2014). Remodeling of PSD95 architecture has been also visualized using super-resolution STED. STED microscopy reveals that PSD95 assembly is reorganized into nanodomains through palmitoylation activity (Fukata et al., 2013). Following chemical LTP, PSD95 nanodomains form perfectly aligned nanomodules with presynaptic proteins, and their number increases within minutes after LTP induction due to their mobility (Hruska, Henderson, Le Marchand, Jafri, & Dalva, 2018). Finally, STED microscopy has also revealed a new nanoorganization of PSD95. It was reported by our laboratory that PSD95 can be organized in a U-shape or ring-like in the visual cortex of a living mouse (Figure 1.4 d-i). However, the formation of such shapes and their impact on transmission efficiency is still unknown (Masch et al., 2018; Wegner et al., 2017).

Finally, the alignment of the presynaptic release of NT with AMPA receptors seated on PSD95 is crucial for the synaptic transmission. This precise alignment of pre and postsynaptic proteins with AMPA receptors was recently termed a trans-synaptic nanocolumn. The Blanpied laboratory has shown, using superresolution 3D- stochastic optical reconstruction microscopy (STORM) imaging, that the presynaptic protein RIM forms a cluster of ~80 nm precisely aligned with AMPA receptor nanodomains (A. H. Tang et al., 2016). Therefore, an increase of PSD95 size or PSD95 remodeling would also have an impact on AMPA receptor nanodomain organization and on the precise nanocolumn alignment with the active zone. Indeed, the active zone in hand with the PSD area significantly enlarges about 2h following LTP (Bell et al., 2014). Bell et al. also point out that the active zone area increases for both small and larger spine after activity-driven plasticity (Bell et al., 2014). In addition, an augmentation of recycling vesicle numbers at the vesicle release site has been demonstrated to occur after LTP induction (Rey, Marra, Smith, & Staras, 2020). Thus, the presynaptic active zone expands after LTP. Nevertheless, not much is known about the dynamics and structure of the AZ during LTP. Does it display similar morphology as the PSD? What happens to the active zone during the formation of perforated and segmented PSDs?

1.8 Super-resolution STED to resolve synaptic proteins

It was previously demonstrated by Meyer et al. that PSD95 undergoes structural plasticity during LTP using two-photon microscopy (Bosch et al., 2014; Meyer et al., 2014). They demonstrated that the volume of the PSD95 cluster increases following LTP (Meyer et al., 2014). However, the spatiotemporal nanoorganization of PSD95 cannot be revealed by conventional light microscopy due to the diffraction limit of ~200 nm. Thus, a lot of information about the protein nanoorganization is lost. Furthermore, the molecular resolution of electron microscopy allows us to resolve the nanoscale organization of proteins but only on fixed or frozen samples. One way to bypass the diffraction limit and access the protein dynamics is by the noval superresolution light microscopy techniques. There are two main superresolution techniques, the deterministic scanning technique STED and reversible saturable optical fluorescence transition (RESOLFT) microscopy, where excitation and detection of the fluorescent protein are revealed point-by-point (Eggeling, Willig, Sahl, & Hell, 2015). The second technique is based on the image reconstruction of single molecule localizations and is called photoactivation localization microscopy (PALM) and stochastic optical reconstruction microscopy (STORM) (Eggeling et al., 2015). In numerous studies, STED has been shown to resolve synaptic proteins during live-cell imaging and is superior to other techniques for imaging in tissue (Hruska et al., 2018; Wegner et al., 2017; Westphal et al., 2008). Therefore, it is the technique of choice for the present thesis. The principle of STED microscopy is to deplete the fluorescence emission of a molecule via a red-shifted beam (Figure 1.6.) (Hell & Wichmann, 1994). Using a doughnut-shaped depletion beam in the X, Y focal plane, it deexcites the fluorescent proteins at the periphery of the excitation spot. Thus, the effective fluorescence volume detected at the center of the doughnut is reduced and will break through the diffraction-limit of light (Figure 1.6) (Hell & Wichmann, 1994). Precisely, when the doughnut-shaped laser is superimposed with the excitation light, the doughnut center, where the intensity of the STED laser is zero, produces a fluorescence spot which can be tuned in size by adjusting the STED laser intensity. This fluorescence spot can then be used to image with a resolution between 50 to 100nm, which is below the diffraction barrier (Figure 1.6) (Hell & Wichmann, 1994). The effective fluorescence spot can be measured with small fluorescent objects and gives an estimate of the obtainable resolution (Figure 1.6). Using STED nanoscopy, we can resolve the organization of

synaptic proteins like the perforated PSD95 nanoorganization, which was previously hidden by the diffraction limited conventional light microscopy (Masch et al., 2018; Wegner et al., 2018).

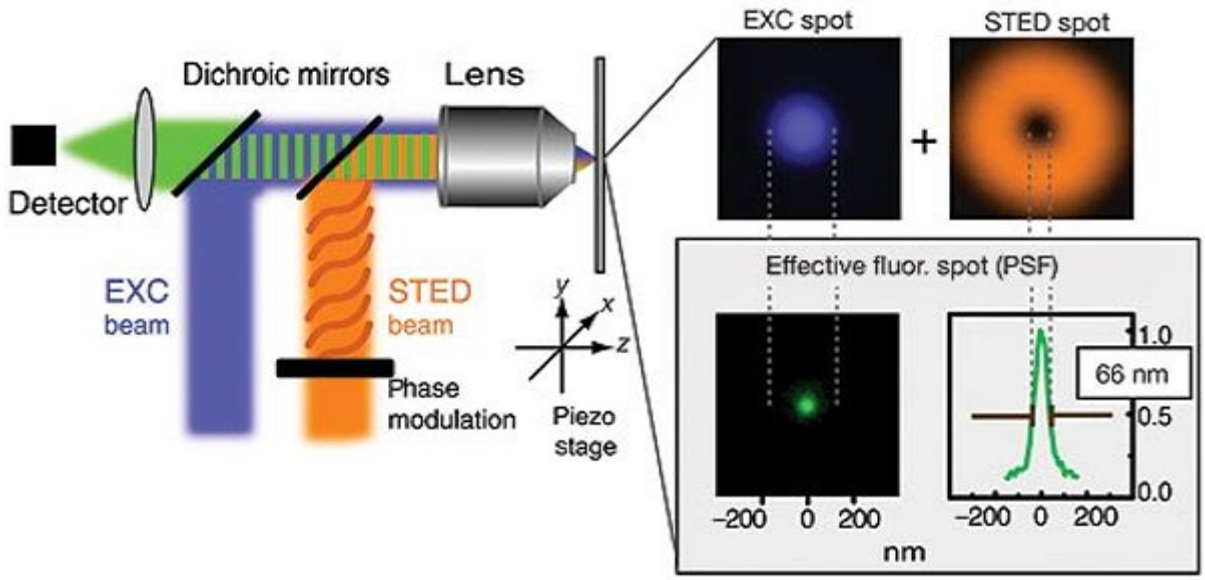

Figure 1.6 STED microscopy. Blue excitation light (EXC spot) combine with the STED-doughnut beam laser (STED spot) divulge the effective fluorescence spot (PSF) in X, Y focal plane with a full width at half maximum (FWHM) of 66nm which give an estimation of the resolution. Adapted from Willig, Rizzoli, Westphal, Jahn, & Hell, 2006

1.9 Scope of the study

Rapid structural modification of the spine head is well-known to be driven by synaptic activity and occurs on the scale of minutes (Bosch & Hayashi, 2012; C. H. Kim & Lisman, 1999). However, less is known about the structural remodeling of the PSD95 organization during LTP. Previous research, using 2-photon microscopy, has demonstrated an increase of PSD95 assembly size following activity-driven plasticity (Meyer et al., 2014, Bosch et al., 2014). Furthermore, electron microscopy has shown that the number of perforated PSDs increases following LTP and a STED microscopy study has demonstrated that PSD95 perforations exist *in vivo* (Masch et al., 2018; Monyer et al., 1992; Stewart et al., 2005; N Toni et al., 2001; Wegner et al., 2017). Nonetheless, 2-photon microscopy cannot reveal the nanoorganization of scaffold proteins due to the diffraction limit, electron microscopy cannot visualize the transformation of perforated PSDs due to fixation and with *in vivo* STED, only baseline changes have been explored. However, it is not known how PSD95 assemblies transform in shape and if these perforations coincide with changes in synaptic strength

such as induced by LTP protocols. Moreover, how do these induced changes affect the presynaptic active zone nanoarchitecture and AMPA receptor nanodomains organization? Therefore, my thesis aims to investigate the remodeling of pre- and postsynaptic structures after chemical LTP induction using STED nanoscopy. I performed live-cell STED imaging for up to 2h after LTP induction in CA1 hippocampal neurons and superresolved changes of endogenous PSD95 nanoorganization by using an antibody-like label. Moreover, I investigated the remodeling of the nanoorganization of the active zone protein Bassoon and AMPA receptor nanodomains in hippocampal neuronal cultures employing immunohistochemistry. I quantified the area of PSD95, Bassoon, and AMPA receptor nanodomains at different time-points, as well as the number of AMPA receptor nanodomains. To access the morphology of PSD95 and Bassoon assemblies, I did a qualitative analysis by attributing shape parameters to the nanoorganizations. A quantitative analysis of PSD95 morphology was also performed by defining and analyzing the filling ratio of PSD95 assembly per synapse. With these experiments, I showed the highly dynamic remodeling of PSD95 nanoarchitecture following LTP, which is accompanied by an increase of AMPA receptor nanodomains and changes in the nanoorganization of the active zone protein Bassoon.

2. Materials and methods

2.1 Neuronal hippocampal cultures

Primary neuronal hippocampal cell cultures were prepared under the sterile hood according to the protocol of D'Este et al., 2017 (D'Este, Kamin, Balzarotti, & Hell, 2017). The hippocampi of newborn Wistar rats (P1) were prepared under the microscope and collected in cold Hank's Solution (Sigma #H4891) composed of 4.2mM $NaHCO_3$, 12mM HEPEs, 33mM D-Glucose, 200µM kynurenic acid (Sigma #K3375), 100units/mL Penicillin and 100µg/mL Streptomycin (Millipore #A2213) at pH 7.4 and supplemented with 0.025% trypsin (Gibco #15090). As a next step, the hippocampi were enzymatically digested at 37°C. After an incubation time of 20 min, the digestion was blocked with Dulbecco's Modified Eagle Medium (Gibco 21969) supplemented with 10% Fetal Bovine Serum (heat-inactivated at 56°C for 30 min; Millipore #S0615), followed by a centrifugation for 5 min at 1000rpm. Subsequently, the neurons were washed in Hank's solution and dissociated in complete Neurobasal media composed of Neurobasal media (Gibco #21103) supplemented with 2% B-27 (Gibco #17504), 2mM L-Glutamine (Gibco # 25030), and 100 units/milliliter Penicillin and 100 µg/mL Streptomycin. Afterwards, the cells were counted with a *hemocytometer* (Brand; 717805) and plated at density of 180,000 cells/ml on 18mm 1.5 thick glass coverslips (Marienfeld # 0117580) in a 12-well plate. The coverslips were previously covered with 100µg/mL Poly-L-ornithine (Sigma #P3655) diluted in autoclaved and filtered ultrapure water (Sartorius), washed in phosphate buffered saline (PBS) pH 7.4, and coated with 1µg/mL Laminin (Corning #354232) diluted in Hank's Solution for adhesion of the cells on the coverslip. After being plated, the media of the neuronal hippocampal culture was changed for fresh complete Neurobasal solution 1 to 2 h after preparation and also on the next day. After 5 days in vitro at 37°C, 95% Oxygen (O_2), and 5% Carbon dioxide (CO_2), 5 µM of ß-D-arabinofuranoside (Sigma #C1768) was added to the cell cultures media to avoid development of glial cells. The cells were kept for 16 to 21 days in an incubator at 37°C, 95% O_2 and 5% CO_2 until treatment or fixation.

2.2 Organotypic hippocampal slice cultures

The organotypic hippocampal slice cultures were prepared from P5 C57BL/6N and C57BL/6J wild-type mice according to the protocol of Stoppini et al. (Stoppini, Buchs, & Muller, 1991). First, the brain was extracted and placed into a cold Hank's balanced salt solution (Gibco #24020091) supplemented with 27mM glucose, 1mM kynurenic acid, and pH 7.1. The hippocampus was then isolated and transferred to a chopper (McILWAIN tissue chopper from CAVEY Laboratory Engineering Co. LTD.) using a sterile Pasteur pipette. The hippocampus was sliced into coronal sections of 300µm thickness in a sterile hood. After careful separation, the hippocampal slices were then placed on a 0.45µm polytetrafluoroethylene membrane (Millipore #FHLC04700). The slices were maintained at the surface of the medium (1mL): 25% Basal Medium Eagle (Gibco #41010026) supplemented with 50% Minimum Essential Medium (Gibco #11012044), 2mM Glutamax (Gibco #35050038), 25% heat-inactivated horse serum (Gibco #26050088) and 32mM glucose via a 0.4µm cell culture insert of 30mm diameter (Millipore #PICM03050) placed in a 6-well plate. The organotypic hippocampal slice cultures were then incubated with 95% O_2 and 5% CO_2 for 18 to 23 days *in vitro* (DIV). The medium was exchanged three times per week and on the third day an inhibitor mix was added to the cells to avoid excessive glial cell growth. The inhibitor mixture contained: 1mM ß-D-arabinofuranoside, 1mM Uridine (Sigma #U3750) and 1mM 5-Fluoro-2'-deoxyuridine (Sigma #F0503).

2.3 Adeno associated virus transduction

For visualization of dendritic spines, the recombinant adeno associated virus (rAAV) rAAV-hSyn-DIO-myr-rsEGFP2-LDLR(ct)-WPRE with a double-floxed inverted open reading frame (DIO) was used under the control of the neuron-specific human synapsin-1 promoter (hSyn). This virus encoded for the reversible photoswitchable (rs) green fluorescent protein rsEGFP2 (emission λ 503 nm) with an N-terminal myristoylation motif (myr) that promoted dendritic membrane labelling, and the C-terminal (Ct) cytoplasmic domains of low density lipoprotein receptor (LDLR) to target the protein to the dendrite (Kameda et al., 2008). The rsEGFP2 is switched on by UV light (λ 408 nm) and switched off by the λ 480 nm excitation light. rsEGFP2 was used instead of rsEGFP due to a faster switching property, which is more convenient during live-STED imaging (Grotjohann et al., 2012). Furthermore, to target the PSD95 protein,

rAAV-ZFN-hSyn-DIO-PSD95.FingR-Citrine-reg.-WPRE was used. This virus expressed endogenous PSD95 with a transcriptionally regulated recombinant antibody-like-protein called FingRs (Fibronectin intrabodies generated with mRNA display) under the hSyn promoter (Gross et al., 2013). By using this antibody-like-protein, it is possible to label and visualize PSD95 without overexpression (Gross et al., 2013). The yellow fluorescent protein citrine was used to visualize endogenous PSD95 with an excitation maximum at 516nm and emission maximum at 529nm. To reduce the overall density of the fluorescent spines and PSD95s, but not to impair their brightness, all fusion proteins were generated as double inverted open reading frames (DIO). Therefore, low concentrations of the cre-recombinase encoding virus rAAV1/2-hSyn-CRE-WPRE were co-transduced with a high concentration of rAAV1/2-ZFN-hSyn-DIO-PSD95.FingR-Citrine-reg.WPRE and rAAV1/2-hSyn-DIO-myr-rsEGFP2-LDLR(ct)-WPRE to reduce the overall labelling density. All viruses had a mixed serotype consisting of serotype 1 and 2. The cloning and production of all used AAVs was carried out by Dr. Waja Wegner and is described for most of the used viruses in detail in Wegner et al., 2020 (Wegner W, Steffens H, Gregor C, Wolf F, 2020). However, in this report, a slightly different virus was used for the visualization of the membrane: rAAV-hSyn-DIO-myr-EGFP-LDLR(ct)-WPRE, where rsEGFP2 is replaced by an EGFP tag.

To investigate PSD95 and the spine head during live-STED imaging, organotypic hippocampal slices were transduced 2 days after preparation. The slices were first placed in a 35 mm petri dish with a small metal weight to maintain the slice in the bottom and immersed in growth medium. Afterwards, a mixture of rAAV1/2-ZFN-hSyn-DIO-PSD95.FingR-Citrine-reg.WPRE, rAAV1/2-hSyn-DIO-myr-rsEGFP2-LDLR(ct)-WPRE and rAAV1/2-hSyn-CRE-WPRE was transduced in the CA1 region of the organotypic hippocampal slice using a 20x objective (LEICA Germany #049) under the light microscope. The viruses were transduced via a borosilicate glass capillary (ID: 0.68mm, OD: 1.2mm; Kwik-fil, World Precision Instruments, Inc. #1B150F-4) that was angled at 50 degree with the slice using a micromanipulator (NARISHIGE Japan). Finally, ~50nL of the virus mixture was pressure injected with 10 pulses at 15 psi in the CA1 region using an Intracellular Microinjection Dispense System (PICOSPRITZER III, Parker Instrumentation). After transduction, the slices were placed back in a 0.4 µm

cell culture insert and incubated in an atmosphere of 95% O_2 and 5% CO_2 at 37 °C until the STED imaging session (16 to 21 days).

2.4 Treatment and Chemical LTP

The hippocampal cultured neurons were used between 16 to 21 days for chemical LTP induction. Synaptic NMDA receptors were activated via a Base solution (105mM NaCl, 2,4mM KCl, 10mM HEPES, 10mM D-glucose, 2mM $CaCl_2$, pH7.4, and ~240mOsm), without $MgCl_2$ supplemented with 200µM glycine (Sigma #G8790) and 20µM bicuculline (Hellobio #HB0893) (Molnár, 2011). The administration of bicuculline removed GABAergic inhibition in the neural network, while glycine is the co-agonist of the NMDA receptor known to activate NMDA receptors in a free Mg^{2+} solution (Shinya Ueno et al., 1997). Chemical LTP was applied to the hippocampal cultured neurons for 5 minutes at 37°C. Following the incubation, the neurons were immediately fixed (Time point 0 min). For the other time points, the cover glasses were transferred back into the culture medium (37°C) and fixed accordingly after 30, 60, or 120min post LTP induction. As a control, coverslips were put into Base solution supplemented with 2mM $MgCl_2$ for 5 minutes at 37°C instead of the chemical LTP solution. Depending on the different points in time (0, 30, 60 or 120min), the cover glass was fixed immediately or transferred back into normal media.

For chemical LTP induction during live-STED imaging of hippocampal organotypic slices, 200µM glycine and 20µM bicuculline were added to artificial cerebrospinal fluid (ACSF) solution (128 mM NaCl, 20 mM KCl, 10 mM KH_2PO_4, 26 mM $NaHCO_3$, 10 mM glucose, 2 mM $CaCl_2$, pH 7.4 and ~ 320 mOsm) free of Mg^{2+} and applied to the hippocampal slice for 10 min. However, to avoid spontaneous synaptic activity before induction of LTP, the slices were maintained in an ACSF solution supplemented with 50 µM *D-2-amino-5-phosphonovaleric acid* (APV) for 20 minutes. This chemical compound, APV (Hellobio #HB0225), is a competitive and selective NMDA receptor antagonist that blocks NMDA receptor activation. Afterward, chemical LTP was induced for 10 min and then the slices were perfused with ACSF for the rest of the experiment. To relate the changes that occur during LTP induction to the activation of the NMDA receptor, a condition using APV was implemented. The protocol was the same as described above, but 50µm of APV was added in all solutions (ACSF and chemical

LTP). The basal activity was also investigated in the control condition where the hippocampal organotypic slices were maintained in ACSF during the whole experiment. Finally, during the live-STED imaging sessions, the hippocampal slices were preserved at 30°C during the whole time-lapse via a solution heater (QE-2 exchange platform; SF-28 solution heater and heater Controllers TC-344C, all from Warner instruments), the ACSF solution and its variants were continuously *infused* with 95% O_2 / 5% CO_2 and the perfusion system (Gilson) continuously delivered the solution with a flow of 1 mL/min.

2.5 Immunocytochemistry

The cultured hippocampal neurons were fixed for 1 hour in a Glyoxal solution (3% v/v Glyoxal (Sigma #128465) and 0.75% acetic acid (Roth #3738) diluted in ultrapure water (Sartorius)). Glyoxal fixation was used instead of 4% paraformaldehyde (PFA) because the efficiency to cross-link of proteins is improved in glyoxal fixative and more rapid than PFA (Richter et al., 2018). Furthermore, glyoxal is less toxic and enhances the preservation of the cell morphology compared to PFA fixative (Richter et al., 2018). Glyoxal solution was adjusted to pH 4 (Bassoon) or 5 (AMPA receptors), depending on the primary antibody used. After fixation, cells were washed three times with 0.1M PBS/glycine and then permeabilized for 30 min in blocking solution (2% normal goat serum (Sigma, #G9023), 0.1% Triton X-100 (Sigma, #T8787) in PBS). Primary antibody solutions Bassoon anti-rabbit (Synaptic Systems, #141013, 1:500, PSD95 anti-mouse (Neuromab, #75-028, 1:300), and Alexa Fluor 488 Phalloidin (Invitrogen #A12379, 1:600) were diluted in blocking solution and incubated for 2 hours at room temperature. Phalloidin antibody binds to actin filament and was used during the primary antibody staining of PSD95 and Bassoon to observe the spine heads during the imaging session. In the case of surface labeling of AMPA receptors via anti-mouse monoclonal antibody specific to N-terminal extracellular domain of the GluA2 subunit (Millipore #MAB397, 1:500), no permeabilization was done during the blocking solution incubation of 30 min and antibody incubation of 2h. So, Triton X-100 was not added to the blocking solution. After the GluA2 antibody incubation, the cells were permeabilized in blocking solution supplemented with Triton X-100 for 30 min to access PSD95. Then, PSD95 anti-rabbit (Cell signaling #3450, 1:300) with AlexaFluor 488 and Phalloidin (1:600) was added to the blocking solution (with Triton X-100) and incubated for 2h at

room temperature. Afterwards, three washing steps in PBS were done before the secondary antibody incubation. Secondary antibody incubation was done at 4°C overnight with STAR RED anti-rabbit (Abberior #STRED-1002, 1:50 in blocking solution (with Triton X-100) and Alexa594 anti-mouse (Thermo Fisher Scientific, #A-11005, 1:100). Finally, three last washes in PBS were performed before mounting the coverslips on slides (Thermo Scientific™, #11386211) with Mowiol (Roth, #0713) to perform two-color STED imaging combined with confocal imaging of Phalloidin.

2.6 STED nanoscopy

2.6.1 Microscope adjustment

The STED beam doughnut-shape was first adjusted using 150nm gold beads (BBI Solutions, #EM.GC150). Through the reflection of the STED beam by the gold beads, the doughnut-shaped point-spread function (PSF) was detected in the X, Y plane (Figure 2.1.A). Cross-section planes along the X, Z and Y, Z show two maxima. These maxima were aligned to be symmetric by moving the vortex phase plate with the aim of obtaining a round and balanced doughnut-shape in the X, Y plane (Figure 2.1). Using the gold beads, the blue light excitation, for the live-STED imaging set-up, was centered in the middle of the STED doughnut-shaped beam in the X, Y focal plane so that the excitation spot was depleted only at the periphery. For two-color STED imaging, the red and orange light excitations were superposed and centered in the middle of the STED doughnut-shaped beam. Afterwards, the detection of the blue excitation light was adjusted using a Rhodamine 110 dye solution (excitation: 500 nm/emission: 522nm) for the live-STED imaging setup. For the two-color STED set-up, the Atto 590 dye (ATTO-TEC; excitation: 593 nm/emission: 622nm) was used to optimize the detection of the orange excitation light and STAR RED (Abberior) a red-emitting rhodamine *dye* (excitation: 630 nm/emission: 660nm) *was employed for the detection of red excitation light.* The STED beam pulse was calibrated to enhance the STED beam depletion. Finally, using 40nm yellow-green beads (Invitrogen, #F8795) for the live-STED set-up or 40nm Crimson beads (Invitrogen) for dual-color STED setup, the resolution of the microscope was confirmed before each experiment (Figure 2.1).

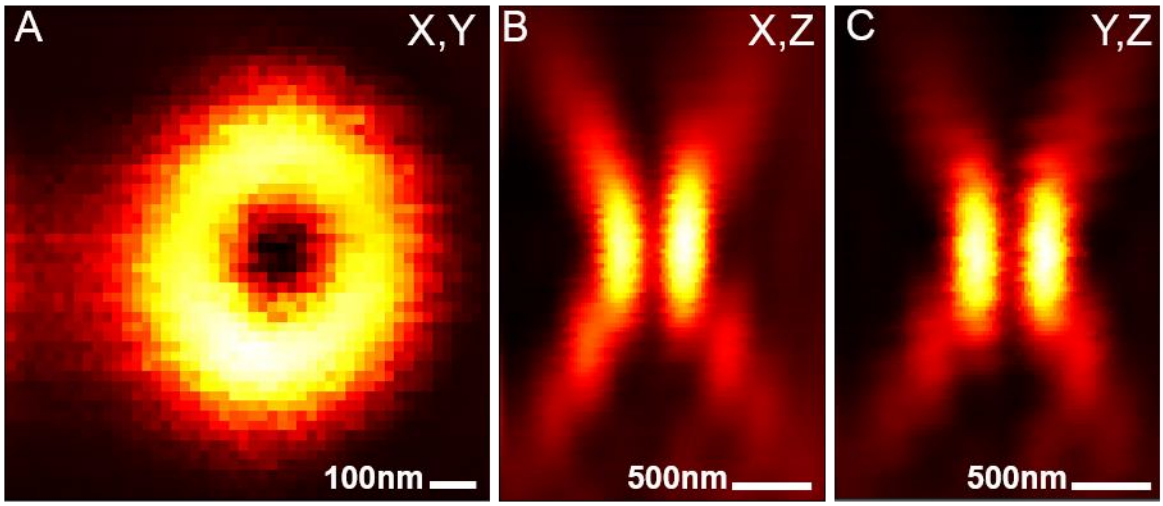

Figure 2.1 STED beam reflection on gold beads. (A) STED doughnut-shaped beam in the X, Y focal plane. **(B)** STED X-shape in the X, Z focal plane. **(C)** STED X-shape in the Y, Z focal plane. A 63X water objective with 1.2 numerical aperture and a correction collar was used to observe the reflection of the STED beam at wavelength of 595nm.

2.6.2 Live STED-imaging

Organotypic hippocampal slices were used for live-cell STED imaging between 16 to 21 days after viral transduction. Live-cell STED imaging was performed via a home-built upright microscope (Willig et al., 2014). The organotypic hippocampal slice was first placed in a 35 mm petri dish and glued to the bottom of the dish with picodent (picodent twinsil, #1300 1000) to prevent the slice moving between each exposure with STED nanoscopy. The slice was then submerged in ACSF solution as described in Section 2.4. During live-STED imaging, a stack of five pictures were taken over 2.5 µm with a ΔZ of 500nm and a dwell-time of 4µs via Imspector software (Abberior Instrument). The dimension of the images taken was 30 x 30µm in the X, Y plane with a pixel size of 30nm. A confocal image was taken to visualize the spine head with AAV-myr-rsEGFP2 and STED imaging was used to visualize PSD95 via AAV-PSD95-FingR-Citrine expression. The images were collected with a water objective of 63x with 1.2 numerical aperture and a correction collar (Leica Germany #506356). The correction collar was adjusted to optimize the performance of the objective in the tissue and correct for spherical aberration. During live cell imaging, a stack of STED and confocal pictures were acquired 4 times: either before LTP, during LTP, 30 and 60min after LTP, or the other imaging scheme consisting of before LTP, 30, 60, and 120min after LTP. STED and confocal imaging were not performed simultaneously, PSD95 was first recorded with STED using blue light excitation, and immediately afterwards a

confocal image of myr was taken with an additional UV light to switch on the fluorophore. Thus, all images of rsEGFP2 do also contain the signal of Citrine. Since PSD95-Citrine was much darker than myr-rsEGFP2, no image processing such as subtraction of the Citrine signal was required. The emission and excitation wavelength of PSD95 and myr and the blue light excitation (Ex: 480nm) and detection window (Det: 535/ 50nm) of the microscope are shown in Figure 2.2.A. The crosstalk of rsEGFP2 activated or not by the UV light are represented in Figure 2.2.B. Finally, the power of the blue light was always set at 5.5µW, the power of the UV light to excite the rsEGFP2 was 2mW and the power of the STED laser was ~15mW in the back-aperture of the objective. STED power of ~15mW allows the resolution of PSD95 with an average FWHM of 75nm (Figure 2.2.C-E).

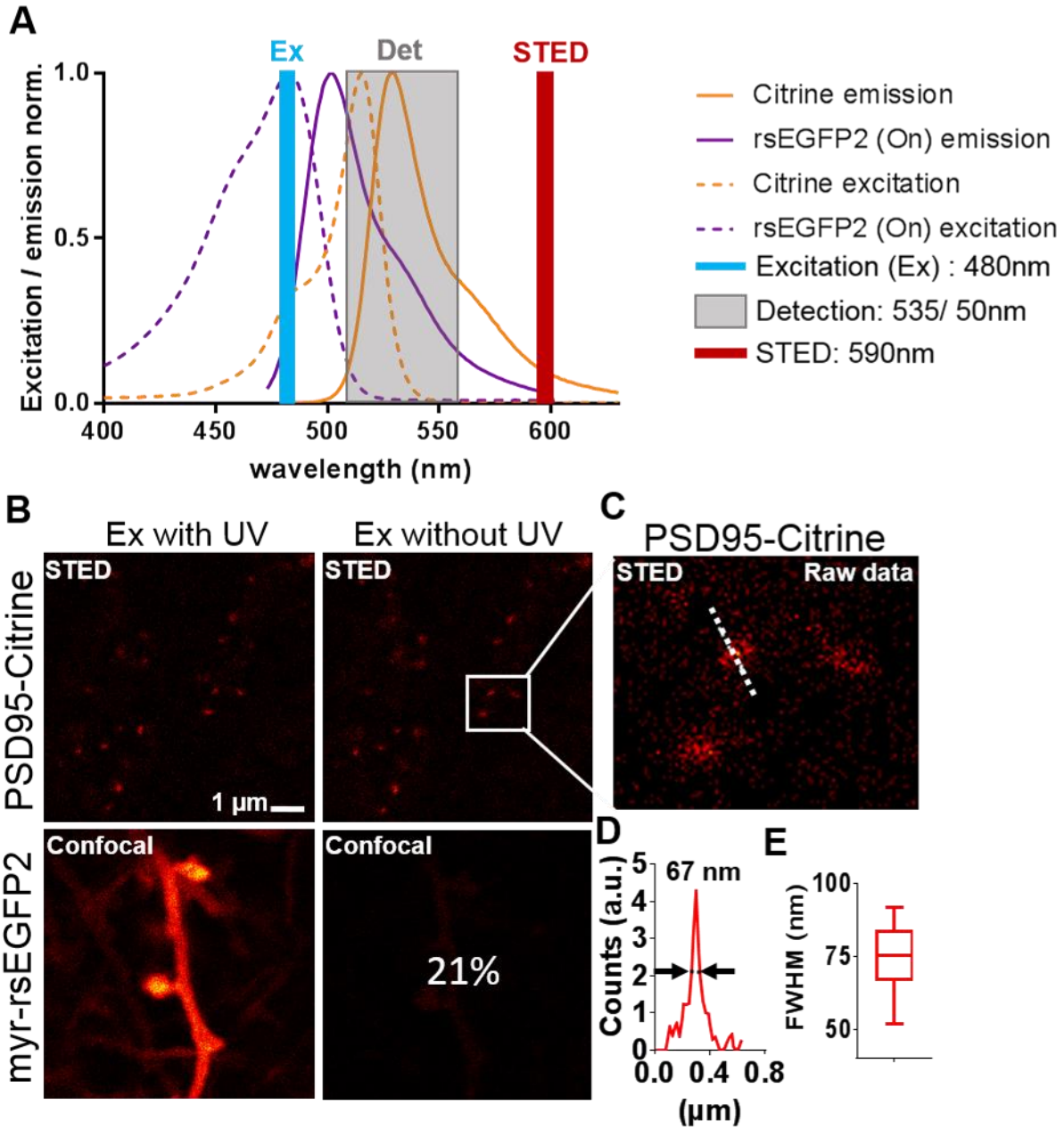

Figure 2.2 Detection of PSD95-Citrine and myr-rsEGFP2. (A) Blue light excitation (Ex) and the detection window (Det) of the STED set-up used for live-cell STED imaging with emission and excitation wavelength of Citrine and rsEGFP2 fluorophores. **(B)** Single virus transduction of AAV-PSD95-FingR-Citrine or AAV-myr-rsEGFP2 in hippocampal organotypic slices and their expression with or without UV light (raw data). AAV-myr-rsEGFP2 presented 21% crosstalk when switching off. **(C)** Magnification of the three PSD95 assemblies shown in the white box in B. **(D)** FWHM of PSD95 represented with a line profile in (C). Estimation of the resolution is determined using FWHM of Gaussian curve fits with an average of 3 lines per profile. **(E)** Average FWHM of a 10 line profile as exemplified in (D). Data presented as median ± standard deviation (SD)

2.6.3 Two-color STED imaging

An inverted STED microscope built by Dr. Joris van Dort was used to image the triple color immunostaining of either Bassoon/PSD95/Phalloidin or AMPA receptor/PSD95/ Phalloidin via the software Imspector (Abberior Instruments). An image collection of 5 pictures of 30 x 30µm in X, Y dimension with a pixel size of 20nm was collected over 2µm with a ΔZ of 400nm. The stack was taken with an oil objective of 100x magnification with 1.4 numerical aperture (Leica Germany #506316) and a dwell-time of 5µs. Confocal microscopy was used to image Phalloidin and two-color STED microscopy was performed to image Bassoon/PSD95 and AMPA receptor/PSD95. The crosstalk of Bassoon/PSD95 or AMPA receptor/PSD95 was revealed with single color staining of Alexa 594 or STAR RED as shown in Figure 2.3. B and C. Finally, the immunostaining of Bassoon with STAR RED secondary antibody (Det: 692/40nm) was imaged with a red-light excitation (Ex: 630nm) of 18µW, PSD95 with Alexa 594 secondary antibody (Det: 620/14nm) with an orange light excitation (Ex: 586nm) of 15µW, and a blue light excitation (Ex: 480nm) of 8µW to reveal the spine head morphology with Phalloidin. For the AMPA receptor/PSD95/Phalloidin staining, AMPA receptor was imaged with the orange light excitation of 38µW, PSD95 with the red-light excitation of 18µW, and Phalloidin with the blue excitation of 8µW. The excitation and emission spectrum of secondary antibody Alexa 594 and STAR RED as well as the orange and red-light excitation and the detection window of the microscope are also presented in Figure 2.3.A. A high STED power of ~230mW was used for dual-color STED imaging, resulting in an average FWHM of the smallest particle of 57nm for AMPA receptor + Alexa 594 and 51nm for PSD95 + STAR RED, 54nm for Bassoon + STAR RED and 55nm for PSD95 + Alexa 594 (Figure 2.3.B,D).

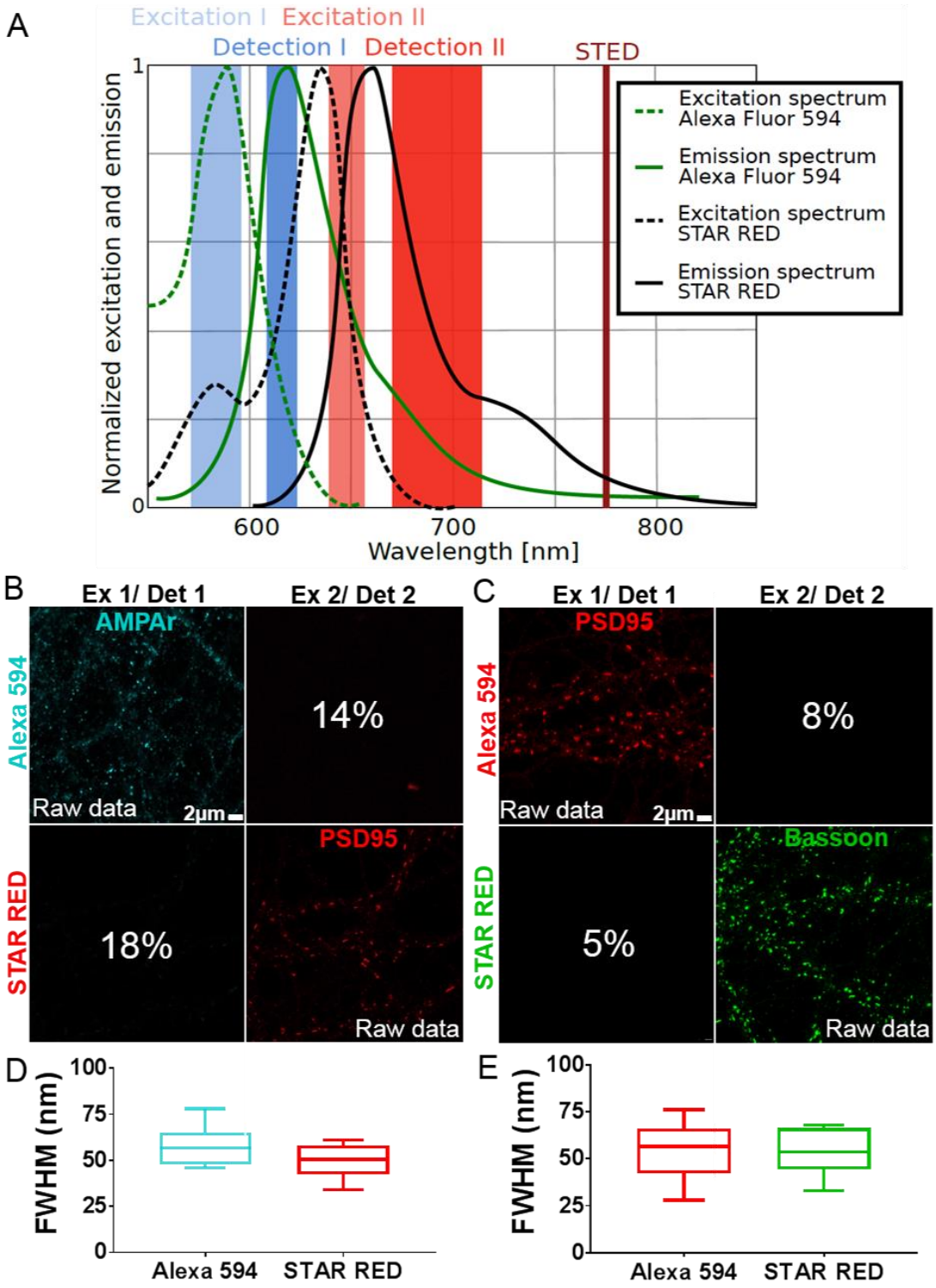

Figure 2.3 Detection of AMPA receptor, PSD95 and Bassoon antibody staining. (A) Orange (Ex 1) and red (Ex 2) light excitation and the detection windows (Det1/ Det 2) of the dual-color STED set-up with emission and excitation wavelength of Alexa 594 and STAR RED secondary antibody. Adapted from van Dorth 2018 (Van Dort, 2018). **(B)** Single color antibody staining of AMPA receptor (AMPAr) + Alexa 594 and PSD95 + STAR RED in neuronal hippocampal cultures of 17 DIV and their crosstalk. Crosstalk of AMPA receptor + Alexa 594 is up to 14% and PSD95 + STAR RED 18%. **(C)** Single antibody staining of PSD95 + Alexa 594 and Bassoon + STAR RED in neuronal hippocampal cultures of 17 DIV and their crosstalk. Crosstalk of PSD95 + Alexa 594 is 8% and Bassoon + STAR RED 5%. **(D)** FWHM of the smallest particle of AMPA receptor + Alexa 594 and PSD95 + STAR RED revealed by two-color STED microscopy in the background of sample (B), n=10. **(E)** Same as (D) but for PSD95 + Alexa 594 and Bassoon + STAR RED, in the background of sample (C) n=10.

2.7 Electrophysiological recording

In collaboration with Dr. ChungKu Lee (laboratory of Prof. Dr. Rhee), whole-cell voltage clamp recordings were performed in hippocampus CA1 pyramidal neurons. The hippocampal slices were used between 16 to 21 days after virus transduction. The pyramidal neurons of CA1 were located via the fluorescence expression of AAV-PSD95-FingR-Citrine and AAV-myr-rsEGFP2 and visualized with an upright epifluorescence microscope (Zeiss examiner D.1). CA1 pyramidal neurons were patched to investigate mEPSCs. The mEPSCS were recorded until 1h after chemical LTP induction. The organotypic hippocampal slices were first immersed in extracellular recording ACSF containing in mM: 120 NaCl, 20 KCl, 10 KH_2PO_4, 26 $NaHCO_3$, 10 glucose, 2 $CaCl_2$, with a pH of 7.4 and 302 mOsm. A stable baseline was recorded, followed by 10 minutes of chemical LTP (ACSF without $MgCl_2$ + 200µM glycine and 20µM bicuculline). Then recorded for another hour in the standard ACSF. For the control condition, mEPSCs were recorded for 1h in standard ACSF solution. All extracellular solutions were continuously *infused* with carbogen (95% O_2 / 5% CO_2) during the experiment and supplemented with the voltage-gated sodium channel blocker tetrodotoxin (TTX) (1µM, Tocris #1078), to prevent action potentials during recording. Furthermore, for control and LTP conditions, ACSF was supplemented with 20µM bicuculline to avoid the contamination of inhibitory currents during recordings of mEPSCs. The patch pipette (2.5-3.0 MΩ) was filled with an intracellular solution composed of 138mM K-gluconate, 16.8mM HEPES, 10mM NaCl, 1mM $MgCl_2$, 4mM ATP-Mg, 0.3mM GTP-Na and 0.25mM K-EGTA at pH 7.38 and 310 mOsm. The recordings were performed at room temperature and the recorded CA1 pyramidal neurons were kept at a holding potential of -70mV, using a double patch-clamp EPC-10 amplifier (HEKA) with Patchmaster software. The mEPSC recording and analysis was performed by Dr. ChungKu Lee and only cells that exhibited a mEPSC amplitude increase after chemical LTP induction were included in the analysis.

Whole-cell patch-clamp recordings of neuronal hippocampal cultures (16 to 21 DIV) were done in collaboration with Dr. Erinn Gideons. The neurons were visualized and targeted via an inverted microscope (Olympus IX51). Base solution (140mM NaCl, 2,4mM KCl, 10mM HEPES, 10mM glucose, 2mM $MgCl_2$ and 2mM $CaCl_2$, pH 7,4 and 287 mOsm) supplemented with 300nM TTX was used as extracellular recording

solution before and after chemical LTP induction. After 10 min of recording baseline activity in Base solution, chemical LTP was induced for 5 minutes with a Base solution without Mg^{2+} and supplemented with 200µM glycine/20µM bicuculline. Then mEPSCs were recorded for another 30 min after chemical LTP stimulation. The intracellular solution contained in mM: 136 KCl, 17.8 HEPES, 1 EGTA, 0.6 MgCl, 4 NaATP, 0.3 Na2GTP, 15 creatine phosphate and 5 U/mL phosphocreatine kinase at 315-320mOsm and pH7.4. The experiment was performed at room temperature and the CA1 pyramidal neurons were kept at a holding potential of -70mV using a Multiclamp 700 amplifier and Clampex software. The recording of mEPSCs and the data analysis were done by Dr. Erinn Gideons.

2.8 Image analysis

All images were analyzed with Fiji/ImageJ software (National Institutes of Health). For the live-cell imaging experiments, the spine head area and the PSD95 expression corresponding to the same spine head in the focal plane X, Y were analyzed for every picture of the time course. The images were first smoothed in ImageJ to average each pixel with 3 x 3 neighborhood and the background was subtracted to improve the contrast. An example of smoothed and background suppression of PSD95 is presented in the Appendix, Figure A1. A-C. The PSD95 area was then analyzed using the length and the width of the PSD95 nanoarchitecture to calculate the area of a fitted ellipse. PSD95 was analyzed as one organization per spine head. To measure the spine head area, the number of pixels was multiplied by the pixel size (30nm). The changes in both the PSD95 area (Δ PSD95 area) and the spine head area (Δ spine head area) at each time point during the time course of the experiment was calculated as $\Delta A/A_0$. The value A_0 corresponds to the initial time point (before LTP) and ΔA the difference between the areas at time point t (0, 30, 60 or 120 min after LTP) with the initial time point A_0. PSD95 morphology was allocated via qualitative analysis. Macular morphology was assigned when the spine head contained only one PSD95 without perforation. Perforated morphology was assigned when PSD95 had a U-shape or ring-like shape and presented a hole of at least 3 x 3 pixels (90nm x 90 nm) in the middle of the structure to exclude noise. Segmented PSD95 was attributed when more than one PSD95 cluster was found in one spine and the clusters were separated by 3 pixels (90nm) or more. To confirm the morphology assigned to each PSD95, the filling ratio

was also calculated via the equation: $\frac{\Sigma\, Pixel\ area}{area\ \ fit\ ellipse}$, which gave access to the number of black pixels in the fitted ellipse area of PSD95**.** The summation of pixel area was obtained via the number of pixels multiplied by the pixel size of 30nm and the area of the fitted ellipse was obtained as described above. Moreover, PSD95 and spine head dynamics were obtained via the Kesten process formulation: $\mu\ (x_t) = (< \epsilon - 1 > x_t + < \eta >)$, where the size fluctuation $\mu\ (x_t)$ is plotted as a function of initial size (Hazan & Ziv, 2020). Size fluctuation $\mu\ (x_t)$ of PSD95 corresponds to ΔPSD95 area and the initial size is A_0. The slope of the linear regression of this function represented the multiplicative component $< \epsilon - 1 >$ and the intercept, the additive component $< \eta >$. The multiplicative component is state-dependent on area fluctuation while the additive one is state-independent on size fluctuation (Hazan & Ziv, 2020; Ziv & Brenner, 2018). Furthermore, after chemical LTP induction, the spines were considered as potentiated when the spine head area displayed an increase of at least 15% (1 x standard deviation (SD) during baseline, referred to Appendix Figure A1.D) at 60 and 120min after stimulation. The other spines that did not display an increase in size of 15% at 60 and 120min after LTP stimulation were defined as unpotentiated spines. Finally, the data of two different time courses after LTP induction were pooled together into a 5-time point series because only 1-time point is different. All experimental conditions were the same and only those spines in which PSD95 was present in at least 3 of 4 time-points during the time courses were analyzed.

For the analysis of two-color STED images, the pictures of AMPA receptor/PSD95/Phalloidin and Bassoon/PSD95/Phalloidin staining were smoothed and the background was subtracted in ImageJ using a macro kindly given by Dr. Heba Ali (Appendix Figure A4-A5). The area of Bassoon, PSD95, and AMPA receptor nanodomains were obtained by the summation of the pixel area. PSD95 and Bassoon were analyzed as one morphology per spine head and only Bassoon in close colocalization to PSD95 was analyzed. PSD95 and Bassoon morphology were obtained via the qualitative analysis as previously described. Finally, only the AMPA receptor nanodomains located on PSD95 nanorganizations were analyzed and the number of nanodomains was determined by the number of clusters, separated by 3 pixels (60nm) or more, located on PSD95 nanoarchitecture.

2.9 Statistical analysis

The results from the area fluctuation, mEPSC, filling ratio, and the number of AMPA receptor nanodomains are represented as mean ± standard deviation of the mean (SEM), and the area (in μm^2) and the ratio of PSD95/spine head area are represented as median ± 95% confidence interval (CI). There was one exception, fluctuation of the spine head area during baseline was presented as SEM ± SD (Appendix Figure A.1). When comparing different conditions (more than 2), the unpaired one-way analysis of variance (ANOVA) test was used for normally distributed data. Kruskal-Wallis (K-W) test was performed for non-normally distributed results. When only two conditions were compared, Mann-Whitney (M-W) test was used. An exception for size distribution and morphology distribution analysis of PSD95 and Bassoon, Kolmogorov-Smirnov (K-S), a cumulative distribution comparison test, was used instead. For analyzing mEPSCs during chemical LTP of hippocampal neuronal cultures, Wilcoxon paired T-test was used to compare the before time point to the 30 min after chemical LTP stimulation time point (Figure 3.8) and a paired one-way ANOVA Friedman test was performed to compare area fluctuation of PSD95 and spine head after each image collection taken with STED microscopy (Figure A1). Furthermore, for the correlation and dynamics analysis, the slope and the intercept of the linear regression were compared using the analysis of covariance (ANCOVA) test. All tests are named in the legend of each figure. Finally, only the graph “Number of AMPAr cluster on different PSD95 morphology” and “Bassoon architecture on different PSD95 morphology” were made by Microsoft Excel (Figure 3.10.D and 3.12.E). All of the other graphs, as well as the statistical analyses, were generated via GraphPad Prism software. A table of the number of analyzed spines and experiments performed are show in table A1 and table A2.

3. Results

The aims of my project are: i) to study the morphological changes of PSD95 induced during LTP at nanoscale resolution ii) to investigate the impact of such structural changes on the active zone protein Bassoon and AMPA receptor nanodomain organization. To answer those two objectives, this chapter is divided into two sections. In the first part, changes in the area and morphology of PSD95 are investigated after chemical LTP induction using time-lapse live STED imaging of endogenous PSD95 in CA1 hippocampal organotypic slices. In the second part, the assembly of AMPA receptor nanodomains on different PSD95 architectures is studied, as well as the area and morphology of Bassoon, at different time points after LTP stimulation. These results will provide insight in the nanoplasticity of PSD95 remodeling after changes in synaptic activity.

3.1 Structural LTP of spine heads and endogenous PSD95

To achieve the first objective, live-STED nanoscopy was used to access the nanoscale organization of PSD95 over a 2h time-lapse period. To image PSD95 and the spine heads, adeno-associated viral particles (AAV) encoding for PSD95-FingR-Citrine and Myr-rsEGFP2 were transduced into CA1 Schaffer collateral synapses of an organotypic hippocampal slice (Figure 3.1.B). PSD95 was tagged with a transcriptionally regulated recombinant antibody-like-protein termed FingR in order to reveal the endogenous PSD95 expression without overexpression artifacts (Gross et al., 2013). The spine head was targeted via a myristoylation motif (myr), which leads to dendritic membrane labelling. After 16 days of virus transfection, STED images of PSD95 and confocal images of the spine heads were taken before and after chemical LTP induction to assess the structural changes of PSD95 during activity-driven plasticity. Before performing live-STED imaging, various STED parameters and PSD95 expression needed to be adjusted as explained in the following section.

3.1.1 Resolution and area distribution of PSD95

Before investigating endogenous PSD95 remodeling over a time-lapse with super-resolution STED, various concentrations of AAV-PSD95-FingR-citrine in CA1 Schaffer collateral synapses were tested and STED parameters were optimized to obtain the

best resolution in order to reveal PSD95 nanoorganization. To minimize photobleaching of the fluorophore by repeated STED beam activation, I also tested different excitations and STED powers. I explored AAV-mediated co-expression of PSD95-FingR-citrine and Myr-rsEGFP2 in CA1 hippocampal organotypic slices to minimize the crosstalk between the fluorescence emitted by rsEGFP2 in on/off state (as explained in Figure 2.2.B) and to increase the detectable fluorescence of endogenous PSD95. An example of the co-expression in a CA1 hippocampal organotypic slice after optimization is presented in Figures 3.1.A and B. Using myr-rsEGFP2 co-expressed with PSD95-FingR-citrine enabled the use of STED microscopy with a single excitation and single detection channel (Figure 2.2.A). The fluorescent protein rsEGFP2 is reversibly switchable, emitting fluorescence in a similar spectral range as EGFP (peak at 507nm). The protein can be switched on by UV light and switched off by 480nm excitation light (Figure 2.2.B). The main advantage of using only one detection channel at 535nm is that a broad detection window of 50nm can be chosen. This broad detection window allows for imaging of a larger spectral range of fluorescence than when using EGFP and Citrine (Wegner W, Steffens H, Gregor C, Wolf F, 2020) leading to a better detection of PSD95 fluorescence (Figure 2.2.C-E).

Furthermore, the parameters of image acquisition were adjusted to optimize the viability of the neurons and minimize the bleaching of PSD95 fluorescence and the photo damage induced during the live-cell STED imaging. Dwell time was adjusted to 4µs, heating of the sample chamber was set to a bath temperature of 30°C and STED laser power was adjusted to ~15mW. With these settings it was possible to detect the fluorescence emitted by PSD95-FingR-citrine following four repeated z-stacks of STED images (Appendix figure A1.A-C). Unfortunately, partial bleaching of PSD95-FingR-citrine could not be avoided while conserving a good resolution. After optimization and reduction of the STED laser power to ~15mW, nanoscale details of the PSD95 substructure with an average Full Width at Half Maximum (FWHM) of ~75nm were observed (Figure 3.1. C, D and Figure 2.2.E). However, the area of PSD95 was slightly affected by repeated exposure to the STED laser due to the bleaching. To quantify this effect, I performed a live-cell STED imaging during a short time-lapse employing the same settings. Under the basal condition, a STED picture was taken at intervals of 30 seconds for a total of 4 STED images in 1.5 minutes. PSD95 area was reduced 6% after the second image, 7% after the third, and 14% after the fourth picture (Appendix

Figure A1.E). The area of the spine head, which was recorded in confocal mode, did not change over the 4 image repetitions taken at 30sec intervals (Appendix Figure A1.D).

In order to study the area covered by PSD95 during LTP and its expansion during structural remodeling, the area of the complete PSD95 structure per spine was approximated by fitting with an ellipse. The area of the ellipse was calculated by: area = π*(a/2)*(b/2) with PSD95 length "a" and width "b" (Figure 3.1.E). In contrast to summating the number of PSD95 pixels, the current method can detect expansion of the molecule in case of a new PSD95 cluster/segment development, or PSD95 clusters moving away from each other. The area distribution of PSD95 assemblies using the length and the width to fit an ellipse is represented in Figure 3.1.E. It reveals a skewed distribution of the PSD95 area with an average of 0.21 ± 0.009 μm² (median ± 95% CI).

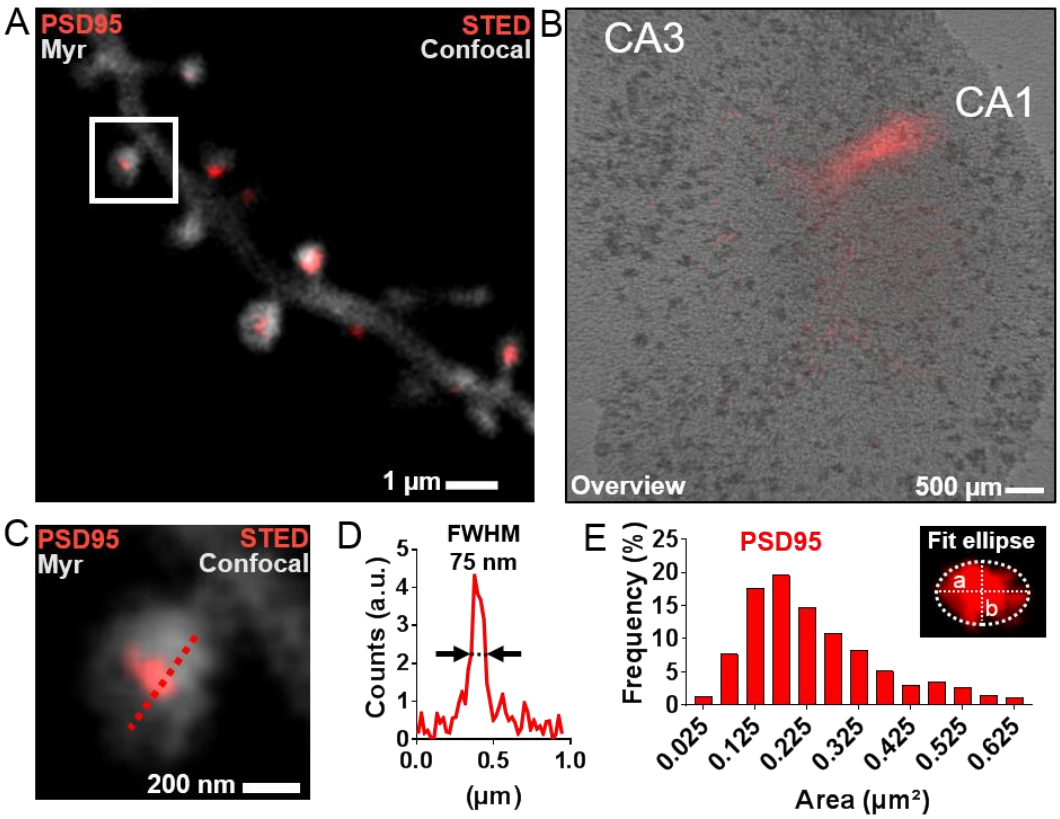

Figure 3.1: STED nanoscopy of endogenous PSD95 and spine morphology (A) Hippocampal neurons expressing PSD95-FingR-citrine were recorded with super resolution STED and Myr-rsEGFP2 with confocal imaging. **(B)** Overview of a mouse hippocampal organotypic slice and the AAV transduction in the CA1 (in red). **(C)** Magnification of white box in A, showing a spine head containing a PSD95 cluster **(D)** Line profile of PSD95 represented in C. Resolution is approximated using full-width at half-maximum (FWHM) of Gaussian curve fits of line profiles of an average of 3 lines **(E)** Distribution of PSD95 area (n=992 spines) with a bin width of 0.05µm². The area is obtained using an ellipse fit of the length (a) and width (b) of PSD95 fluorescent images in the X, Y focal plane. Imaging parameters are listed in Table A1.

3.1.2 LTP leads to spine head enlargement and PSD95 expansion

To explore the dynamics of PSD95 nanoorganization during activity-driven plasticity, chemical LTP was induced using 0 Mg^{2+}/ 200µM Glycine/ 20µM Bicuculline while PSD95 dynamics were revealed by live-cell STED imaging. The temporal sequence for LTP induction used during live-cell imaging is illustrated in Figure 3.2.A. Before LTP induction, hippocampal organotypic slices were put in ACSF solution containing APV, leading to blockage of basal neuronal activity induced by NMDA receptors for 20min. The first image (before LTP) was taken about 5min before LTP was induced. Subsequently, the perfusion was changed to the chemical LTP cocktail and then changed back to ACSF after 10min of stimulation. STED imaging during and after LTP was performed in two different time courses. First, at the time-points: before LTP (-15min), during LTP incubation (-5min) and at 30min and 60min after LTP induction to

observe the changes related to the early phase of LTP. The second time-lapse was performed at the time-points: before LTP (-15min) and at 30min, 60min, and 120min after LTP induction, which provided information about the late phase of LTP. As such, the -5min time point was changed for 120min in the latter set. As the STED parameters remained the same, the data were pooled into a 5-time point series to display the changes of PSD95 and the spine heads from before LTP induction (-15min) until up to 2h after stimulation. As the control condition, live-cell STED imaging was performed in ACSF. For the APV control (NMDA inhibitor), 50µM of APV was added to chemical LTP cocktail and ACSF solutions during the time course to be able to link any structural changes of PSD95 directly to the activation of NMDA receptors. The same time points were used for the control and the condition supplement with APV.

For analysis, spines were separated into two distinct groups. The spines that underwent a persistent enlargement of ≥15% at 60min and 120min after LTP induction were considered potentiated spines. All other spine heads, i.e. <15% enlargement, were called unpotentiated. The 15% level was chosen as it corresponds to one standard deviation of the spine head during baseline (see Appendix figure A.1.D). On average, 40% of the spine heads showed a persistent enlargement of at least 15% at 60min and 120min following LTP stimulation (111 of 279 spines in 19 cells). In some experiments the number of potentiated spines was very low and thus the dendrite was not responsive. Dendrites with enlargement in less than 20% of the spines were therefore discarded. A potentiated and unpotentiated spine over a time course of 120min following LTP induction is represented in Figure 3.2.B. In this example, the area of the spine head increased at 30, 60, and 120 minutes after LTP for the potentiated spine, but not for the unpotentiated one. A quantitative area analysis of the whole measurement series showed a fast and significant enlargement of potentiated spine heads compared to control and unpotentiated spines (figure 3.2.C). After 5min of LTP induction, the spine heads already showed an increase of 37 ± 5% in area when compared to controls. This enlargement increased up to 60 ± 5% after 60min and 52 ± 4% after 120min. While unpotentiated spine heads displayed only a small but significant increase of 10 ± 3% during LTP stimulation compared to control, an increase that was not sustained for the rest of the time course. The same result was obtained when unpotentiated spines were compared to the control condition supplement with APV (Figure 3.2. C). There were no significant changes over the time course in the

control and APV conditions. Thus, these results are consistent with the current literature where LTP induces a rapid enlargement of the spine head.

I also analyzed the area of PSD95 assemblies on potentiated, unpotentiated, and controls spines as described in Section 3.1.1. The area analysis of PSD95 assemblies showed a significant increase of 27 ± 5% only at 60min after LTP induction for potentiated spines in comparison to control while no change was observed in unpotentiated spines or spines incubated in APV (Figure 3.2.D). In the potentiated spines, PSD95 also showed an increase of 15 ± 6% at 30min and 120min after the stimulation, but those augmentations were not significant. However, comparison of potentiated spines with unpotentiated spines presented a significant increase of PSD95 area at 60 and 120min after LTP induction (Figure 3.2.D) This can be observed in the STED picture in Figure 3.2.B where ellipse fit size around PSD95 was increased, especially at 60min after LTP induction for potentiated spines. This area increase was coordinated with a reorganization of PSD95 nanostructure, while unpotentiated spines had practically unchanged PSD95 area and nanostructure over the same time course. These results concord well with a finding of Meyer et al., where PSD95 area increased with a delay of ~ 1h after LTP induction (Meyer et al., 2014). The graphs of figure 3.2.C and D have been normalized to the control condition to avoid any bleaching artefact affecting the PSD95 area. For comparison, the same graphs without normalization are presented in Appendix figure A2.A-B, where the area of PSD95, at the time point 60min, displayed a decrease of 16 ± 3% for control, 10 ± 3% for unpotentiated spines and 11 ± 3% when supplemented with APV. In contrast, PSD95 area in potentiated spine increased significantly at 10 ± 5% (Appendix figure A2.B). The expansion of PSD95 in potentiated spines at 60 minutes after LTP can also be observed in the histogram of PSD95 area (Figure 3.2.F). As such, the area distribution of potentiated spines is shifted to the right towards larger values, compared to control (Figure 3.2.F). Also, the PSD95 area average of 0.189 ± 0.032µm² in the potentiated spines was higher than in the control spines 0.147 ± 0.013µm². The cumulative frequency of PSD95 area also showed a significant difference between the control and potentiated conditions (Figure 3.2.F).

Finally, to confirm the insertion of single glutamatergic receptors following chemical LTP, whole-cell voltage clamp recordings were performed on hippocampal neurons in

collaboration with Dr. ChungKu Lee (Laboratory of Prof. Dr. Rhee). CA1 pyramidal neuron mEPSCs were recorded in organotypic hippocampal slices for 1h after chemical LTP. The hippocampal slice was first submerged in ACSF until a stable baseline was recorded, followed by 10 minutes of incubation with the chemical LTP cocktail and then remained in ACSF for 1 more hour. A significant increase of the average mEPSC amplitude up to 1h after LTP stimulation was observed. For instance, mEPSC amplitude is 1.23 ± 0.06 at 65min after chemical LTP stimulation. For comparison, the control condition showed normalized mEPSCs amplitudes of 0.93 ± 0.04 fold of the baseline at the same time point. This suggests that there were more AMPA receptors at the synapse after the chemical stimulus and confirms our LTP protocol.

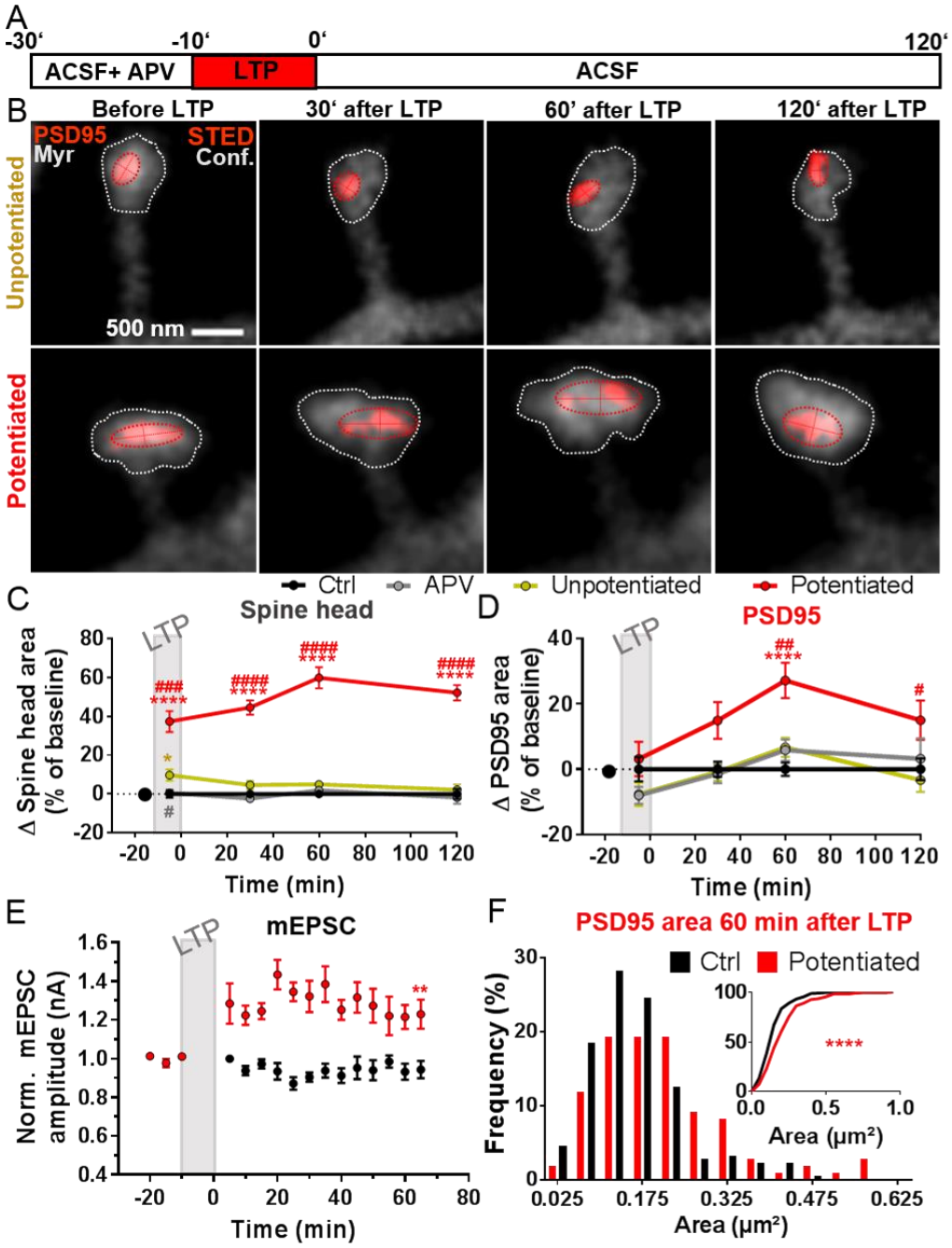

Figure 3.2 Activity-driven plasticity induced a rapid spine head enlargement and delayed PSD95 expansion (A) Time-line of the experiment. LTP is induced by 0Mg^{2+}/ 200µM Glycine/ 20µM Bicuculline **(B)** Images of potentiated and unpotentiated spines co-expressing PSD95-FingR-citrine (STED image) and Myr-rsEGFP2 (confocal image) before and after chemical LTP stimulation. Imaging parameters are listed in the table A1 **(C)** Mean changes in spine head areas of potentiated, unpotentiated spines, and control conditions supplemented with APV following chemical LTP. Changes were normalized to control and compared to control (*) and unpotentiated (#) conditions. *K-W test* with *Dunn's* post hoc showed significant difference: -5min *p= 0.029 and -5-120min ****p< 0.0001 and -5min #p= 0.024, -5min ###p= 0.0004 and 30-120min ####p< 0.0001. **(D)** Same as in (C), but for PSD95 area using fit ellipse. Significant differences shown using *K-W test* and *Dunn's* post hoc: 60min ****p< 0.0001; 60min ## p= 0.0012 and 120min # p= 0.047 **(E)** mEPSC amplitudes recorded in neurons of CA1 region of hippocampal organotypic slice following chemical LTP (in red, n=9) and without stimulation (in black, n=5). *M-W test* was performed at 65 min: **p= 0.007. Dr. ChungKu Lee from the laboratory of Prof. Dr. Rhee performed the experiments. **(F)** Distribution of PSD95 area for potentiated and control conditions at 60min after LTP induction and cumulative distribution of the same data. *K-S test* showed significant difference ****p< 0.0001. (C), (D) and (E) Data are represented as mean +/- SEM and the exact number of experiments and spines are listed in the table A2.

3.1.3 Structural LTP is triggered in small spine heads

The induction of chemical LTP caused the spine population to divide into two classes: potentiated and unpotentiated spines. We then wanted to investigate whether structural LTP depends on spine size, therefore we analysed the spine area before stimulation and 60min after LTP for potentiated and unpotentiated spines (Figure 3.3.A-B). Figure 3.3.C shows that the population of potentiated spines before LTP possessed an average area of 0.45 ± 0.05µm², which is significantly smaller than the area of unpotentiated spines of 0.57 ± 0.04µm² before LTP (Figure 3.3.C). At 60min following chemical LTP, the potentiated spine areas increased significantly to 0.67 ± 0.05µm² compared to their initial area of 0.45 ± 0.05µm², while the unpotentiated spines decreased slightly to 0.54 ± 0.05µm². This tendency is also observed in the Figure 3.3.A-B, where the spine head in the time point before LTP induction is larger for an unpotentiated spine compared to a potentiated spine. In the same example, the spine head area of potentiated spines shows a great enlargement at 60min after LTP compared to before LTP, while the spine head area of unpotentiated spines is reduced at 60min following the stimulation (Figure 3.3 A-B).

It is well known that spine head and PSD size are correlated (Harris & Stevens, 1989). But is this correlation conserved during structural changes induced by LTP? Figure 3.3.D shows the ratio of PSD95 area to the spine head area before LTP and 60min after LTP. LTP induction generated a strong and significant decrease of the original PSD95/spine head area ratio of potentiated spines from 0.42 ± 0.03 to 0.30 ± 0.02 (Figure 3.3D). For unpotentiated spines, we observed a small but significant difference in the ratio (0.37 ± 0.03 vs 0.34 ± 0.02). Thus, the decrease of PSD95/ spine head area ratio is than 4 times higher in the case of potentiated spines compare to unpotentiated spines. This is due to the huge increase of the spine head in potentiated spines of 60%, which is ~2 times larger than the expansion of PSD95 area of 27% at 1h after stimulation. This change is also observed in the Figure 3.3.B, where the ratio of PSD95/spine head area of potentiated spines decreased at 60min after LTP in comparison to before LTP due to the huge growth of the spine head area. Note that the enlargement of the spine head in the example is accompanied by PSD95 expansion and structural modification at 60min following LTP compared to before LTP (Figure 3.3.B). This is supported by a previous finding the fast enlargement of the spine head area immediately after LTP induction disrupted the PSD95/spine head size ratio

(Meyer et al., 2014). This study also demonstrated that 2h after LTP induction, the ratio is restored by the late expansion of PSD95 (Meyer et al., 2014).

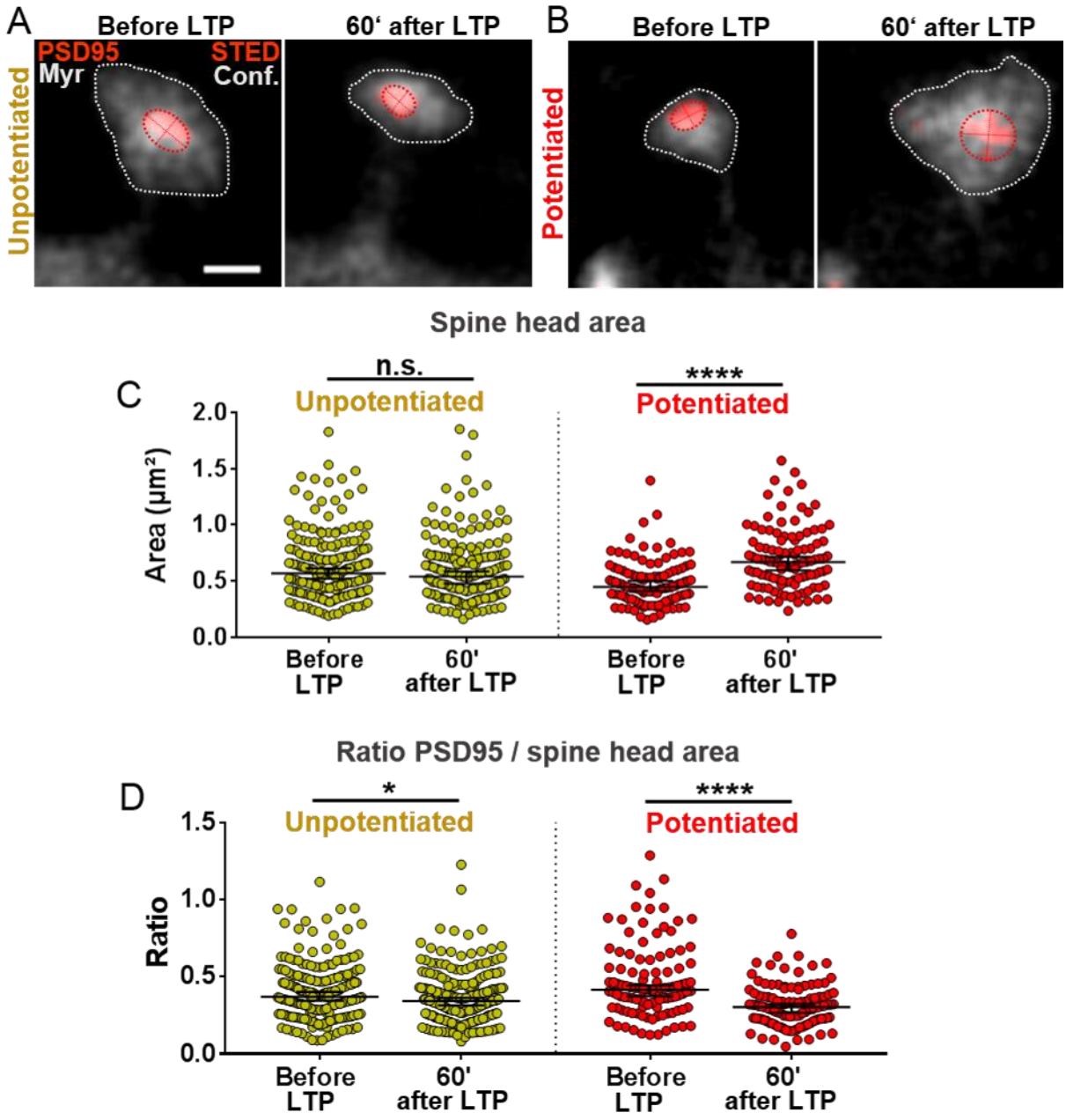

Figure 3.3 LTP promotes the structural plasticity of small spine heads. (A) Image of unpotentiated spines coexpressing PSD95-FinGR-Citrine (STED image) and Myr-rsEGFP2 (confocal image) before and 60min after chemical LTP stimulation. **(B)** Same as (A), but for a potentiated spine. Scale bar: 500nm. Imaging parameters are listed in the table A1. **(C)** Spine head area of unpotentiated and potentiated spines before and 60min after LTP. Significant differences shown with *M-W test*: ****p<0.0001. **(D)** Ratio PSD95 to spine head area of unpotentiated and potentiated spines before and 60min after LTP. Significant differences shown with *M-W test*: *p=0.028 and ****p<0.0001. Data are presented as median ± 95% C.I. and the exact number of experiments and spines are listed in the table A2.

3.1.4 Molecular dynamics of spine head enlargement and PSD95 expansion are ruled by different mechanisms

To better understand the structural changes after LTP, we plotted the area changes as function of their original area (Figure 3.4). Thus, the absolute changes in spine head area between 60min after LTP and before LTP were calculated and plotted as a function of the spine head area before LTP (Figure 3.4.A). Potentiated spines were larger following LTP as evidence by almost all values for potentiated spines being above those of unpotentiated spines or control and above zero. The area of control and unpotentiated spines were essentially unchanged. However, the regression line is slightly below zero indicative of a small shrinkage that could be due to bleaching. The regression line with a negative slope for unpotentiated spines does not show any difference compared to the control (figure 3.4.A). The regression line of potentiated spines shows a positive slope, which is significantly different from the slopes of control and unpotentiated spines (Figure 3.4.A). In other words, we observed that small potentiated spine heads undergo small area changes while larger potentiated spine head heads undergo stronger changes. Such size dependent changes are typically described for multiplicative dynamics. Indeed, a recent model of synaptic changes was done using a Kesten process model. The Kesten process models size fluctuations by $\mu\ (x_t) = < \epsilon - 1 > x_t + < \eta >$. Thus it assumes that initial size x_t changes by both a multiplicative term $< \epsilon - 1 >$ and an additive term $< \eta >$; ϵ and η are stochastic variables (Hazan & Ziv, 2020; Statman, Kaufman, Minerbi, Ziv, & Brenner, 2014; Ziv & Brenner, 2018). Figure 3.4.A thus indicates a large portion of multiplicative changes.

Next, we asked whether changes in PSD95 area are regulated by a similar mechanism as the spine head. As for the spine head, the absolute area of PSD95 changes between 60min after LTP and before LTP have been plotted as a function of the initial area of PSD95. Then, a linear regression line was plotted (Figure 3.4.B). In the case of PSD95, the slope for control, unpotentiated, and potentiated conditions were all similar and did not show any differences (potentiated= -0.288 vs unpotentiated= -0.298 vs control= -0.315). This indicates that PSD95 dynamics are not controlled by a multiplicative component as for the spine head. Nevertheless, the changes of potentiated spines are larger than for control and unpotentiated spines since most of the points are above the regression line of the control condition. Moreover, the regression line of potentiated spines is shifted to larger (positive) changes. This shift is significantly different when

comparing the Y-intercept of potentiated (0.061), unpotentiated (0.030) and control (0.009) conditions. This offset in Y for potentiated spines, which is strongly different compared to control and unpotentiated spines, suggests that PSD95 size dynamics were regulated by an additive component (Figure 3.4.B). In other words, small PSD95 assemblies as well as large PSD95 assemblies of potentiated spines increased in average by the same area when compared to control. Also, the mean area of PSD95 assemblies, which corresponds to the point where the linear regression crosses the X-abscissa, was larger in potentiated spines with a value of 0.210μm² while for the control condition the mean area of PSD95 assemblies is 0.030μm² and 0.101μm² for unpotentiated spines. Therefore, potentiated spines present a greater growth factor and larger mean area of PSD95 assemblies.

The graph of PSD95 dynamics also provided information about the population of PSD95 assemblies that undergo area increases after LTP induction. PSD95 assemblies that were larger than ~0.3 μm² showed mostly negative changes in potentiated spines, indicating that large PSD95 assemblies preferentially decreased at 60min after LTP (figure 3.4.B). Moreover, smaller PSD95 nanoorganizations were associated with a growth of PSD95 assemblies, especially those with an area less than ~0.3μm² in potentiated spines. Thus, after LTP induction, the negative slope of the linear regression suggested that small PSD95 assemblies had a tendency to become larger, while the large PSD95 assemblies had a tendency to shrink. However, small and large PSD95 assemblies in potentiated spine increase by the same factor (additive growth) when compared to control. These results suggest that small PSD95 assemblies in potentiated spines increased more than small PSD95 assemblies in the control condition. Similarly, with the same factor, larger PSD95 assemblies of potentiated spines decreased less than larger PSD95 assemblies in the control condition. The area decrease could also be induced by the small bleaching effect of PSD95 as present in Appendix figure A1.E. In summary, we observed that change in spine heads might be regulated by a multiplicative component and PSD95 by an additive component. Therefore, LTP driven changes of spine head and PSD95 follow different mechanisms.

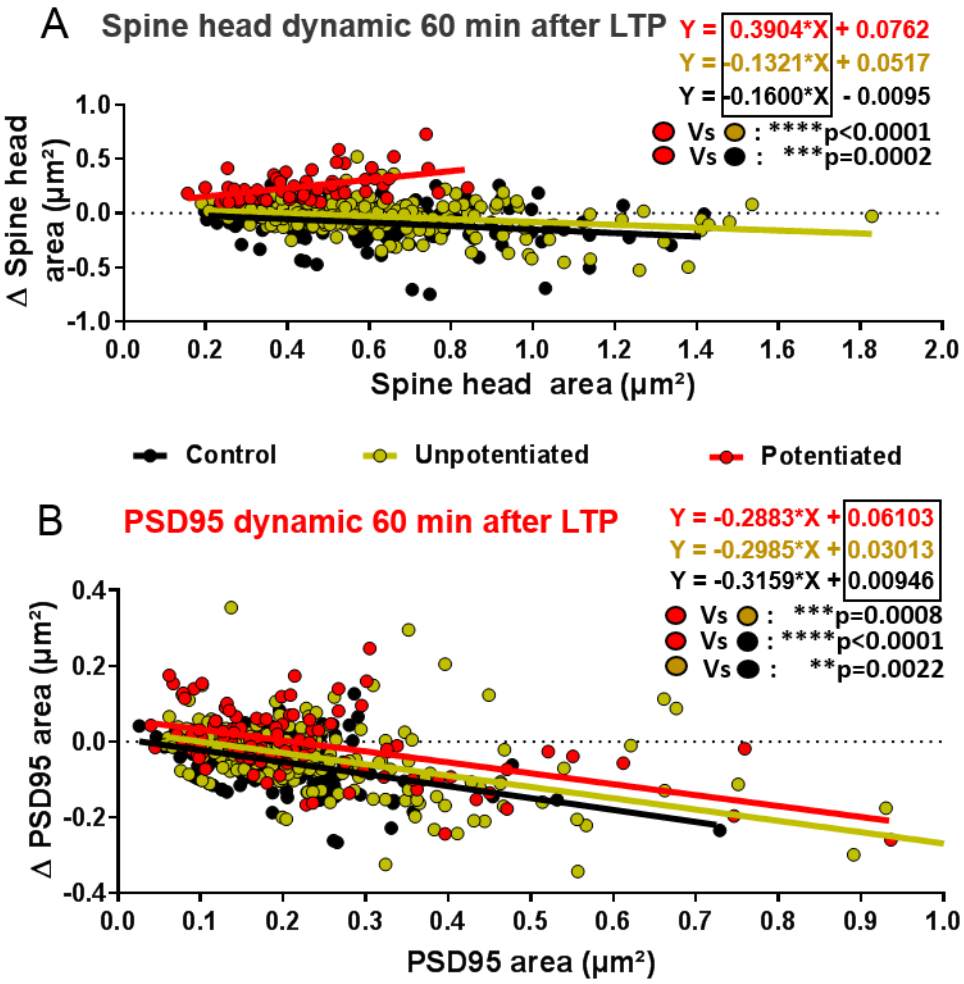

Figure 3.4 Spine head and PSD95 size dynamics are driven by different mechanisms. (A) The absolute value of spine head area changes at 60 min after LTP in potentiated, unpotentiated, and control conditions was plotted against the initial spine head area before LTP. A significant difference between slopes was found using ANCOVA. **(B)** Same as (A), but for PSD95 area changes. The slope was similar, but a significant difference between the Y-intercept of the linear regression was found using ANCOVA. The exact number of experiments and spines are listed in the table A2.

3.1.5 Morphological changes of PSD95 during activity-driven plasticity

In the previous chapter I showed that the area of PSD95 expands at 1h after LTP induction. The next question was to investigate whether the PSD95 area increases were accompanied by morphological changes of the protein assembly. Therefore, I set out to categorize PSD95 into different morphology classes. PSD95 is the most abundant protein of the PSD and PSD95 nanoorganization as observed by STED revealed similar structure to that of the PSD. Thus, I categorized the PSD95 nanoarchitecture with the same terms as the PSD structure: macular, perforated, segmented 2, and segmented 3. Examples of each categorization are displayed in

Figure 3.5.A. Spines containing a disk-like shape of PSD95 assemblies were defined as macular, spines containing a U-shape or ring-like structure of PSD95 assemblies were defined as perforated, spines containing two clusters of PSD95 were defined as segmented 2, and spines containing three clusters as segmented 3. The area of the spine head is about 2 times larger when they hold a perforated PSD95 (average spine head area: 0.86 ± 0.09μm²) and ~1.5 times larger with segmented 2 PSD95 (average spine head area: 0.73 ± 0.05μm²) compared to spines containing a macular one (average spine head area: 0.46 ± 0.03μm²) (Appendix Figure A3.A). Similarly, the area of perforated PSD95 is also 2 times larger than macular PSD95 (P: 0.36 ± 0.09μm² vs M: 0.18 ± 0.01μm²) and segmented 2 PSD95 is 1.5 times larger than macular (S2: 0.26 ± 0.04μm² vs M: 0.18 ± 0.01μm²) (Appendix Figure A3.B). Therefore, perforated and segmented PSD95 assemblies displayed larger PSD95 assemblies that appear only on large spines.

Next, the morphology of PSD95 in potentiated spines and without stimulation was investigated during the LTP time course explained in section 1.3.2. In the control condition, the proportion of the different shapes was mainly conserved over the time course. There were 93% of macular PSD95 at the initial time point, 90% at 60min, and 91% at 120min. Similarly, the proportion of perforated and segmented PSD95 was constant in the control condition. However, in the case of potentiated spines, the macular proportion of 91% before LTP decreased to 86% at 30min, 78% at 60min, and down to 70% at 120min after stimulation (Figure 3.5.B). This reduction of macular configurations was accompanied by an increase of segmented 2 and perforated PSD95 (figure3.5.B). For instance, the number of segmented 2 before LTP was 7% and increased up to 12% at 30min, 16% at 60min and up to 20% at 120min The quantity of perforated PSD95 is only 2% before LTP and increased to 4% after 60min and 8% at 120 min after stimulation (Figure 3.5.B). Thus, PSD95 remodeling is induced by the LTP protocol and thus driven by NMDA receptor mediated activity. Macular PSD95 is mainly transformed into segmented 2 with a linear increase of segmented 2 over the time course of 120min after LTP stimulation. At 120min following LTP induction, an increase of perforated PSD95 was also detected.

Furthermore, to support the qualitative analysis of PSD95 morphology in Figure 3.5.B., the filling ratio was calculated for every PSD95 with the formula: ∑ Pixel area/ area fit

ellipse, where the sum of the pixel area, ∑, was calculated as: (number of pixels x pixel size) and the area of the fit ellipse as described in section 3.1.1. The number of black pixels in the area of the ellipse around PSD95 nanoorganization gave access to the filling ratio. An example of filling ratio for different PSD95 morphologies is presented in Figure 3.5.C. In this example, the perforation of PSD95 reduced the filling ratio to 0.77, and an even larger decrease was observed in the segmented PSD95. The filling ratio was 0.802 ± 0.007 for macular PSD95, decreased to 0.685 ± 0.013 for perforated, to 0.595 ± 0.009 for segmented 2 and to 0.507 ± 0.025 for segmented 3 PSD95 (Appendix figure A3.C). I used the filling ratio to quantify the morphological changes of PSD95 in the time course after LTP induction. In the control condition, the filling ratio was essentially constant during the whole time course with a value of 0.781 ± 0.007 before LTP, 0.763 ± 0.008 at 60min and 0.767 ± 0.013 at 120min after LTP. The potentiated spines presented a significant decrease from 0.804 ± 0.012 to 0.729 ± 0.013 at 60 min and to 0.705 ± 0.015 at 120min after LTP. Thus, this data supports the idea that the size expansion of PSD95 at 60min after LTP is accompanied by the remodeling of the PSD95 organization.

3.1.6 Large PSD95 undergo further remodeling during plasticity

In the preceding sections, we showed that PSD95 underwent expansion and morphological changes following LTP. The next question was to determine whether the remodeling of PSD95 assemblies were specific to the population of small PSD95 or the large one. To investigate the morphology of small and large PSD95, the population of PSD95 was divided into two groups before LTP stimulation: PSD95 smaller than 0.200µm² and PSD95 larger than 0.200µm². As presented in the last section, the area of macular PSD95 is on average 0.18 µm², while perforated PSD95 is 0.36µm² and segmented 2 is 0.26µm² (Appendix Figure A3.B). Thereby, the group of PSD95 smaller than 0.200µm² should be mostly composed of macular PSD95.

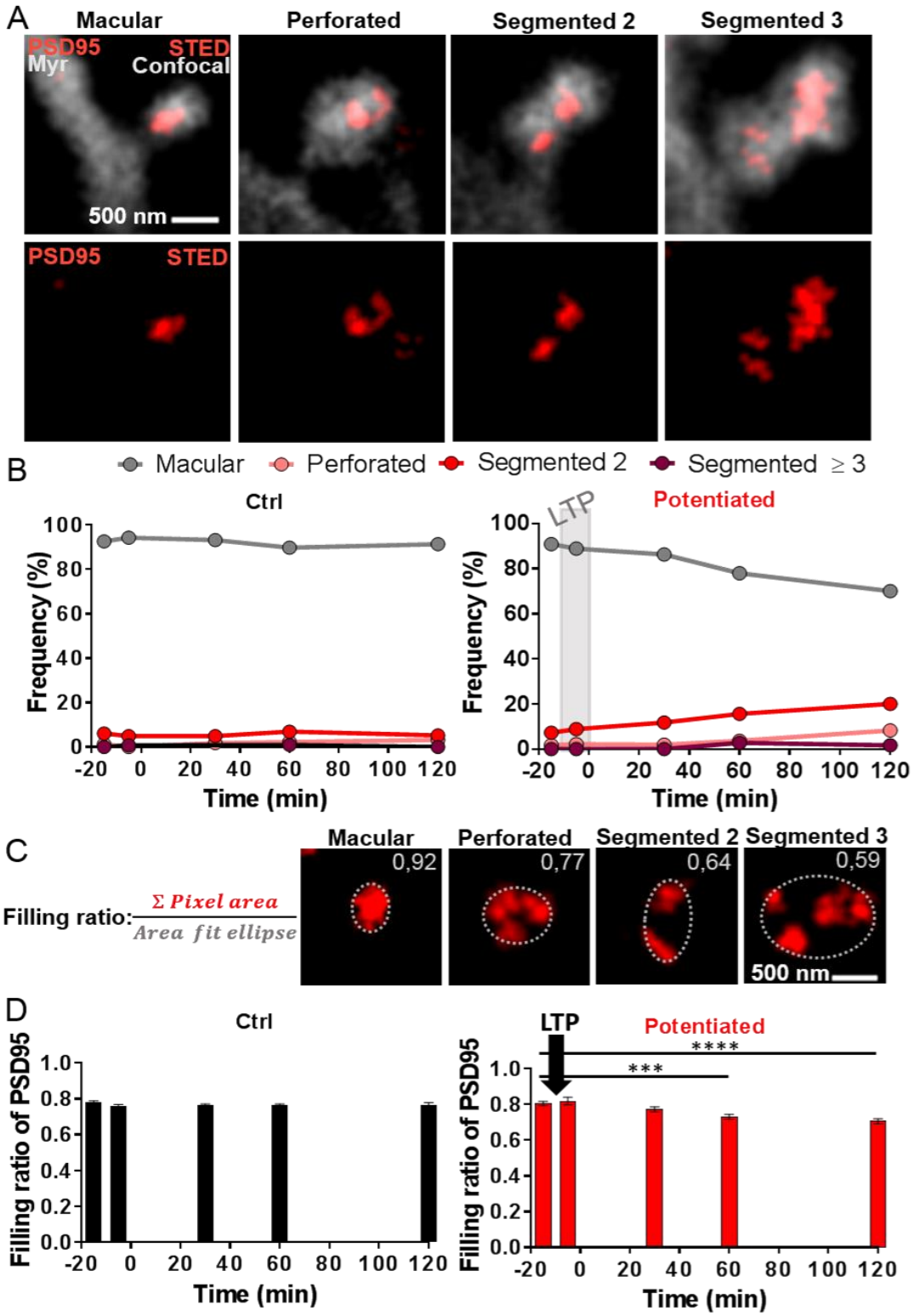

Figure 3.5 Reorganization of PSD95 nanostructure during plasticity. (A) Images of macular, perforated, segmented 2, and segmented 3 PSD95 revealed by PSD95-FingR-Citrine expression (STED image) and the spine head with Myr-rsEGFP2 (confocal image). **(B)** Frequency of macular, perforated, segmented 2, and segmented ≥ 3 PSD95 over 120min time course after LTP stimulation. **(C)** An example of the filling ratio for macular, perforated, segmented 2, and segmented ≥ 3 PSD95. **(D)** The filling ratio of PSD95 for control and potentiated spines condition over a 120min time course after LTP stimulation. Same data set as Figure 3.2.D. A significant difference is shown using one-way ANOVA and Dunnett's post hoc: ***p=0.0002 and ****p<0.0001. Data are represented as mean +/- SEM. The exact number of experiments and spines are listed in the table A2.

The morphology of small PSD95 < 0.200µm² was analyzed on potentiated spines after LTP induction. Representative pictures of potentiated spine containing small PSD95 before LTP induction and over a time course after LTP stimulation are shown in Figure 3.6.A. As expected, 97% of the spines before stimulation contained macular PSD95 and only 3% have a segmented 2 (Figure 3.6.B). At 1h after LTP induction, the proportion of segmented 2 PSD95 increased to 15% while the percentage of macular decreased to 82%. After 2h, the level of macular PSD95 stayed stable at 82%, the frequency of segmented decreased slightly to 12% while the number of perforated increased to 6%. Thus, most of the changes observed for the small PSD95 came from remodeling of macular PSD95 into segmented 2 (Figure 3.6.B). The STED images of potentiated spines over the time course of LTP also displayed this tendency of macular to become segmented 2 in the top and bottom images of Figure 3.6.A. For example, in the top image, the changes occur at 1h, and in the bottom time course macular PSD95 became segmented 2 at 30min, were macular after 60min and segmented 2 again after 120min after LTP. The time course presented in the middle of Figure 3.6.A, showed an example of macular PSD95 that became perforated 2h after LTP.

On the other hand, large structures of PSD95 were also investigated on potentiated spines during activity-driven plasticity. Spines containing large PSD95 ≥ 0,200 µm² before LTP are shown over the same time course in Figure 3.6.C. Before LTP, 83% of the spines possessed a macular, 13% segmented 2, and 4% perforated PSD95. At 60min following the stimulation, macular decreased to 72%, while segmented 2 increased to 17%, perforated to 7%, and segmented 3 appeared at 4%. Even more remodeling happens 120min after LTP stimulation, the level of macular PSD95 decreased to 55% while segmented 2 rose to 30% and perforated to 15% (Figure 3.6.D). To highlight this tendency, the STED pictures of large PSD95 assemblies over the times courses after LTP induction also display a higher level of perforated and segmented PSD95 than the small PSD95 (figure 3.6.C). For example, the top time course of figure 3.6.C exhibited a macular PSD95 that becomes segmented 2 at 60min and perforated at 120min following LTP stimulation. The time course in the middle also shows a macular PSD95 that became segmented 2, but this time at 120min after LTP (Figure 3.6.C). The bottom example displayed a large segmented 2 PSD95 that became segmented 3 at 60min and perforated at 120min after LTP induction (Figure

3.6.C). Therefore, these data suggest that large PSD95 undergo a stronger structural remodeling, especially at 120min after LTP. This is supported by the data showing the population of large PSD95 had about two times more segmented 2 and perforated PSD95 compared to the small PSD95 after 120min.

Furthermore, as mentioned in section 3.1.4, the negative slope of the linear regression suggests that small PSD95 tends to grow and large PSD95 tends to shrink. Therefore, the area change of small and large PSD95 area was also explored during a time course following LTP. In Figure A2.E-F (Appendix) shows that small PSD95 displayed an increase in area of 35 ± 8% 60min after LTP stimulation while the larger PSD95 showed an increase of only 16 ± 5% in comparison to control (Appendix Figure A2 E-F). Therefore, small PSD95 presented an average area increase which is two times higher than large PSD95. On the same line, spine heads of potentiated spines tended to enlarge further when containing a small PSD95 (66 ± 9 %) compared to a large PSD95 (52 ± 4 %) (Appendix Figure A2.C-D). To conclude, the NMDA receptor mediated activity promoted the growth of PSD95 assemblies, especially of the small, macular ones at 60min after LTP induction while structural remodeling is more frequent in large PSD95, notably at 120min after LTP.

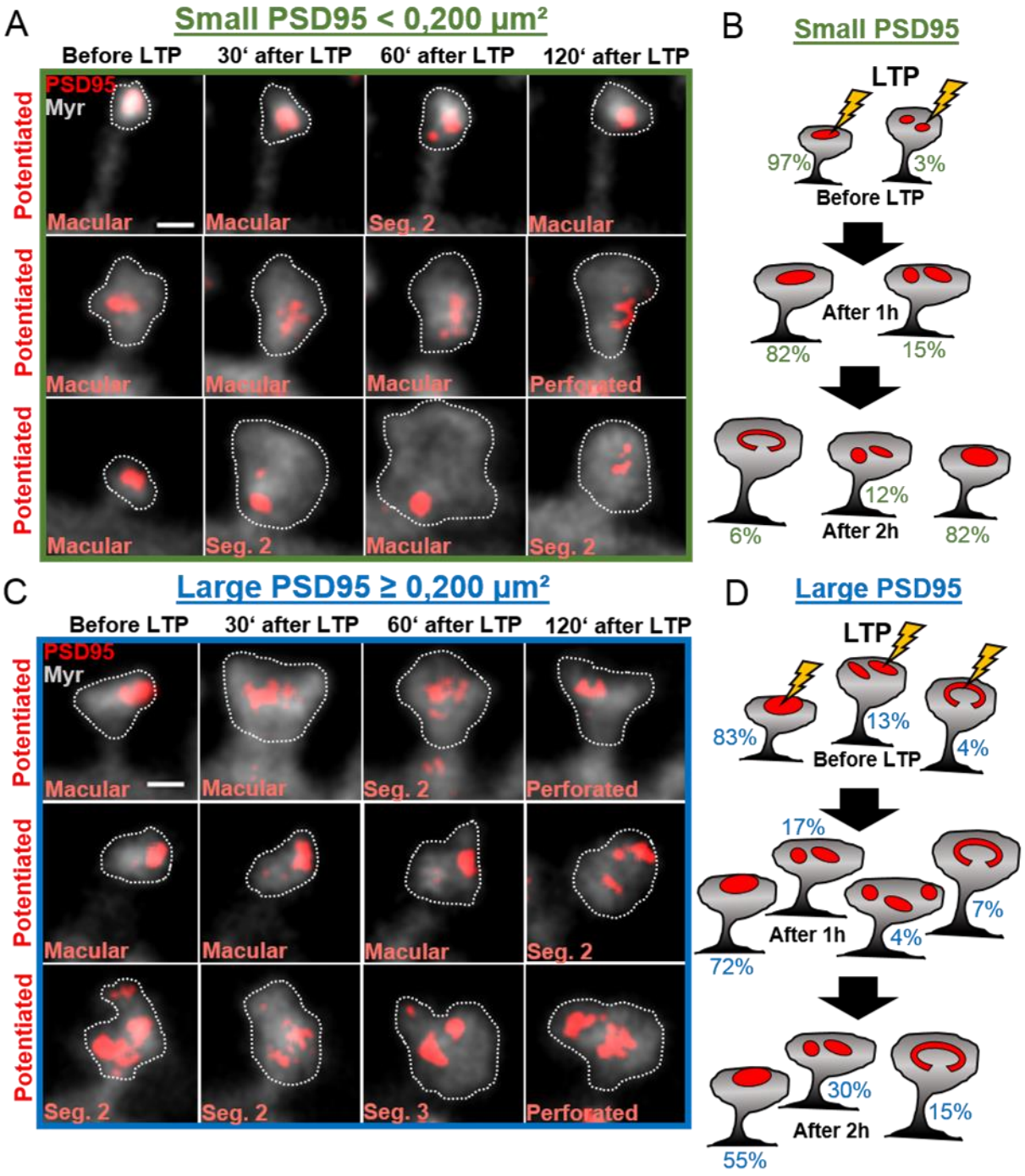

Figure 3.6 Structural remodeling is increased in large PSD95 after LTP induction. (A) Images of potentiated spines with a small PSD95 area initially (< 200 µm²) and its spine head before and after chemical LTP stimulation. PSD95 area is obtained with PSD95-FingR-citrine expression (STED image) and spine head with Myr-rsEGFP2 (confocal image). Imaging parameter are listed in table A1 **(B)**. Cartoon of different PSD95 morphologies after LTP induction of small PSD95 and frequency of appearance **(C)** Same as (A), but for large PSD95 (≥ 200 µm²). **(D)** Same as (B), but for large PSD95. Scale bar: 500 nm. Imaging parameters are listed in the table A1. The frequency of small and large PSD95 morphologies in Figure 3.6.B and D is taken from Appendix Figure A.2.G-H. The exact number of experiments and spines are listed in the table A2.

3.2 Remodeling of PSD95 organization enhance synaptic transmission

In the first part of this thesis, expansion and remodeling of PSD95 following LTP was revealed using live-cell STED imaging. In this section, the impact of such changes on synaptic transmission efficiency was questioned. The amount and area of AMPA receptor nanodomains in correlation to change of PSD95 assemblies was investigated. This was done via immunohistological staining of hippocampal cell cultures that were fixed at different time points after chemical LTP induction. Cells were imaged using two-color STED microscopy. Using the same method, the area and morphology of the active zone protein Bassoon was also imaged and analyzed with respect to changes in PSD95 morphology. An increase in size of Bassoon together with the incorporation and/or enlargement of AMPA receptor clusters during LTP driven PSD95 remodeling would suggest an increase in the synaptic strength. We decided to employ immunohistochemistry for this study since there are no live-cell compatible tags available for endogenous AMPA receptor and Bassoon labeling. As the expression of fusion proteins are often subject to expression artifacts, we chose conventional antibody labeling.

3.2.1 Size distribution of PSD95, AMPA receptor, and Bassoon organization revealed by two-color STED microscopy

To observe the impact of during activity-driven plasticity on the area and number of AMPA receptor nanodomains, which are a correlate for synaptic transmission, as well as the area and morphology of the active zone protein Bassoon, we employed two-color STED imaging and antibody staining. The AMPA receptor nanodomain was targeted by an antibody specific to the GluA2 subunit of the AMPA receptor. Before studying these proteins, the fixation method of hippocampal cell cultures was optimized to improve antibody specificity. The paraformaldehyde fixation was replaced by Glyoxal, which resulted in a better preservation of the cellular architecture (Richter et al., 2018). The pH of the Glyoxal solution was adjusted to optimize specificity of the antibody binding and reduce unspecific labelling. The antibody dilution was also optimized to reduce unspecific binding and adjustment of the brightness of both colors for STED imaging (Figure 2.3.A-C). Furthermore, an antibody against actin filaments (Phalloidin) was implemented to target the spine and dendrite. Phalloidin was imaged in confocal mode in order to obtain three color images composed of the spine head,

PSD95, and AMPA receptor or Bassoon as presented in Figures 3.7.A-B. For this three-colour imaging, I used a STED microscope that was optimized for imaging of two organic dyes instead of fluorescent proteins in the previous sections. Thus, I used secondary antibodies tagged with Alexa594 or STAR RED, both emitting in the red and far-red. For the confocal channel, phalloidin was fused to Alexa488 emitting in the green. For details of spectral separation and cross-talk refer to section 2.method Figure 2.3.A-C.

As can be seen in Figure 3.7.A, AMPA receptor clusters appear on spines and also on dendrites. To study the impact of AMPA receptor organization on synaptic transmission, only AMPA receptor nanodomains located on PSD95 nanoorganizations were analysed. Synaptic AMPA receptor nanodomains trapped by PSD95 are known to modulate the strength of the synapse (Nair et al., 2013; Opazo et al., 2010). For this reason, only synaptic proteins were investigated. Similarly, the morphology and area of Bassoon were measured in rough colocalization with PSD95 nanoorganization. Additionally, only the synaptic PSD95 nanoorganizations located on a spine head were taken into account. The area of all protein assemblies was measured by the summation of pixels as shown in Figure 3.7.C-E. The distribution of the PSD95 area (median: 0.195 ± 0.007μm²) was similar to Bassoon area (median: 0.197 ± 0.009μm²). The AMPA receptor area distribution (median: 0.053 ± 0.007μm²) was smaller than PSD95 and Bassoon (Figure 3.7.C-E).

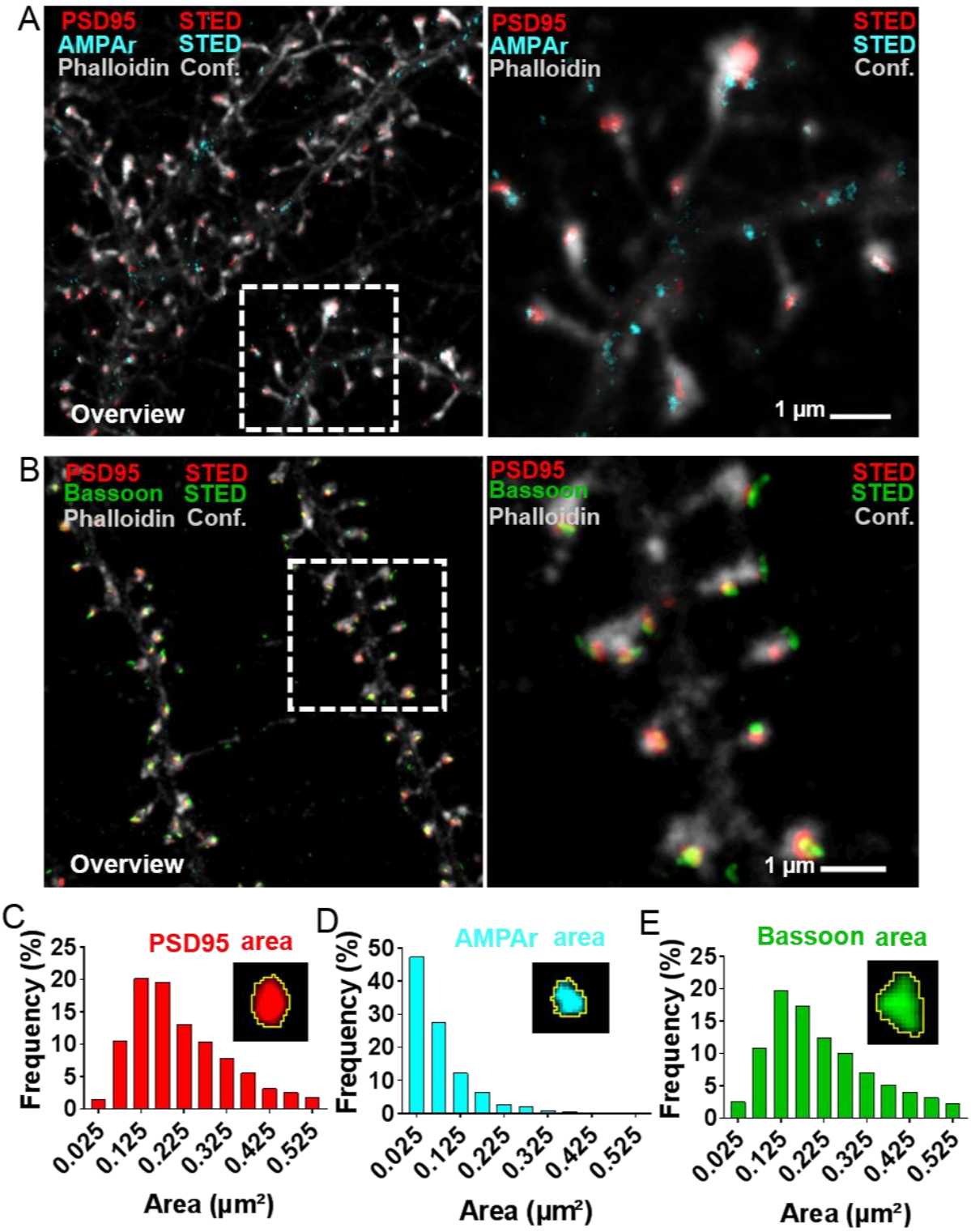

Figure 3.7 Two-color STED microscopy of PSD95, AMPA receptor and Bassoon organizations. **(A)** Two-color STED imaging of PSD95 and AMPA receptors (AMPAr) antibody labeling, and confocal image of actin (phalloidin labelling) using immunohistochemistry in hippocampal neuronal cell culture at 17DIV. **(B)** Two-color STED imaging of PSD95 and Bassoon, and actin (phalloidin) with confocal microscopy of hippocampal neuronal cell culture at 20 DIV. **(C)** Distribution of PSD95 area, n=988. **(D)** Distribution of AMPA receptor area, n=723 and **(E)** distribution of Bassoon area, n=2226. (C-E) The bin size of all 3 distributions is 0.05 µm². Imaging parameters are listed in the table A1.

3.2.2 Simultaneous enlargement of PSD95 assembly and AMPA receptor nanodomain area

To study the plasticity of AMPA receptor nanodomains with PSD95 expansion after activity induced, we used a chemical LTP protocol as described in section 2.4. First, LTP was confirmed in hippocampal neuronal cell cultures by recording mEPSCs. The cell activity was recorded up to 30 minutes after 5min of LTP induction by Dr. Erinn Gideons from the laboratory of Prof. Dr. Nils Brose. The data showed significantly higher mEPSC amplitudes with LTP induction until the end of the experiment (Figure 3.8.C). In this experiment, 3 cells displayed a decrease in amplitude, while 8 cells exhibited an augmentation of mEPSC amplitudes following chemical LTP, suggesting a gain of activity mediated by AMPA receptors (Figure 3.8.C).

For the fluorescence labeling, chemical LTP was induced for 5min. Then the neurons were fixed at the following time points: 0, 30, 60, and 120 minutes. After immunolabeling of PSD95 and AMPA receptors, and labeling of actin with phalloidin, three-color images were taken for each time point (Figure 3.8.A-B). Subsequently, the total area of PSD95 per spine head was analyzed and all PSD95 clusters present in a single spine head were summed. The area of PSD95 and AMPA receptor clusters were calculated by summation of pixels as explained in the previous section 3.2.1. The total area of AMPA receptors was calculated as the summation of all AMPA receptor clusters within the PSD95 organization (Figure 3.8.A-B). We found a significant increase of PSD95 area at 30, 60, and 120 minutes after LTP induction that was accompanied by a significant augmentation of AMPA receptor area at the same time points (Figure 3.8.D, E). Immediately after stimulation (0min), the area of stimulated PSD95 (LTP: 0.193 ± 0.014μm² vs Ctrl: 0.196 ± 0.012μm²) and AMPA receptor compared to control (LTP: 0.056 ± 0.016μm² vs Ctrl: 0.047 ± 0.016μm²) were not significantly changed (Figure 3.8.D, E). At 30min, the total area of PSD95 (LTP: 0.212 ± 0.018μm² vs Ctrl: 0.178 ± 0.015μm²) and AMPA receptor (LTP: 0.079 ± 0.019μm² vs Ctrl: 0.052 ± 0.017μm²) were significantly larger. We also observed an increase at 60min after LTP for which the area of PSD95 was 0.249 ± 0.018μm², which is significantly larger than control 0.168 ± 0.013μm²; at the same time the area of AMPA receptors was 0.098 ± 0.013 μm² and 0.062 ± 0.009μm² for control (Figure 3.8.D, E). Finally, at the 120min time point, the AMPA receptor area increased further (LTP: 0.150 ± 0.029μm² vs Ctrl:

0.080 ± 0.013μm²). The PSD95 area was still significantly larger compared to control (LTP: 0.202 ± 0.026μm² vs Ctrl: 0.177 ± 0.011μm²) (Figure 3.8.D, E).

Furthermore, the cumulative frequency distribution also confirms the area increases of PSD95 and AMPA receptors following LTP stimulation (Figure 3.8.F-G). It should be noted that the STED images of PSD95 and AMPA receptor showed this tendency very clearly (Figure 3.8.A-B). PSD95 area increased in at 30, 60, and 120 minutes after LTP. AMPA receptor nanodomains were also larger, especially at 60 and 120min after LTP. The number of AMPA receptor clusters located on PSD95 organizations also increased at 120min after stimulation (Figures 3.8.A-B). Thus, enlargement of PSD95 assemblies led to an increase in the area of AMPA receptor nanodomains. This could be caused by either the growth of one cluster or appearance of additional clusters.

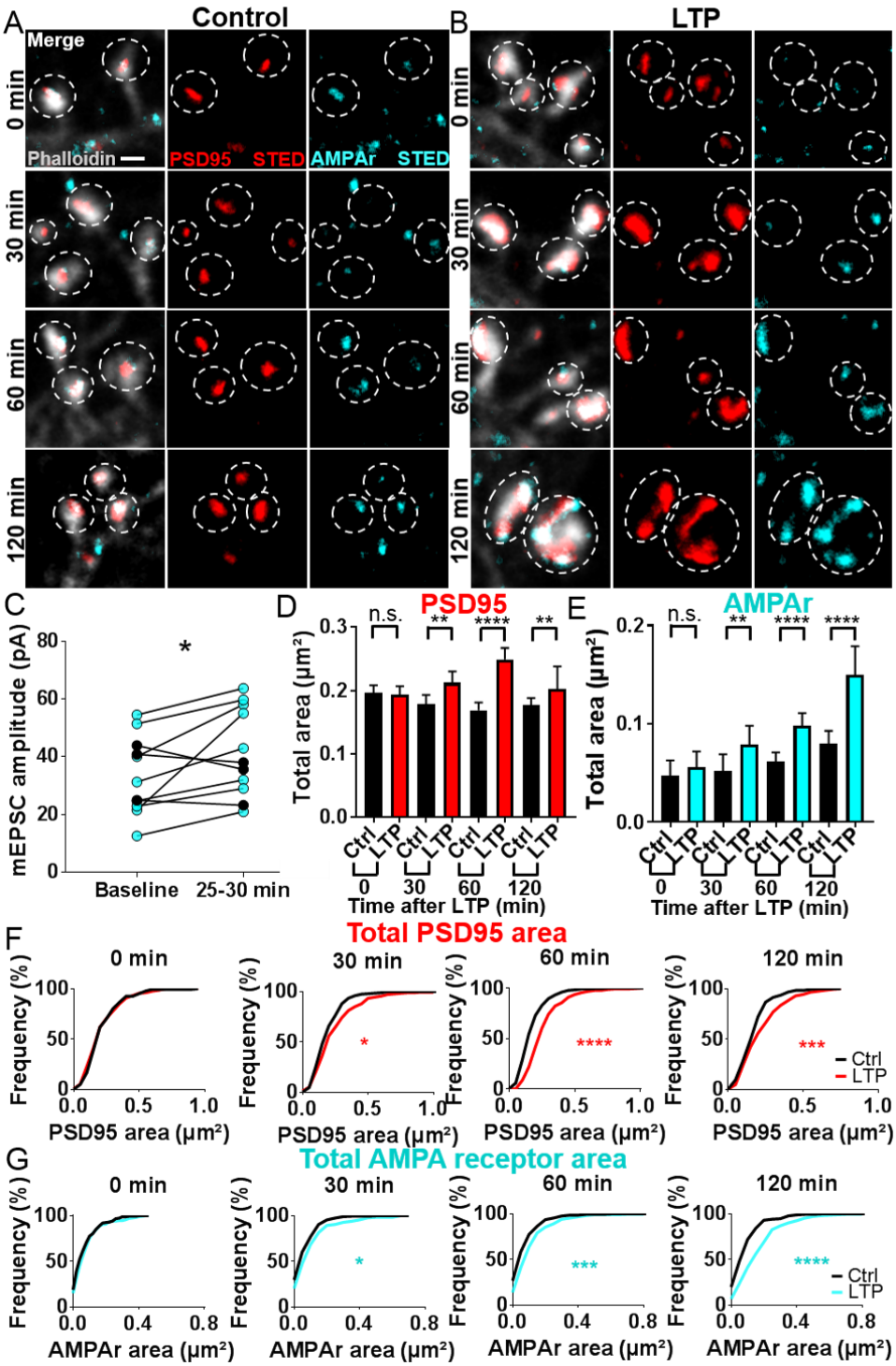

Figure 3.8 Activity-driven plasticity promotes area increase of PSD95 and AMPA receptor nanodomains. (A, B) Two-color STED imaging of PSD95 and AMPA receptors (AMPAr) together, with actin (phalloidin) images with confocal. The image was taken at 0, 30, 60, and 120min after LTP stimulation of hippocampal neuronal cultures (17DIV) (B) or without stimulation (A). Imaging parameters: Table A1. Scale bar: 500nm. **(C)** mEPSCs recorded in hippocampal cell cultures until 30min after LTP induction. Wilcoxon paired t-test showed significant difference between baseline and 25-30 min after stimulation: *p=0.03. Dr. Erinn Gideons performed the experiments **(D)** Total PSD95 area per spine at 0, 30, 60, and 120min following LTP compared to control. Data shown as median +/- 95% C.I. M-W test showed significant difference: 30min **p=0.003, 60min ****p<0.0001 and 120min **p=0.002. **(E)** Same as (D), but for total AMPA receptor clusters per PSD95 organization. 30min **p=0.0018 and 60-120min****p <0.0001. **(F)** The cumulative frequency of the total PSD95 area compared to control at different time points after LTP stimulation. Same data set as (D) K-S test showed significant difference: 30min *p=0.018, 60min ****p <0.0001 and 120min ***p=0.0001. **(G)** Same as (F), but for total AMPA receptor clusters. Same data set as (E). 30min *p=0.0238, 60min ***p=0.0002 and 120min ****p <0.0001. The exact number of experiments and spines: Table A2.

3.2.3 LTP promotes enlargement and appearance of additional AMPA receptor clusters

The next question was to determine whether the observed increase in total AMPA receptor area was caused by the enlargement of a single AMPA receptor cluster or the appearance of new AMPA receptor clusters. The area of the individual AMPA receptor nanoclusters was analyzed in stimulated and unstimulated spines in hippocampal neuron cultures. Figure 3.9.B shows a significant increase in area of single AMPA receptor clusters at 30, 60, and 120min after LTP. No difference was detected at 0 min between stimulated neurons and control (LTP: 0.044 ± 0.008 μm² vs Ctrl: 0.044 ± 0.015 μm²), while at 30min the area of individual clusters enlarged significantly (LTP: 0.064 ± 0.012 μm² vs Ctrl: 0.046 ± 0.012 μm²) and even more at 60min (LTP: 0.073 ± 0.011 μm² vs Ctrl: 0.060 ± 0.007 μm²) and 120min (LTP: 0.096 ± 0.018 μm² vs Ctrl: 0.063 ± 0.010 μm²) (Figure 3.9.B). Furthermore, the cumulative area distribution displayed a significant enlargement of single AMPA receptor nanodomains at 60 and 120min after LTP (Figure 3.9.C).

Thereafter, we investigated the number of AMPA receptor clusters per PSD95 organization after LTP induction. An augmentation in the average number of AMPA receptor nanodomains in stimulated neurons compared to unstimulated at 0min (LTP: 1.37 ± 0.06 vs Ctrl: 1.20 ± 0.05) was observed (Figure 3.9A). A further increase of AMPA receptor nanodomain number was observed at 120min (LTP: 1.51 ± 0.05 vs Ctrl: 1.22 ± 0.05). Nonetheless, no significance was found at 30min (LTP: 1.32 ± 0.06 vs Ctrl: 1.20 ± 0.05) or at 60min (1.32 ± 0.05 vs 1.18 ± 0.04) after LTP stimulation. However, the average number of AMPA receptor clusters was slightly higher for all time-points in stimulated spines compared to control (Figure 3.9.A). Moreover, we calculated the percentage of PSD95 organizations without AMPA receptor clusters at every time point (Figure 3.9.D). Without AMPA receptors the synapse cannot be activated and thus is called a silent synapse. Immediately following the stimulation (0min), the frequency of synapses without AMPA receptor nanodomains, silent synapses, was similar in stimulated (8.2 %) and control spines (9.6%) (Figure 3.9.D). At 30min after LTP, the proportion of silent synapses decreased and became ~2 times less than in control (LTP: 6.6% vs Ctrl: 12.6%), at 60min 3 times less (LTP: 2.7% vs Ctrl: 8.1%) and finally at 120min after LTP, ~5 times less synapses without AMPA receptors were present compared to control (LTP: 1.4% vs Ctrl: 6.9%) (Figure 3.9.D).

An example of two silent synapses is shown 30min after LTP induction in Figure 3.8.A. In this image, two macular PSD95s were not occupied by an AMPA receptor cluster. Therefore, LTP promoted the gradual insertion of new AMPA receptors on silent synapses, especially at 2h after LTP when silent synapses vanished. At the same time, the average number of AMPA receptor nanodomains per PSD95 organization, as well as the AMPA receptor cluster area, was significantly higher.

In summary, LTP induces the enlargement of a single AMPA receptor cluster and the appearance of a new AMPA receptor cluster on PSD95 nanorganizations. This increase is also conserved in the correlation between PSD95 and AMPA receptor area during structural LTP. Figure 3.9.E shows the PSD95 area as function of AMPA receptor area after LTP stimulation. The slope between control and LTP does not show any difference (Figure 3.9.E). This indicates that the LTP induced enlargement of the AMPA receptor area goes hand in hand with the area increase of PSD95.

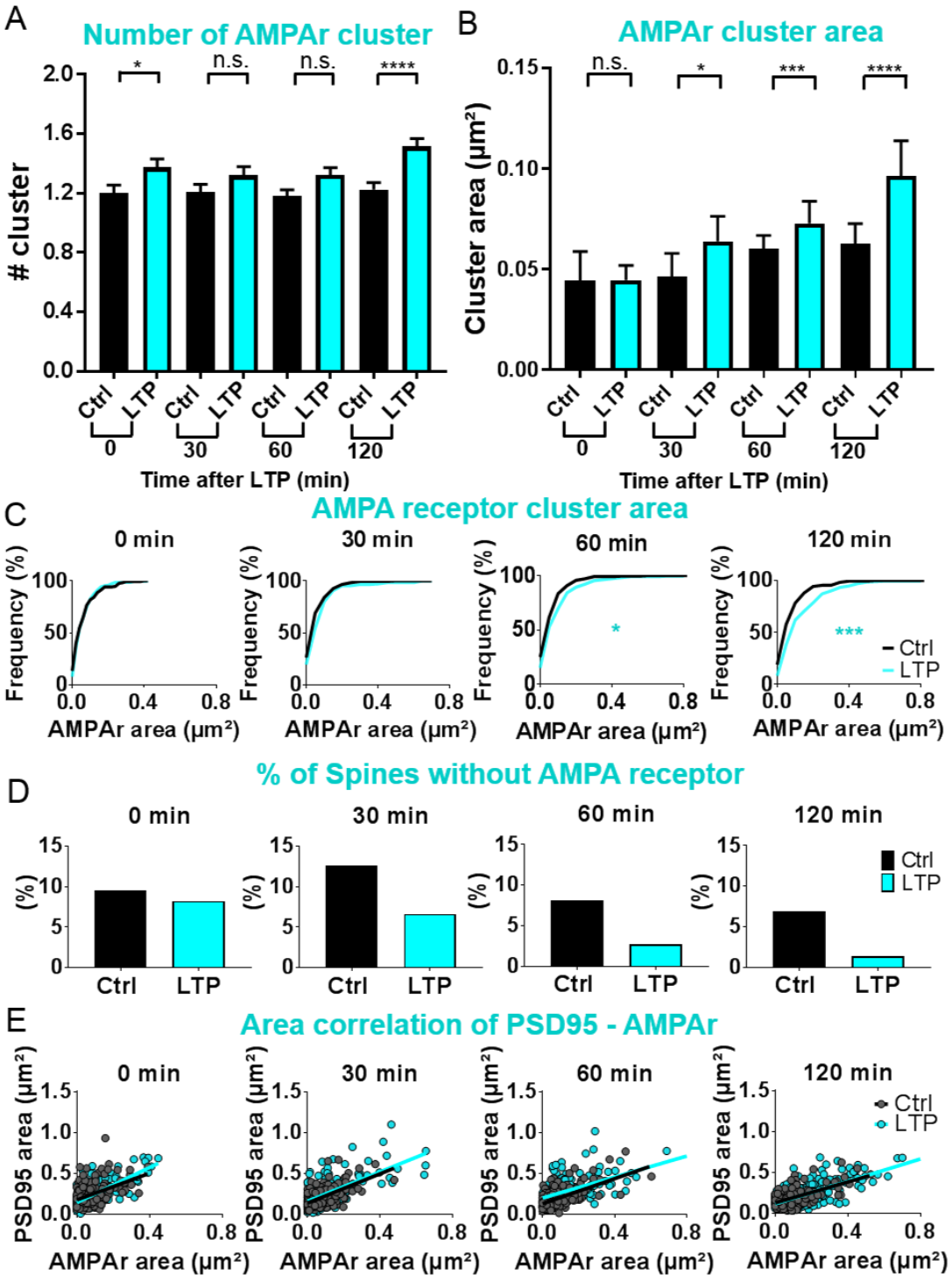

Figure 3.9 Number and area of single AMPA receptor clusters increased after LTP. (A) The number of AMPA receptor (AMPAr) clusters per PSD95 nanoorganization at 0, 30, 60, and 120min following LTP compared to control. Data shown as mean +/- SEM. M-W test showed significant difference: 0min *p=0.039 and 120min ****p<0.0001. **(B)** Single AMPA cluster area at 0, 30, 60, and 120min following LTP compared to control. Data showed as median +/- 95% C.I. M-W test showed significant difference: 30min **p=0.04, 60min ***p=0.001 and 120min ****p<0.0001. **(C)** Cumulative frequency of single AMPA receptor cluster area during LTP compared to control at different time points after LTP stimulation. Same data as (B). K-S test showed significant difference: 60min *p=0.013 and 120min ***p=0.0004. **(D)** Percentage of spines without AMPA receptor clusters based on PSD95 organizations at 0, 30, 60, and 120min following LTP compared to control. **(E)** Correlation between total PSD95 area and total AMPA receptor area by PSD95 organization at 0, 30, 60, and 120min following LTP compared to control. The exact number of experiments and spines are listed in the table A2.

3.2.4 PSD95 remodeling leads to the addition of new AMPA receptor clusters

In the previous section, we showed that the number of silent synapses gradually disappeared following LTP, and that the average number of AMPA receptor clusters increased. These phenomena could be caused, on one hand, by the appearance of new AMPA receptor clusters on macular PSD95 or, on the other hand, through the remodeling of PSD95 morphology. To test this hypothesis, the morphology of PSD95 after LTP and the number of AMPA receptor clusters on different PSD95 organizations was investigated. I quantified the proportion of different PSD95 morphologies: macular, perforated, segmented 2 and segmented ≥ 3 (Figure 3.10). A higher proportion of perforated and segmented PSD95 was observed after LTP (Figure 3.10.B). Therefore, less macular PSD95 compared to the unstimulated neurons was seen, which coincided with the results described in section 3.1.5 using live STED imaging of endogenous PSD95 after LTP (Figure 3.10.B). Immediately after LTP (0min), the occurrence of macular PSD95 (79%) was slightly decreased compared to control (87%) due to a slight increase of perforated PSD95 (LTP: 8% vs Ctrl: 6%) and segmented 2 PSD95 (LTP: 11% vs Ctrl: 7%) (Figure 3.10.B). At time points 30 and 60min following stimulation, the percentage of perforated (30 min: LTP 10% vs Ctrl 5%; 60min: LTP 11% vs Ctrl 4%) segmented 2 PSD95s (30min: LTP 10% vs Ctrl 7%; 60min: 11% vs 9%) were similar to time point 0min. As well as, at the same times points, the number of macular PSD95 after LTP induction (30min: LTP 78% vs Ctrl 88%; 60min: LTP 75% vs Ctrl 86%) were similar to time point 0 (Figure 3.10.B). At 120min after LTP, the distribution of PSD95 nanoorganizations became significantly different than in the control condition (Figure 3.10.B). This significance was not observed at time points 0, 30, and 60min. For instance, at 120min, the proportion of macular PSD95s decreased to 59% compared to 82% in control, and the percentage of perforated PSD95s increased to 22% vs 3% in control, and the percentage of segmented 2 also increased to 18% vs 12% in control.

Afterwards, the number of AMPA receptor clusters was investigated in relation of different PSD95 morphologies. The different PSD95 nanoorganizations with their AMPA receptor nanodomains are shown in Figure 3.10.A. In Figure 3.10.D, we plotted the number of AMPA receptor clusters and the percentage of their appearance as a function of different PSD95 morphologies. This revealed that macular PSD95 had

mostly one AMPA receptor cluster with an occurrence of 67% and 11% silent synapses. Only 18% of macular PSD95s possessed 2 AMPA receptor clusters, 4% had 3 clusters and 0.3% contained 4 clusters (Figure 3.10.D). For example, in Figure 3.10.A, the STED image shows a macular PSD95 with one AMPA receptor cluster and another macular PSD95 with four AMPA receptor clusters (Inset 1). Furthermore, perforated PSD95s exhibited extra AMPA receptor clusters compared to macular PSD95s with a 41% occurrence of one AMPA receptor cluster, 34% for 2 clusters, 20% for 3 clusters, 2% of 4 clusters, and 1% for 0 clusters (Figure 3.10.D). An example of perforated PSD95 is shown with 1 AMPA receptor cluster in Figure 3.10.A inset 2. This image shows that the area of AMPA receptor clusters on perforated PSD95s is much larger than this one on macular PSD95 (figure 3.10.A inset 2). Segmented 2 PSD95, for its part, presented an occurrence for 1 AMPA receptor cluster of 46%, which indicates that only one of the two PSD95 segments was occupied by an AMPA receptor nanodomain. Also, 40% of segmented 2 PSD95 possessed 2 AMPA receptor clusters, as seen in the STED image in Figure 3.10.A (inset 3). For completeness, 11% of segmented 2 PSD95 assemblies had 3 AMPA receptor clusters, 1% had 4 AMPA receptor clusters, and 2% had no AMPA receptor clusters (Figure 3.10.D). Finally, segmented 3 PSD95s possessed a higher number of AMPA receptor clusters on its structure compared to the other morphologies with a frequency of 23% for 1 AMPA receptor clusters, 27% for 2 AMPA receptor clusters, 31% for 3 AMPA receptor clusters, and 19% for 4 AMPA receptor clusters. An example of segmented 3 PSD95 with three AMPA receptor nanodomains is shown in Figure 3.10.A (inset 4). Remarkably, silent synapses were not present on perforated or segmented PSD95s. Therefore, the remodeling of PSD95 from macular into perforated and/or segmented PSD95 considerably affected the number of AMPA receptor nanodomains at the synapse.

Finally, the number of AMPA receptor clusters on segmented 2 PSD95s was questioned because 46% of them possessed only one AMPA receptor cluster for 2 segments. This indicates that one PSD95 segment had one AMPA receptor cluster while the other one had none. Did LTP induction promote the appearance of AMPA receptor clusters on the empty PSD95 segment of segmented 2 PSD95? The number of AMPA receptor nanodomains was then counted for every segment of segmented 2 PSD95 of the stimulated and unstimulated spines at 0, 30, 60, and 120min after LTP induction (Figure 3.10.C). No change was observed at 0, 30 and 60min after LTP

compared to the control (0min: LTP 0.77 ± 0.10 vs Ctrl 0.62 ± 0.18; 30min: LTP 0.7 ± 0.09 vs Ctrl 0.71 ± 0.12; 60min: LTP 0.70 ± 0.09 vs Ctrl 0.074 ± 0.11). A significant increase of AMPA receptor clusters per PSD95 segment was detected at 120min after LTP where the average cluster per segment was slightly higher than 1 (LTP 1.03 ± 0.06 vs Ctrl 0.82 ± 0.08) (Figure 3.10.C). Therefore, LTP induced structural remodeling of macular PSD95s into segmented 2 and/or perforated PSD95s, and 2h after stimulation, all PSD95 segments of the segmented 2 organization became populated with AMPA receptor clusters.

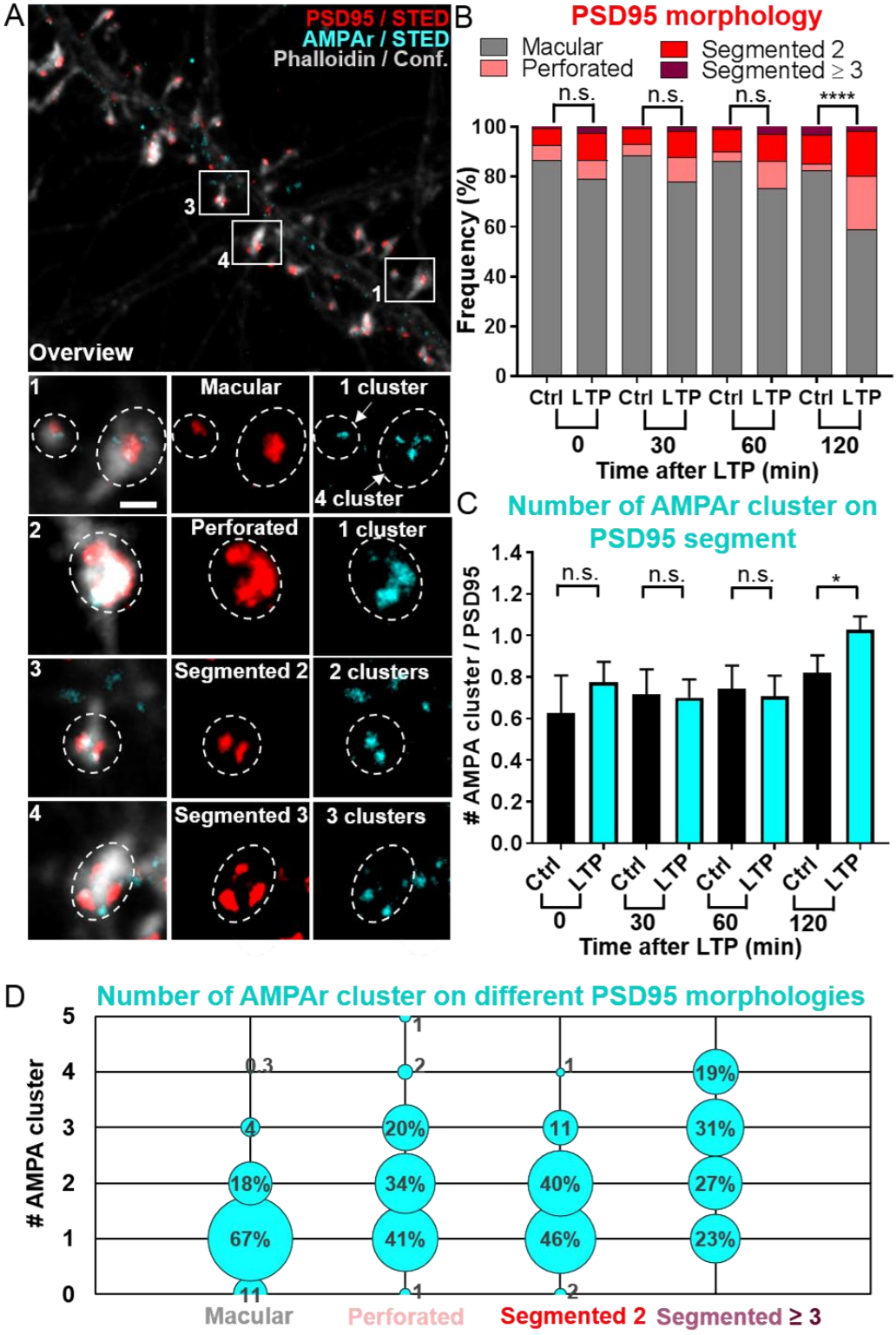

Figure 3.10 PSD95 remodeling and AMPA receptor clusters appearance following LTP. (A) Images of macular, perforated, segmented 2, and segmented 3 PSD95s with the number of AMPA receptor (AMPAr) clusters located on the PSD95 nanoorganization. Scale bar: 500nm. Imaging parameters are listed in the table A1. **(B)** Frequency of different PSD95 morphologies at 0, 30, 60, and 120min following LTP compared to control. K-S test showed a significant difference in the cumulative distribution of PSD95 morphology at 120min: ****p< 0.0001. **(C)** The number of AMPA receptor clusters per PSD95 segment of segmented 2 PSD95 at 0, 30, 60, and 120min following LTP compared to control. Data are represented as mean ± SEM. M-W test showed a significant difference: *p=0.0498. **(D)** Frequency of number of AMPA receptor clusters as function of different PSD95 morphologies. The exact number of experiments and spines are listed in the table A2.

3.2.5 Simultaneous enlargement the area of PSD95 and Bassoon assemblies after LTP induction

In the previous section of this chapter, we showed that the enlargement and remodeling of PSD95 during LTP is accompanied by an increase of the number and the area of single AMPA receptor nanodomains. Therefore, the formation of pre- and postsynaptic nanomodules and their transsynaptic alignment into nanocolumns with glutamatergic receptors suggests that enlargement and remodeling of PSD95 might have a similar effect on the active zone. Thus, we asked whether the size and morphology of the active zone protein Bassoon follows the same tendency as the PSD95 organization after LTP induction. We performed a fixation and immunostaining of cultured hippocampal neurons at different time-points of 0, 30, 60 and 120min after 5min of induction of chemical LTP (Figure 3.11.A-B). We labeled the neurons with antibodies Bassoon, PSD95 and phalloidin, the actin cytoskeleton, as described in section 3.2.1. Bassoon and PSD95 were recorded with STED microscopy. We analysed only Bassoon to PSD95 assembly. PSD95 assembly, in turn, was only analysed when located on a spine that was visualized with phalloidin staining. The total area of colocalized Bassoon and PSD95 was measured via summation of the pixel area of each protein. We found a significant area increase of the Bassoon nanoorganization at 60min (LTP: 0.238 ± 0.018 μm² vs Ctrl: 0.172 ± 0.013μm²) and 120min (LTP: 0.236 ± 0.023μm² vs Ctrl: 0.194 ± 0.012μm²) after LTP compared to the control condition. At the same time points a significant enlargement of PSD95 assemblies was observed (60min: LTP 0.223 ± 0.022μm² vs Ctrl 0.190 ± 0.013μm² ; 120min: LTP 0.244 ± 0.026μm² vs Ctrl 0.173 ± 0.017μm²) (Figure 3.11.C-D). Furthermore, the cumulative area distribution of Bassoon and PSD95 assemblies also showed the same increase (Figure 3.11.E-F). Indeed, the total area of PSD95 and Bassoon assemblies of stimulated neurons manifests larger scaffold protein assemblies compared to control, which were significant at 60min and 120min after LTP induction (Figure 3.11.E-F). This tendency is also observed in the STED images of Bassoon and PSD95 following LTP stimulation (Figure 3.11.A-B). PSD95 and Bassoon were larger, with a greater morphologic diversity, at 60 and 120min after LTP induction compared to the unstimulated neurons, in which the PSD95 and Bassoon nanostructures were small macular (Figure 3.11.A-B). Moreover, PSD95 and Bassoon architecture looked very similar (Figure. 3.11.A-B). Therefore, the area of PSD95 and Bassoon assemblies increased simultaneously after LTP induction.

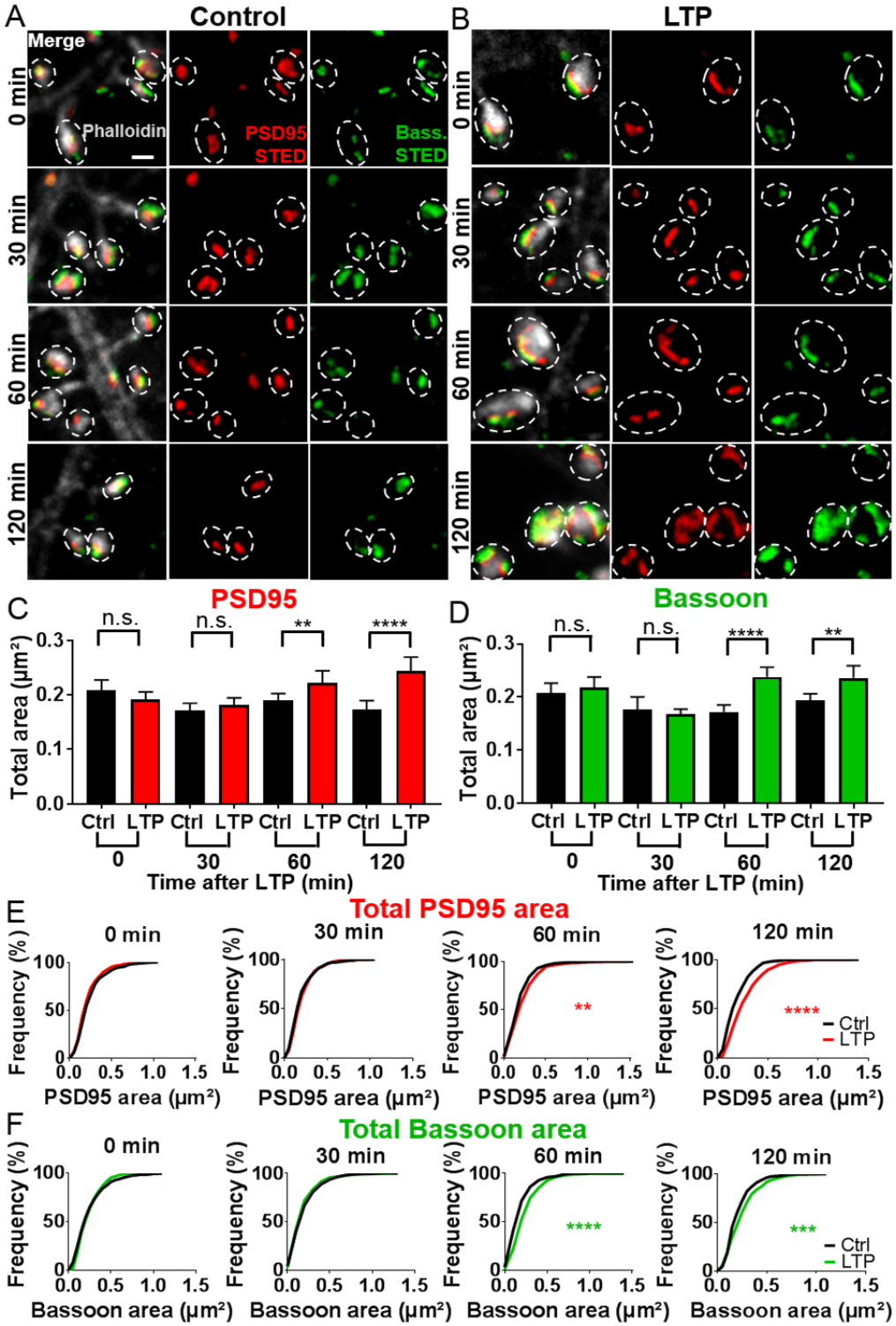

Figure 3.11 LTP promotes on increase in the size of PSD95 and Bassoon assemblies. (A-B) Two-color STED imaging of PSD95 and Bassoon, with actin (phalloidin) in confocal. The pictures were taken at 0, 30, 60, and 120min after LTP stimulation of hippocampal cell cultures (17DIV) (B) or without stimulation as a control (A). Imaging parameters are listed in table A1. Scale bar: 500nm. **(C)** Total PSD95 area per spine at 0, 30, 60, and 120min following LTP compare to control. Data shown as median +/- 95% C.I. M-W test showed significant difference: **p=0.0017 and ****p<0.0001. **(D)** Same as (C), but for total Bassoon area per spine. ****p <0.0001 and **p=0.0016. **(E)** The cumulative frequency of the total PSD95 area after LTP stimulation compared to control at different time points. Same data as (C). K-S test showed significant difference: **p= 0.0043 and ****p <0.0001. **(F)** Same as (G), but for total Bassoon area ****p <0.0001 and ***p=0.0003. Same data as (C). The exact number of experiments and spines are listed in table A2.

3.2.6 Morphological changes in PSD95 and Bassoon appear simultaneously

In the last section we have shown that both PSD95 and Bassoon assemblies areas increase after activation by LTP. Next, we investigated if this increase is synchronized and the consequence it has on the nanoorganization of PSD95 and Bassoon. Different morphologies of PSD95 with Bassoon nanoorganization are displayed in the Figure 3.12.A. We found that Bassoon was also organized in macular, perforated, segmented 2, and segmented 3 structures. Two-color STED reveals a structural correlation between PSD95 and Bassoon (Figure 3.12.A). This indicates that macular Bassoon is associated with macular PSD95, perforated Bassoon with perforated PSD95, segmented 2 Bassoon with segmented 2 PSD95 and segmented 3 Bassoon with segmented 3 PSD95 (figure 3.12.A). Thus, the Bassoon organization appeared to be paired with similar PSD95 morphology.

To quantify these observations, the morphologies of Bassoon and PSD95 were analyzed at 0, 30, 60, and 120min following LTP. The results for PSD95 morphology were comparable to the previous results obtained from two-STED imaging of PSD95 and AMPA receptor clusters in section 3.2.4. The distribution of different PSD95 morphologies was again significantly different at 120min after LTP induction (Figure 3.12.C). Furthermore, the distribution of morphologies of Bassoon revealed a difference at 120min after LTP stimulation compared to control (Figure 3.12.D). This observed change was due to an increase of perforated (LTP: 8% vs Ctrl: 4%), segmented 2 (LTP: 28% vs Ctrl: 20%), and segmented 3 (LTP: 7% vs Ctrl: 5%) Bassoon nanostructures compared to control (Figure 3.12.D). At 0min and 30min after LTP, the frequency of different Bassoon morphologies was comparable to control. At 60min after LTP, there was a higher level of perforated (LTP: 8% vs Ctrl: 2%) and segmented 3 (LTP: 8% vs Ctrl: 5%) Bassoon as compared to the control condition, but this difference was not significant (Figure 3.12.D). The increase of perforated and segmented 2 PSD95s at 120min after LTP induction (figure 3.12.C) was accompanied by an increase of perforated, segmented 2, and segmented 3 Bassoon (Figure 3.12.D). Therefore, the morphological changes of PSD95 and Bassoon were synchronized.

Afterwards, the occurrence of Bassoon with different PSD95 nanoorganizations was inspected in order to detect the correlation between PSD95 and Bassoon

morphologies (figure 3.12.E). We found a frequency of 77% for the occurrence of macular PSD95 with macular Bassoon, 23% for perforated PSD95 with macular Bassoon, 23% for segmented 2 PSD95 with macular Bassoon, and only 3% segmented 3 PSD95 with macular Bassoon. Thus, macular-macular was found to be the predominant correlation between PSD95 and Bassoon nanomorphology (Figure 3.12.E). Furthermore, perforated Bassoon showed a predominance associated with similar structured, perforated PSD95 (20%). However, perforated Bassoon very rarely occurred with macular PSD95 (3%) or segmented 2 PSD95 (5%). Moreover, segmented 2 Bassoon was mostly paired with segmented 2 PSD95 (54%) Finally, segmented 3 Bassoon was mainly coupled with segmented 3 PSD95 (61%), 23% with perforated PSD95, and 18% with segmented 2 PSD95 (figure 3.12.E). Therefore, Bassoon and PSD95 changed their structure simultaneously following LTP.

At last, the correlation between the area of PSD95 and Bassoon assemblies was analyzed to confirm whether changes between PSD95 and Bassoon arise in conjunction (Figure 3.12.B). Indeed, the correlation was maintained over all time points after LTP induction (Figure 3.12.B). Moreover, the slope of the regression line of stimulated neurons was not significantly different compared to the unstimulated neurons. PSD95 area was slightly, but not significantly, higher compared to control at 120 min after LTP (Figure 3.12.B). Thus, PSD95 and Bassoon structural changes were tied together, considering the correlation between these scaffold proteins stayed intact during enlargement and remodeling for up to 120min after LTP induction.

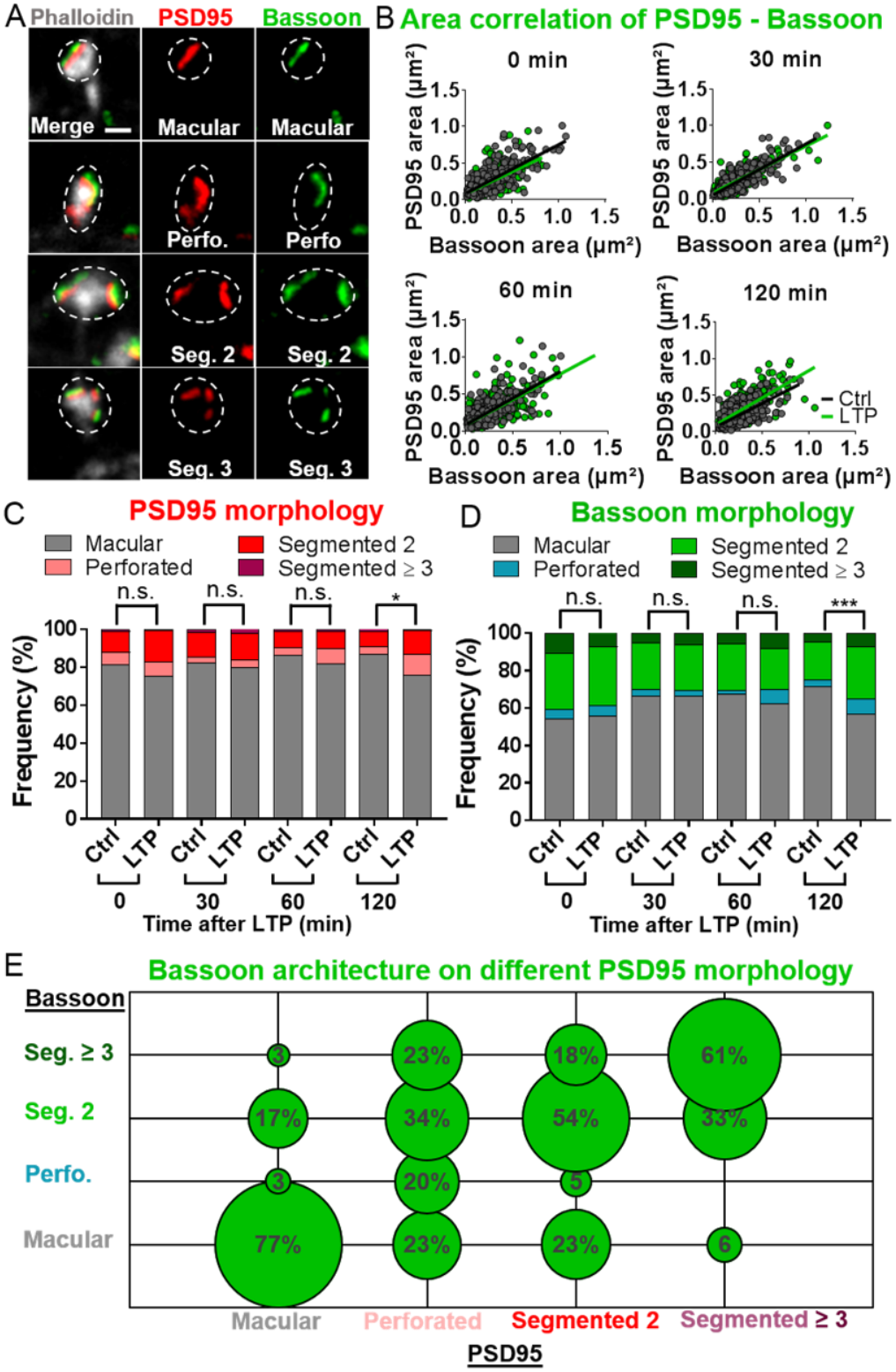

Figure 3.12 Morphological changes of PSD95 and Bassoon assemblies after LTP induction. (A) Images of macular, perforated, segmented 2 and segmented 3 PSD95 morphology with Bassoon nanoorganization. Scale bar: 500nm. Imaging parameters are listed in the table A1. **(B)** Correlation between total PSD95 area and total Bassoon area per spine at 0, 30, 60, and 120min following LTP compared to control. **(C)** Frequency of different PSD95 morphologies at 0, 30, 60, and 120min following LTP compared to control. K-S test shows a significant difference in the cumulative distribution of PSD95 morphology at 120min: *p=0.014. **(D)** Same as (C), but for Bassoon morphologies. 120min: ***p=0.0002. **(E)** Frequency of Bassoon morphology on different PSD95 nanoorganizations. The exact number of experiments and spines are listed in table A2.

4. Discussion

4.1 Chemical LTP promotes remodeling of PSD95

4.1.1 Chemical LTP induces an increase of PSD95 area

The first aim of my project was to investigate the nanorganization of endogenous PSD95 expression and the change induced by chemical LTP during a 2h live-STED imaging time-lapse following LTP induction. To my knowledge, this is the first study that investigated the transformation of the PSD95 nanoarchitecture and formation of perforated PSD95 after induction of chemical LTP. The dynamic modifications of the PSD95 assembly were explored in changes of their total area and in changes of their nanoorganization. The PSD95 area expanded (27% ± 5%) with a delay of 1h after chemical LTP only in potentiated spines when compared to control (Figure 3.2.D). In unpotentiated spines and with an NMDA receptor inhibitor (APV), PSD95 area remained unchanged after chemical LTP. These results suggest that NMDA receptor activation is necessary for the LTP-induced change in PSD95 nanoorganization. Additionally, there was a broadening area distribution of PSD95 area at 1h after LTP induction compared to control (Figure 3.2.F). Therefore, PSD95 expansion depends on the late phase of LTP due to the delay of 1h before the change occurs. These results are supported by the research of Meyer et al. and Bosch et al., which also show an increase of PSD95 volume at 1h after LTP induction (Bosch et al., 2014; Meyer et al., 2014). At 2h after LTP, potentiated spines displayed an increase in PSD95 area of 15% ± 6% that was not significant compared to control, but significant when compared with unpotentiated spines (Figure 3.2.D). A potential explanation of this non-significant change in PSD95 area 2h after chemical LTP could be the fewer data points collected after 2h (n= 59 spines) compared to 1h (n= 108 spines) and 30 min (n= 103 spines) after LTP. Therefore, collecting more data points at the 2h after LTP condition could make the area increase of PSD95 assembly on potentiated spine significantly different compared to control.

A critical parameter for the analysis of PSD95 enlargement is the threshold at which a spine is regarded as potentiated. For example, in the Meyer et al., (2014) paper, this threshold was varied for different experiments (Meyer et al., 2014). For my analysis, I

chose 1 SD above baseline as the threshold for determination of a potentiated spine at 1h and 2h after LTP induction (1 SD during baseline refer to Appendix Figure A1.D). Another critical aspect of my analysis was the degrading fluorescent signal during the time-lapse imaging that affected the measured area. Although I used the antibody-like FingR-PSD95 to label endogenous PSS95 and not introducing overexpression artefacts, the fluorescent signal was relatively low and degraded over the 2h time-lapse imaging. It is also possible that bleaching of the fluorophore occurred preferentially at the periphery of the PSD95 cluster after every image acquisition and slightly affect the area of the cluster. Unfortunately the exchange rate of PSD95 is very low and these PSD95 molecules are not replaced because they are nearly immobile under the basal condition (Fukata et al., 2013). However, I performed a detailed analysis of this effect and only found a small decrease of 14% of PSD95 area after taking 4 STED image stacks (Appendix Figure A1.E), while the area of the spine head did not show any variation (Appendix Figure A1.D). This area reduction is also present in the control condition of my data during the time course of LTP stimulation as shown in Appendix Figure A2.B. Since this reduction in area after multiple imaging was affected by the imaging itself, I normalized the changes of PSD95 area and the changes of the spine head area to the control. A similar normalization was used by Meyer et al. (Meyer et al., 2014).

Furthermore, my data demonstrate a tendency of primarily smaller spines to enlarge after LTP induction, which is in line with the research of Matsuzaki et al. (Figure 3.3.C)(Matsuzaki et al., 2004). Using two-photon microscopy combined with glutamate uncaging, they found that small spines are more likely to persistently enlarge after LTP than larger ones(Matsuzaki et al., 2004). Moreover, my data demonstrated that the small spines with larger PSD95/spine head area ratio to start with were more likely to be potentiated than the bigger spines (Figure 3.3). The higher PSD95/spine head ratio obtained for spines that were potentiated can be caused either by the presence of a larger PSD95 area before LTP or smaller spine head (Figure 3.3.D). As the spine head area is significantly smaller before LTP in the case of potentiated spines compared to unpotentiated spines, the second option is more likely (Figure 3.3.C).

For a better understanding of these increases of PSD95 and spine head area, we analysed the changes as a function of their initial area (Figure 3.4). Interestingly, the

area changes of the spine head and PSD95 correlated very differently with their initial area. After LTP, changes in spine head area increased with their initial area. This supports a Kesten process formulation for dynamic spine analysis that indicates that the enlargement of the spine head is governed by a multiplicative component that is state-dependent (Hazan & Ziv, 2020; Ziv & Brenner, 2018). Therefore, the fast polymerization accompanied by the slow depolymerization rate of actin filaments could act as the multiplicative component during the spine enlargement process (Bamburg 1999).

In a similar way**,** PSD95 dynamics were also investigated. Unlike the spine head dynamics, the area of PSD95 assembly increase after LTP stimulation is regulated by an additive component, which is a state-independent fluctuation (Figure 3.4.B) (Liran Hazan 2020, Noam Ziv 2018). Therefore, synthesis of new protein after LTP could act as the additive component. Furthermore, PSD95 dynamics under basal activity point out the tendency of small PSD95 areas to expand and the larger ones to shrink, which is concordant with the spine head dynamics. This tendency of the small synapses to become stronger and bigger ones to become weaker was also observed by Noam Ziv et al. (Hazan & Ziv, 2020; Ziv & Brenner, 2018). The area distribution of PSD95 is skewed and shifted to larger values 1h after LTP induction (Figure 3.2.F). This supports a model by Shomar et al. on size fluctuation of synapses (Shomar, Geyrhofer, Ziv, & Brenner, 2017). These authors used a model of stochastic binding and unbinding of proteins to a matrix that explains synaptic size fluctuations (Shomar et al., 2017). In this model, an increase in the binding coefficient of the proteins promotes the broadening of the skewed size distribution, which is what we observed for the PSD95 assembly area. However, the exact mechanism and binding partner remains elusive. This model assumes the binding and unbinding of proteins to a matrix. In the case of PSD95, this matrix could be formed by the adhesion molecule neuroligin-1, which is necessary for the precise location of PSD95 at the synapse and the alignment of AMPA receptor nanodomains with presynaptic release of glutamate. Furthermore, the model by Shomar et al. also provides a theoretical basis for the formation of the clusters we and others observed for PSD95 and synaptic proteins (Fukata et al., 2013; Hruska et al., 2018; Wegner et al., 2017). They explain that matrix proteins form “seeds” that can act as nucleation points for nanoclusters. Unfortunately, this model does not include the formation of the perforation like U-shape and ring-like structure of protein

assemblies. Therefore, a more advanced or specific model is needed.

4.1.2 Plasticity of PSD95 nanoorganization after LTP

Next, the morphology of PSD95 after LTP induction was investigated to determine if the area expansion of PSD95 occurs simultaneously with the modification of PSD95 nanoarchitecture. The results obtained via PSD95 morphology analysis after LTP reveals an increase of the percentage of non-macular PSD95, especially at 1h with +13% and 2h after LTP stimulation with +21% (Figure 3.5.B). More precisely, 1h following LTP stimulation, there is a difference of +9% of segmented 2 PSD95 compare to before LTP. At 2h after LTP induction, the proportion of segmented 2 increased by +13% in total, and perforated PSD95 also increased in total by +6%. (Figure 3.5.B) Contrastingly in the control condition, the level of macular PSD95 stays constant at ~90% during the duration of the time-laps duration. Therefore, not just the area of PSD95 increases after LTP, but also a modification of PSD95 nanoarchitecture occurs simultaneously. These results are consistent with a new *in vivo* STED imaging report of endogenous PSD95 from my laboratory, where segmented and perforated PSD95 were observed in the visual cortex (Wegner W, Steffens H, Gregor C, Wolf F, 2020). This study proved the existence of perforated PSD95 assemblies *in vivo* and that these nanoorganizations are highly dynamic, even at baseline. My colleagues recently revealed that the modification of PSD95 nanoarchitecture occurs faster in mice housed in an enriched environmental, which is known to enhance synaptic plasticity of dendritic spines in the visual cortex, in comparison to mice housed in standard conditions (Baroncelli et al., 2010; Greifzu, Kalogeraki, & Löwel, 2016; Wegner W, Steffens H, Gregor C, Wolf F, 2020). Therefore, it suggests that these morphological changes are triggered by experience and synaptic plasticity potentially improves transmission efficiency.

Furthermore, my results are also supported by the research of Stewart et al. using electron microscopy of the electron-dense region of the PSD, including post-synaptic proteins and receptors. They observed an increase of non-macular PSDs of over 17% 1h after chemical LTP (Stewart et al., 2005). However, they observed about 70% of non-macular PSDs in the control condition, which increased to 87% 1h after chemical LTP. My results, in contrast, show that non-macular PSD95 occurs at a frequency of

9% in the basal condition and increases to 22% at 1h and 30% at 2h after LTP (Figure 3.5.B). This discrepancy could be explained by the age of the mice used for this experiment. Stewart et al. use hippocampal acute brain slices of 12-week-old mice while I prepared hippocampal organotypic slices from mice that were used at about ~23 days of maturation (5 days post-natal + 18 DIV). The age difference could explain the observed variation of PSD95 structure between the two studies as perforated PSDs emerge during development (Harris et al., 1992). Harris et al. previously demonstrated that at 15 days post-natal, the spines have macular PSDs with an occurrence of 88%, while in older animals, there is a dominance of perforated PSDs with a frequency of 81% (Harris et al., 1992). Electron microscopy with the 3D reconstruction allows to resolve the protein details in X, Y, Z plane. Thus, employing 3D-STED would reveal the complete 3D morphology of PSD95 and not just the ones restricted to the X, Y focal plane. However, the Z resolution is about 500nm, which is not enough is to reveal the perforation of the scaffold protein organization. The STED microscopes I used for live-cell imaging offer only superresolution in the X, Y plane. Being able to superresolve perforations only in the X, Y plane, the total proportion of perforated PSD95 is most likely higher in total

Moreover, my data are also consistent with the research of Hruska et al., where they observed the appearance of a second PSD95 nanomodule in the spine head after chemical LTP induction (Hruska et al., 2018). However, my data shows a predominant augmentation of segmented 2 PSD95, which is equivalent to 2 nanomodules in Hruska et al., in hippocampal organotypic slices at 1h (+ 9%) and 2h (+13%) post LTP, while Hruska et al. saw the increase immediately after LTP induction (Figure 3.5.B). In detail, Hruska et al. used a very similar construct, FingR-PSD95-EGFP, and very similar LTP protocol, as well as superresolution STED microscopy (Hruska et al., 2018). However, they show the number of PSD95 nanomodules per spine is already significantly increased by ~2 times immediately after LTP stimulation in cortical neuronal cultures (Hruska et al., 2018). Nevertheless, in my experiment, the formation of segmented 2 PSD95 arise together with the area expansion of PSD95 at 1h following LTP (Figure 3.5.B). The filling ratio analysis of potentiated spines is also significantly different at 1h and 2h after LTP induction, which confirms the morphological change of macular into segmented and/or perforated PSD95 by 1h (Figure 3.5.D). Therefore, modification of PSD95 nanoarchitecture occurs simultaneously with increased area of PSD95

assembly. Furthermore, Hruska et al., observed an increase of PSD95 mobility following LTP induction (Hruska et al., 2018). The mobility of the PSD95 assembly was also improved during palmitoylation activity and nanodomain formation (Fukata et al., 2013). Therefore, potentiated spines and formation of PSD95 nanodomains by palmitoylation activity present highly dynamic PSD95 assemblies that are likely necessary for morphological changes of PSD95 assembly.

Furthermore, the enrichment of perforated PSD95s at 2h after stimulation reveals a potential role for this newly discovered structure in transmission efficiency (Figure 3.5.B). Notably, the appearance of perforated PSD95s seems to occur during the formation of the spine apparatus, which also takes place at 2h after LTP induction (Chirillo et al., 2019). In addition, the increase in the proportion of spine apparatuses is accompanied by PSD area enlargement in the spine containing a smooth endoplasmic reticulum and polyribosomes, which are subcellular resources necessary for local proteins synthesis (Chirillo et al., 2019). The increase of perforated PSD95 along with the spine apparatus would be coherent with previous research showing that the majority of perforated PSDs are hosted by a spine containing a spine apparatus (Harris et al., 1992). Consequently, the formation of the spine apparatus promotes local protein synthesis, a necessary process for the late phase of LTP (Pierce et al., 2000). Therefore, the formation of perforated PSD95 in conjunction with the appearance of the spine apparatus might be a feature of L-LTP and new protein synthesis.

The shape analysis of macular, perforated, and segmented PSD95 presented in this thesis was performed by visual inspection only. It was sometimes difficult to attribute a morphology to the PSD95 nanoarchitecture. For this reason, a software that can reveal different PSD95 morphologies would help to avoid the variation induced by the subjective perception of the person performing the analysis. For instance, machine learning could be a good strategy to counterpart the variability of shape attributes to PSD95 nanoorganization. A new report using STED microscopy combined with machine learning for analysis revealed different PSD95 structures but does not include perforated PSD95. Interestingly, elongation of PSD95 structure was observed immediately after 10min of chemical LTP stimulation of cultured hippocampal neurons (Wiesner et al., 2020).

4.1.3 Structural remodelling of small and large PSD95 assemblies

I observed that PSD95 expansion occurs mostly in small spines that usually have a small PSD95 assembly. For this reason, the population of PSD95 nanoorganizations was split into small and large areas to investigate the remodeling of PSD95 nanorganization after LTP induction. The area of small PSD95 assemblies significantly increased at 1h after LTP, which is about 2 times more than the large PSD95 at the same time point (Appendix Figure.A2.E-F) However, the small PSD95s, which were mainly composed of macular PSD95 (97%), showed less structural modifications than larger PSD95 assemblies, especially at 2h after stimulation (small: 82% macular; large: 55% macular) (Figure 3.6). Therefore, it suggests that larger PSD95 assemblies are in larger spines containing rich subcellular resources, like polyribosomes and SER, which could promote structural changes of the PSD95 assembly (Chirillo et al., 2019). Intriguingly, the levels of macular (82%), segmented 2 (12%), and perforated PSD95 (6%) at 2h after LTP induction of initially small PSD95 are comparable to the proportion of 83% macular, 13% segmented 2 and 4% perforated observed for large PSD95 before LTP (Figure 3.6). This suggests that the small PSD95 becomes stronger after one event and further structural modifications appear from event to event. Thus, PSD95 assembly area first increase and then form perforations and segmentation after the next LTP event. The area increase of small PSD95 assembly after LTP stimulation could promote the transformation of small and transient spines containing small PSD95s, into larger and persistent spines with larger PSD95 assemblies, as the size of PSD95 and spine head are correlated (Meyer et al., 2014). The following transformation of PSD95 assembly into perforated and segmented PSD95 might be a second feature involved in the stabilization and maintenance of LTP. This is supported by an *in vivo* experiment in mice, where they observed a proportion of small spines appeared and disappeared after a few days, while the large spines were persistent for more than a month under basal activity (A. J. G. D. Holtmaat et al., 2005; A. Holtmaat, Wilbrecht, Knott, Welker, & Svoboda, 2006). Finally, the sustained increase of mEPSC amplitudes to 1h after chemical LTP induction, supports the theory of increased AMPA receptor nanodomain content and/or the number of vesicles released after LTP (Figure 3.2.E). Therefore, the area increases and remodeling of the PSD95 structure could provide new slots for the incorporation of new AMPA receptors.

4.1.4 Summary

The results obtained via live-cell STED imaging indicate that the PSD95 assembly area increases with a delay of about 1h following LTP that is likely due to de novo protein synthesis during the late phase of LTP. Furthermore, the increased area occurs simultaneously with the remodeling of PSD95 nanoarchitecture after LTP. A time-course reveals that the proportion of perforated and segmented 2 PSD95 increases with a similar delay following LTP stimulation. Additionally, the formation of perforated PSD95 is correlated with the formation of the spine apparatus 2h after LTP. Therefore, perforated PSD95 could be a secondary feature and related to protein synthesis during L-LTP. It would be enlightening to track de Novo protein synthesis of PSD95 using a photoconvertible fluorescent protein tag with PSD95. The changes in protein nanoorganization would then be separable from the addition of newly synthesized proteins. Moreover, most of the increase of PSD95 assembly area occurred in small spines hosting small PSD95s, but the proportion of perforated and segmented 2 PSD95s is higher for larger PSD95 assemblies. Therefore, area increases and structural remodeling of PSD95 emerge one after the other to improve the synaptic strength of the synapse.

4.2 Modification of PSD95 nanoarchitecture occur in conjunction with changes in Bassoon and AMPA receptor nanoorganization

I performed two-color STED microscopy of PSD95 and AMPA receptors, and PSD95 and Bassoon to determine if the increased area and structural changes of PSD95 during LTP also improve the strength of the synapse. In a third confocal channel, I imaged F-actin. Thus, I was able to identify dendritic branches and assign the PSD95 assembly to dendritic spines. I analyzed the area and number of AMPA receptor nanodomains, as well as Bassoon assembly area and morphology, following LTP induction.

4.2.1 Nanoplasticity of AMPA receptors following LTP

My results reveal that the total area of both AMPA receptor clusters and PSD95 increase together at 30, 60, and 120min after LTP induction. This increase is simultaneous as the slope of the regression line between PSD95 and AMPA receptor

total area was equal to control for all time points (Figure 3.9.E). Therefore, these results suggest that when a new PSD95 slot is formed, it is immediately populated by a new AMPA receptor.

However, the increase of total AMPA receptor cluster area during LTP can be caused on one hand by the augmentation of AMPA receptor nanodomain number or, on the other hand, by adding more AMPA receptors to one AMPA receptor nanodomain. To explore the first option, I labeled the GluA2 subunit of the AMPA receptor and analyzed the number of GluA2 containing AMPA receptor nanodomains. This revealed a fast and significant increase in the number of AMPA receptor clusters immediately after LTP (Figure 3.9.A). These results are consistent with the fast exocytosis of the GluA1-containing AMPA receptors during LTP, since most of the synaptic receptors (~80%) are composed of GluA1 and GluA2 subunits (W. Lu et al., 2009; Patterson et al., 2010). This can explain my observation that the number of AMPA receptor nanodomains formed with GluA2-subunit increases rapidly after LTP induction. Therefore, it suggests that there is already an available slot in PSD95 waiting for the fast exocytosis and lateral diffusion of the AMPA receptors immediately after LTP stimulation. However, the strongest increase of AMPA receptor nanodomains was observed at 2h after LTP. This increase occurred at the same time as the vanishing of silent synapses and gaining of one AMPA receptor nanodomain (Figure 3.9.D). Moreover, almost all silent synapses were in the spine as macular PSD95 (11%), which suggests the activation of silent macular PSD95 after LTP (Figure 3.10.D). These results are consistent with the research done by Nair et al. where they also observed a frequency of 15% of silent synapses using STED microscopy that occurred on smaller PSD95 assemblies (Nair et al., 2013). Nevertheless, the appearance of AMPA receptor nanodomains observed at 2h after LTP also correlate in time with the formation of perforated and segmented 2 PSD95s (Figure 3.10.B). Indeed, at 2h after LTP, a significant increase of non-macular PSD95 was observed compared to control that was due to the augmentation of perforated and segmented 2 PSD95s (Figure 3.10.B). Notably, perforated PSD95 mostly hosted 2 or 3 AMPA receptor nanodomains, while macular PSD95 mainly possessed one AMPA receptor cluster (Figure 3.10.D). Thus, the transformation from macular to perforated PSD95 should boost the synaptic strength. Furthermore, about half of segmented 2 PSD95s contain only one AMPA receptor nanodomain 1h after LTP induction, but 2h following LTP induction most of segmented 2 PSD95 contained

2 AMPA receptor nanodomains (Figure 3.10.C-D). This suggests that during the formation of segmented 2 PSD95, the second PSD95 segment is not immediately activated and becomes unsilenced around 2h after LTP induction. Therefore, the activation of silent synapses goes hand in hand with the augmentation of perforated and/or segmented 2 PSD95 at 2h after LTP and thus an increase in the number of AMPA receptor nanodomains found at the synapse.

The area of one AMPA receptor nanodomain was also explored after LTP induction. Individual AMPA receptor nanodomains enlarged at 30, 60, and 120min, simultaneous with PSD95 area increase. The magnitude of enlargement of the AMPA receptor nanodomains also increased with time after LTP. This enlargement could be caused by the exchange of AMPA receptor subunits from GluA1 monomers to GluA1/GluA2 heterotetramers, which occurs at 25 min after LTP (Plant et al., 2006). Furthermore, the enlargement of a single AMPA receptor nanodomain area suggests an increase in the number of GluA2-subunits of AMPA receptor per nanodomain. This increase of AMPA receptors per nanodomain might raise the number of intramolecular collisions via macromolecular crowding and improve the ability of PSD95 to interact with TARP for the retention of AMPA receptors at the synapse (Santamaria, Gonzalez, Augustine, & Raghavachari, 2010). The enlargement of one AMPA receptor cluster should have a positive effect on mEPSC amplitude. Indeed, an increase of mEPSC amplitude was also observed at 30min after chemical LTP induction. Thus, the increased size of AMPA receptor nanodomains and morphological changes of PSD95 nanorganization are two co-occurring features to enhance synaptic transmission efficiency via incorporation of AMPA receptor nanodomains following LTP. These results are supported by Nair et al., where they detect an increase of AMPA receptor nanodomain number and size after overexpression of PSD95 (Nair et al., 2013). Moreover, the overexpression of PSD95 is known to induce the formation of perforated PSDs and larger synapses (Nikonenko et al., 2008). Therefore, the modification of the PSD95 architecture from macular into perforated and/or segmented PSD95 will increase the number of AMPA receptor nanodomains and improve synaptic strength. Consequently, the formation of perforated PSD95 after LTP could allow the newly incorporated AMPA receptor nanodomains to be perfectly aligned with the presynaptic active zone to enhance transmission efficiency.

4.2.2 Nanoplasticity of Bassoon and PSD95 following LTP

On the other side of the synapse, the area of the Bassoon assembly increased simultaneously with the area of the PSD95 assembly at 1h and 2h post LTP induction. Similar to the AMPA receptor cluster analysis, the Bassoon area also conserved its correlation with PSD95 area after LTP induction (Figure 3.12.B). This suggests that the modification of PSD95 and Bassoon architecture occurs together. These results are in line with the research of the Harris laboratory where they observed an increase of the active zone together with PSD area at 2h after LTP induction (Bell et al., 2014). Furthermore, similar to the PSD95 assemblies, Bassoon morphology analysis revealed an increase of non-macular Bassoon 2h post LTP compared to control (Figure 3.12.D). Likewise, the correlation of Bassoon and PSD95 structure revealed a stronger correlation between the same morphology of protein assembly (Figure 3.12.E). However, perforated PSD95 was most likely to appear with segmented 2 Bassoon (Figure 3.12.E). Therefore, the area increases and modification of PSD95 morphology into perforated and segmented occurs simultaneously with the modification of the active zone protein Bassoon and suggests an increase of neurotransmitter release for those morphologies. These results are also consistent with the report of Toni et al., which indicated that perforated PSDs emerged during LTP and possessed ~30% more presynaptic readily releasable vesicles than macular PSDs (N Toni et al., 2001). A new study using STED nanoscopy and machine learning analysis also supports my data (Wiesner et al., 2020). They report an elongation of Bassoon structure and increased correlation between PSD95 and Bassoon following chemical LTP (Wiesner et al., 2020). Thus, morphological changes of PSD95 and Bassoon nanorganization occur together following LTP, possibly to improve the alignment between the presynaptic release of neurotransmitters and the appearance of new AMPA receptor nanodomains.

Although STED superresolution was necessary to resolve the nanoorganization of synaptic proteins, we can only resolve with nanoscale resolution in the X, Y plane. To resolve all nanoorganizations, we would need ~ 50nm resolution in all 3 dimensions. However, with our two-color STED microscope, we achieved only a resolution of 100 x 135 x 135 in Z, X, Y, which is not enough to reveal all perforated PSD95 or the Bassoon nanoarchitecture. For this reason, I decided to perform 2D STED imaging of PSD95-AMPA and PSD95-Bassoon, which allowed me to have a resolution of ~55 nm in both channels in order to resolve all morphologies present in the X, Y focal planes

(Van Dort, 2018).

Finally, different neuronal cell culture preparations can also introduce some variation in synaptic area and/or morphology. As well, variation can be induced by the different ages of the neuronal cultures, which were between 16 and 21 DIV. For instance, it was demonstrated by Harris et al. that perforated PSDs, which are larger than macular ones, emerge during development (Harris et al., 1992).

4.2.3 Summary

In summary, my results show that the expansion and remodeling of PSD95 are accompanied by an increase of the number and area of single AMPA receptor nanodomains. The area increases of one AMPA receptor nanodomain was correlated with the area increase of PSD95, while the increase in number seems to be correlated in time with the activation of silent synapses and/or by the morphological change of PSD95 nanoarchitecture into perforated or segmented 2. Furthermore, the Bassoon area also increased in hand with PSD95 assembly area and the morphological analysis suggests that they undergo a synchronized structural remodeling. Therefore, the area increases and morphological changes of PSD95 assembly occur together with changes in Bassoon nanoorganization. This synchronisation possibly promotes the formation and/or enlargement of a trans-synaptic nanocolumn or to improve the trans-synaptic nanocolumn alignment of PSD95, AMPA receptors, and Bassoon that will enhance synaptic strength. It would be interesting to observe the formation of trans-synaptic nanoculumns, especially on perforated PSD95, and to follow the dynamic of trans-synaptic nanocolumns of PSD95/Bassoon/AMPA receptor nanodomains via live-cell imaging after LTP induction. Furthermore, in the present thesis I demonstrated that PSD95 area increased together with the area of Bassoon assembly and AMPA receptor nanodomains. Therefore, using a three-color STED microscope to superresolve the trans-synaptic nanoculumns formed by PSD95/Bassoon/AMPA receptor nanodomains should reveal a simultaneous enlargement of Bassoon assembly together with AMPA receptor organization.

5. Conclusion and outlook

In conclusion, using superresolution STED microscopy to access the nanoscale organization of endogenous PSD95 assemblies, I demonstrated both that the total area of PSD95 increases and that the PSD95 nanoarchitecture undergoes modifications following chemical LTP induction. I showed that mainly segmented 2 and perforated PSD95, which are two discontinuous structures of PSD95 assemblies, arise during L-LTP. Using two-color STED imaging of hippocampal cultured neurons following LTP induction, I also demonstrated that the area of the presynaptic active zone protein Bassoon assembly increased simultaneously with the area of the PSD95 assembly. Moreover, the structural remodeling of pre- and post-synaptic scaffold protein assemblies was correlated. Furthermore, I showed that the area of AMPA receptor nanodomains increased in correlation with the area of PSD95 assemblies following LTP. Additionally, the appearance of a new AMPA receptor nanodomains occurred in concert with the remodeling of PSD95 assemblies and/or activation of silent synapses at 2h after stimulation. Therefore, the enlargement and/or appearance of new AMPA receptor nanodomains, as well as the enlargement and remodeling of Bassoon assemblies, following the modification of PSD95 nanoarchitecture increases synaptic strength. Structural remodeling of PSD95 might promote the formation and/or enlargement of trans-synaptic nanocolumns that improve the alignment between AMPA receptor nanodomains with the presynaptic release of glutamate. In the future, it would be interesting to study pre- and post-synaptic nanoorganization and the formation of trans-synaptic nanocolumns *in vivo*. Then it would be possible to directly correlate the synaptic nanophysiology with learning. One way to investigate the trans-synaptic nanocolumn *in vivo* would be to analyze PSD95, Bassoon, and/or AMPA receptor organization in the visual cortex of a living mouse during visual stimulation. A calcium sensor, like GCamP6, could be used as a read out of activated neurons after visual stimulation. Finally, to elucidate if the formation of perforated PSD95 is related to de novo protein synthesis after LTP induction, one could observe the appearance of newly synthesized PSD95 molecules. This could be done by using a photoconvertible fluorescent PSD95 and determining whether they form new segments or incorporate into the existing structure.

Bibliography

Abel, T., Nguyen, P. V., Barad, M., Deuel, T. A. S., Kandel, E. R., & Bourtchouladze, R. (1997). Genetic demonstration of a role for PKA in the late phase of LTP and in hippocampus-based long-term memory. *Cell*. https://doi.org/10.1016/S0092-8674(00)81904-2

Abraham, W. C., Dragunow, M., & Tate, W. P. (1991). The role of immediate early genes in the stabilization of long-term potentiation. *Molecular Neurobiology*. https://doi.org/10.1007/BF02935553

Altrock, W. D., Tom Dieck, S., Sokolov, M., Meyer, A. C., Sigler, A., Brakebusch, C., … Gundelfinger, E. D. (2003). Functional inactivation of a fraction of excitatory synapses in mice deficient for the active zone protein bassoon. *Neuron*. https://doi.org/10.1016/S0896-6273(03)00088-6

Anson, L. C., Chen, P. E., Wyllie, D. J. A., Colquhoun, D., & Schoepfer, R. (1998). Identification of amino acid residues of the NR2A subunit that control glutamate potency in recombinant NR1/NR2A NMDA receptors. *Journal of Neuroscience*. https://doi.org/10.1523/jneurosci.18-02-00581.1998

Araki, Y., Zeng, M., Zhang, M., & Huganir, R. L. (2015). Rapid Dispersion of SynGAP from Synaptic Spines Triggers AMPA Receptor Insertion and Spine Enlargement during LTP. *Neuron*. https://doi.org/10.1016/j.neuron.2014.12.023

Arellano, J. I., Benavides-Piccione, R., DeFelipe, J., & Yuste, R. (2007). Ultrastructure of Dendritic Spines: Correlation Between Synaptic and Spine Morphologies. *Frontiers in Neuroscience*. https://doi.org/10.3389/neuro.01.1.1.010.2007

Aristotle. (1994). De Anima (On the Soul). *Book II, Translated by J.A. Smith, Written 350 B.C.E.*

Baltaci, S. B., Mogulkoc, R., & Baltaci, A. K. (2019). Molecular Mechanisms of Early and Late LTP. *Neurochemical Research*. https://doi.org/10.1007/s11064-018-2695-4

Bamburg, J. R. (1999). Proteins of the ADF/cofilin family: Essential regulators of actin dynamics. *Annual Review of Cell and Developmental Biology*. https://doi.org/10.1146/annurev.cellbio.15.1.185

Baroncelli, L., Braschi, C., Spolidoro, M., Begenisic, T., Sale, A., & Maffei, L. (2010). Nurturing brain plasticity: Impact of environmental enrichment. *Cell Death and Differentiation*. https://doi.org/10.1038/cdd.2009.193

Barrow, S. L., Constable, J. R., Clark, E., El-Sabeawy, F., McAllister, A. K., & Washbourne, P. (2009). Neuroligin1: A cell adhesion molecule that recruits PSD-95 and NMDA receptors by distinct mechanisms during synaptogenesis. *Neural Development*. https://doi.org/10.1186/1749-8104-4-17

Bats, C., Groc, L., & Choquet, D. (2007). The Interaction between Stargazin and PSD-95 Regulates AMPA Receptor Surface Trafficking. *Neuron*, *53*(5), 719–734. https://doi.org/10.1016/j.neuron.2007.01.030

Bayer, K. U., De Koninck, P., Leonard, A. S., Hell, J. W., & Schulman, H. (2001). Interaction with the NMDA receptor locks CaMKII in an active conformation. *Nature*, *411*(6839), 801–805. https://doi.org/10.1038/35081080

Béïque, J. C., Lin, D. T., Kang, M. G., Aizawa, H., Takamiya, K., & Huganir, R. L. (2006). Synapse-specific regulation of AMPA receptor function by PSD-95. *Proceedings of the National Academy of Sciences of the United States of America*. https://doi.org/10.1073/pnas.0608492103

Bell, M. E., Bourne, J. N., Chirillo, M. A., Mendenhall, J. M., Kuwajima, M., & Harris, K. M. (2014). Dynamics of nascent and active zone ultrastructure as synapses enlarge during long-term potentiation in mature hippocampus. *Journal of Comparative Neurology*. https://doi.org/10.1002/cne.23646

Blanpied, T. A., Kerr, J. M., & Ehlers, M. D. (2008). Structural plasticity with preserved topology in the postsynaptic protein network. *Proceedings of the National Academy of Sciences of the United States of America*. https://doi.org/10.1073/pnas.0711669105

Borczyk, M., Śliwińska, M. A., Caly, A., Bernas, T., & Radwanska, K. (2019). Neuronal plasticity affects correlation between the size of dendritic spine and its postsynaptic density. *Scientific Reports*. https://doi.org/10.1038/s41598-018-38412-7

Borovac, J., Bosch, M., & Okamoto, K. (2018). Regulation of actin dynamics during structural plasticity of dendritic spines: Signaling messengers and actin-binding proteins. *Molecular and Cellular Neuroscience*. https://doi.org/10.1016/j.mcn.2018.07.001

Bosch, M., Castro, J., Saneyoshi, T., Matsuno, H., Sur, M., & Hayashi, Y. (2014). Structural and molecular remodeling of dendritic spine substructures during long-term potentiation. *Neuron*, *82*(2), 444–459. https://doi.org/10.1016/j.neuron.2014.03.021

Bosch, M., & Hayashi, Y. (2012). Structural plasticity of dendritic spines. *Current Opinion in Neurobiology*. https://doi.org/10.1016/j.conb.2011.09.002

Bourne, J. N., Chirillo, M. A., & Harris, K. M. (2013). Presynaptic ultrastructural plasticity along CA3→CA1 axons during long-term potentiation in mature hippocampus. *Journal of Comparative Neurology*. https://doi.org/10.1002/cne.23384

Bourne, J. N., & Harris, K. M. (2011). Coordination of size and number of excitatory and inhibitory synapses results in a balanced structural plasticity along mature hippocampal CA1 dendrites during LTP. *Hippocampus*. https://doi.org/10.1002/hipo.20768

Bourtchuladze, R., Frenguelli, B., Blendy, J., Cioffi, D., Schutz, G., & Silva, A. J. (1994). Deficient long-term memory in mice with a targeted mutation of the cAMP-responsive element-binding protein. *Cell*. https://doi.org/10.1016/0092-8674(94)90400-6

Bozon, B., Davis, S., & Laroche, S. (2003). A requirement for the immediate early gene zif268 in reconsolidation of recognition memory after retrieval. *Neuron*. https://doi.org/10.1016/S0896-6273(03)00674-3

Bredt, D. S., & Nicoll, R. A. (2003). AMPA receptor trafficking at excitatory synapses. *Neuron*. https://doi.org/10.1016/S0896-6273(03)00640-8

Buchs, P. A., & Muller, D. (1996). Induction of long-term potentiation is associated with major ultrastructural changes of activated synapses. *Proceedings of the National Academy of Sciences of the United States of America*. https://doi.org/10.1073/pnas.93.15.8040

Carlisle, H. J., Fink, A. E., Grant, S. G. N., & O'dell, T. J. (2008). Opposing effects of PSD-93 and PSD-95 on long-term potentiation and spike timing-dependent plasticity. *Journal of Physiology*. https://doi.org/10.1113/jphysiol.2008.163469

Chao, L. H., Pellicena, P., Deindl, S., Barclay, L. A., Schulman, H., & Kuriyan, J. (2010). Intersubunit capture of regulatory segments is a component of cooperative CaMKII activation. *Nature Structural and Molecular Biology*. https://doi.org/10.1038/nsmb.1751

Chen, X., Levy, J. M., Hou, A., Winters, C., Azzam, R., Sousa, A. A., … Reese, T. S. (2015). PSD-95 family MAGUKs are essential for anchoring AMPA and NMDA receptor complexes at the postsynaptic density. *Proceedings of the National Academy of Sciences of the United States of America*. https://doi.org/10.1073/pnas.1517045112

Chen, X., Nelson, C. D., Li, X., Winters, C. A., Azzam, R., Sousa, A. A., … Reese, T. S. (2011). PSD-95 is required to sustain the molecular organization of the postsynaptic density. *Journal of Neuroscience*. https://doi.org/10.1523/JNEUROSCI.5968-10.2011

Chih, B., Engelman, H., & Scheiffele, P. (2005). Control of excitatory and inhibitory synapse formation by neuroligins. *Science*. https://doi.org/10.1126/science.1107470

Chirillo, M. A., Waters, M. S., Lindsey, L. F., Bourne, J. N., & Harris, K. M. (2019). Local resources of polyribosomes and SER promote synapse enlargement and spine clustering after long-term potentiation in adult rat hippocampus. *Scientific Reports*. https://doi.org/10.1038/s41598-019-40520-x

Colbert, C. M., & Johnston, D. (1996). Axonal action-potential initiation and Na+ channel densities in the soma and axon initial segment of subicular pyramidal neurons. *Journal of Neuroscience*. https://doi.org/10.1523/jneurosci.16-21-06676.1996

Coley, A. A., & Gao, W. J. (2019). PSD-95 deficiency disrupts PFC-associated function and behavior during neurodevelopment. *Scientific Reports*. https://doi.org/10.1038/s41598-019-45971-w

D'Este, E., Kamin, D., Balzarotti, F., & Hell, S. W. (2017). Ultrastructural anatomy of nodes of Ranvier in the peripheral nervous system as revealed by STED microscopy. *Proceedings of the National Academy of Sciences of the United States of America*. https://doi.org/10.1073/pnas.1619553114

Dani, A., Huang, B., Bergan, J., Dulac, C., & Zhuang, X. (2010). Superresolution Imaging of Chemical Synapses in the Brain. *Neuron*. https://doi.org/10.1016/j.neuron.2010.11.021

Davydova, D., Marini, C., King, C., Klueva, J., Bischof, F., Romorini, S., … Fejtova, A. (2014). Bassoon specifically controls presynaptic P/Q-type Ca2+ channels via RIM-binding protein. *Neuron*. https://doi.org/10.1016/j.neuron.2014.02.012

De Koninck, P., & Schulman, H. (1998). Sensitivity of CaM kinase II to the frequency of Ca2+ oscillations. *Science*. https://doi.org/10.1126/science.279.5348.227

De Robertis, E D and Bennett, H. S. (1955). Some Features of T H E Submicroscopic Morphology of. *The Journal of Biophysical and Biochemical Cytology*.

del Castillo, J., & Katz, B. (1954). Quantal components of the end‐plate potential. *The Journal of Physiology*. https://doi.org/10.1113/jphysiol.1954.sp005129

Deller, T., Korte, M., Chabanis, S., Drakew, A., Schwegler, H., Stefani, G. G., … Mundel, P. (2003). Synaptopodin-deficient mice lack a spine apparatus and show deficits in synaptic plasticity. *Proceedings of the National Academy of Sciences of the United States of America*. https://doi.org/10.1073/pnas.1832384100

Deller, T., Merten, T., Roth, S. U., Mundel, P., & Frotscher, M. (2000). Actin-associated protein synaptopodin in the rat hippocampal formation: Localization in the spine neck and close association with the spine apparatus of principal neurons. *Journal of Comparative Neurology*. https://doi.org/10.1002/(SICI)1096-9861(20000306)418:2<164::AID-CNE4>3.0.CO;2-0

Desmond, N. L., & Levy, W. B. (1986). Changes in the postsynaptic density with long‐term potentiation in the dentate gyrus. *Journal of Comparative Neurology*. https://doi.org/10.1002/cne.902530405

Dieterich, D. C., & Kreutz, M. R. (2016). Proteomics of the synapse - A quantitative approach to neuronal plasticity. *Molecular and Cellular Proteomics*. https://doi.org/10.1074/mcp.R115.051482

Dingledine, R., Borges, K., Bowie, D., & Traynelis, S. F. (1999). The glutamate receptor ion channels. *Pharmacological Reviews*.

Djinović-Carugo, K., Young, P., Gautel, M., & Saraste, M. (1999). Structure of the α-actinin rod: Molecular basis for cross-linking of actin filaments. *Cell*. https://doi.org/10.1016/S0092-8674(00)81981-9

Dulubova, I., Lou, X., Lu, J., Huryeva, I., Alam, A., Schneggenburger, R., … Rizo, J. (2005). A Munc13/RIM/Rab3 tripartite complex: From priming to plasticity? *EMBO Journal*. https://doi.org/10.1038/sj.emboj.7600753

Eggeling, C., Willig, K. I., Sahl, S. J., & Hell, S. W. (2015). Lens-based fluorescence nanoscopy. *Quarterly Reviews of Biophysics*. https://doi.org/10.1017/S0033583514000146

Ehrlich, I., Klein, M., Rumpel, S., & Malinow, R. (2007). PSD-95 is required for activity-driven synapse stabilization. *Proceedings of the National Academy of Sciences of the United States of America*. https://doi.org/10.1073/pnas.0609307104

Elias, G. M., Funke, L., Stein, V., Grant, S. G., Bredt, D. S., & Nicoll, R. A. (2006). Synapse-Specific and Developmentally Regulated Targeting of AMPA Receptors by a Family of MAGUK Scaffolding Proteins. *Neuron*. https://doi.org/10.1016/j.neuron.2006.09.012

Elliot, L. S., Dudai, Y., Kandel, E. R., & Abrams, T. W. (1989). Ca2+/calmodulin sensitivity may be common to all forms of neural adenylate cyclase. *Proceedings of the National Academy of Sciences of the United States of America*. https://doi.org/10.1073/pnas.86.23.9564

Falzone, T. T., Lenz, M., Kovar, D. R., & Gardel, M. L. (2012). Assembly kinetics determine the architecture of α-actinin crosslinked F-actin networks. *Nature Communications*. https://doi.org/10.1038/ncomms1862

Fatt, P., & Katz, B. (1951). An analysis of the end‐plate potential recorded with an intra‐cellular electrode. *The Journal of Physiology*. https://doi.org/10.1113/jphysiol.1951.sp004675

Fejtova, A., Schmidt, H., Weyhersmüller, A., Silver, R. A., Gundelfinger, E. D., & Eilers, J. (2010). Bassoon speeds vesicle reloading at a central excitatory synapse. *Neuron*. https://doi.org/10.1016/j.neuron.2010.10.026

Fifková, E., Markham, J. A., & Delay, R. J. (1983). Calcium in the spine apparatus of dendritic spines in the dentate molecular layer. *Brain Research*. https://doi.org/10.1016/0006-8993(83)91322-7

Frey, U., Huang, Y. Y., & Kandel, E. R. (1993). Effects of cAMP simulate a late stage of LTP in hippocampal CA1 neurons. *Science*. https://doi.org/10.1126/science.8389057

Friedman, H. V., Bresler, T., Garner, C. C., & Ziv, N. E. (2000). Assembly of new individual excitatory synapses: Time course and temporal order of synaptic molecule recruitment. *Neuron*. https://doi.org/10.1016/S0896-6273(00)00009-X

Fukata, Y., Dimitrov, A., Boncompain, G., Vielemeyer, O., Perez, F., & Fukata, M. (2013). Local palmitoylation cycles define activity-regulated postsynaptic subdomains. *Journal of Cell Biology*. https://doi.org/10.1083/jcb.201302071

Funke, L., Dakoji, S., & Bredt, D. S. (2005). Membrane-associated guanylate kinases regulate adhesion and plasticity at cell junctions. *Annual Review of Biochemistry*. https://doi.org/10.1146/annurev.biochem.74.082803.133339

Futai, K., Kim, M. J., Hashikawa, T., Scheiffele, P., Sheng, M., & Hayashi, Y. (2007). Retrograde modulation of presynaptic release probability through signaling mediated by PSD-95-neuroligin. *Nature Neuroscience*. https://doi.org/10.1038/nn1837

Ganeshina, O., Berry, R. W., Petralia, R. S., Nicholson, D. A., & Geinisman, Y. (2004). Differences in the Expression of AMPA and NMDA Receptors between Axospinous Perforated and Nonperforated Synapses Are Related to the Configuration and Size of Postsynaptic Densities. *Journal of Comparative Neurology*. https://doi.org/10.1002/cne.10950

Gerrow, K., Romorini, S., Nabi, S. M., Colicos, M. A., Sala, C., & El-Husseini, A. (2006). A preformed complex of postsynaptic proteins is involved in excitatory synapse development. *Neuron*. https://doi.org/10.1016/j.neuron.2006.01.015

Giannone, G., Mondin, M., Grillo-Bosch, D., Tessier, B., Saint-Michel, E., Czöndör, K., … Thoumine, O. (2013). Neurexin-1β Binding to Neuroligin-1 Triggers the Preferential Recruitment of PSD-95 versus Gephyrin through Tyrosine Phosphorylation of Neuroligin-1. *Cell Reports*. https://doi.org/10.1016/j.celrep.2013.05.013

Giese, K. P., Fedorov, N. B., Filipkowski, R. K., & Silva, A. J. (1998). Autophosphorylation at Thr286 of the α calcium-calmodulin kinase II in LTP and learning. *Science*, *279*(5352), 870–873. https://doi.org/10.1126/science.279.5352.870

Glasgow, S. D., McPhedrain, R., Madranges, J. F., Kennedy, T. E., & Ruthazer, E. S. (2019). Approaches and limitations in the investigation of synaptic transmission and plasticity. *Frontiers in Synaptic Neuroscience*. https://doi.org/10.3389/fnsyn.2019.00020

Golding, N. L., & Spruston, N. (1998). Dendritic sodium spikes are variable triggers of axonal action potentials in hippocampal CA1 pyramidal neurons. *Neuron*. https://doi.org/10.1016/S0896-6273(00)80635-2

Gomperts, S. N., Rao, A., Craig, A. M., Malenka, R. C., & Nicoll, R. A. (1998). Postsynaptically silent synapses in single neuron cultures. *Neuron*. https://doi.org/10.1016/S0896-6273(00)80662-5

Graf, E. R., Zhang, X., Jin, S. X., Linhoff, M. W., & Craig, A. M. (2004). Neurexins induce differentiation of GABA and glutamate postsynaptic specializations via neuroligins. *Cell*. https://doi.org/10.1016/j.cell.2004.11.035

GRAY, E. G. (1959). Axo-somatic and axo-dendritic synapses of the cerebral cortex: an electron microscope study. *Journal of Anatomy*.

Greifzu, F., Kalogeraki, E., & Löwel, S. (2016). Environmental enrichment preserved lifelong ocular dominance plasticity, but did not improve visual abilities. *Neurobiology of Aging*, *41*, 130–137. https://doi.org/10.1016/j.neurobiolaging.2016.02.014

Grooms, S. Y., Noh, K. M., Regis, R., Bassell, G. J., Bryan, M. K., Carroll, R. C., & Zukin, R. S. (2006). Activity bidirectionally regulates AMPA receptor mRNA abundance in dendrites of hippocampal neurons. *Journal of Neuroscience*. https://doi.org/10.1523/JNEUROSCI.0472-06.2006

Gross, G. G., Junge, J. A., Mora, R. J., Kwon, H. B., Olson, C. A., Takahashi, T. T., … Arnold, D. B. (2013). Recombinant Probes for Visualizing Endogenous Synaptic Proteins in Living Neurons. *Neuron*, *78*(6), 971–985. https://doi.org/10.1016/j.neuron.2013.04.017

Grotjohann, T., Testa, I., Reuss, M., Brakemann, T., Eggeling, C., Hell, S. W., & Jakobs, S. (2012). rsEGFP2 enables fast RESOLFT nanoscopy of living cells. *ELife*. https://doi.org/10.7554/eLife.00248

Gundelfinger, E. D., Reissner, C., & Garner, C. C. (2016). Role of Bassoon and Piccolo in Assembly and Molecular Organization of the Active Zone. *Frontiers in Synaptic Neuroscience*. https://doi.org/10.3389/fnsyn.2015.00019

Haas, K. T., Compans, B., Letellier, M., Bartol, T. M., Grillo-Bosch, D., Sejnowski, T. J., … Hosy, E. (2018). Pre-post synaptic alignment through neuroligin-1 tunes synaptic transmission efficiency. *ELife*. https://doi.org/10.7554/eLife.31755

Hafner, A. S., Penn, A. C., Grillo-Bosch, D., Retailleau, N., Poujol, C., Philippat, A., … Choquet, D. (2015). Lengthening of the stargazin cytoplasmic tail increases synaptic transmission by promoting interaction to deeper domains of PSD-95. *Neuron*. https://doi.org/10.1016/j.neuron.2015.03.013

Harris, K. M., Jensen, F. E., & Tsao, B. (1992). Three-dimensional structure of dendritic spines and synapses in rat hippocampus (CA 1) at postnatal day 15 and adult ages: Implications for the maturation of synaptic physiology and long-term potentiation. *Journal of Neuroscience*. https://doi.org/10.1523/jneurosci.12-07-02685.1992

Harris, K. M., & Stevens, J. K. (1989). Dendritic spines of CA1 pyramidal cells in the rat hippocampus: Serial electron microscopy with reference to their biophysical characteristics. *Journal of Neuroscience*. https://doi.org/10.1523/jneurosci.09-08-02982.1989

Hartzell, H. C. (1981). Mechanisms of slow postsynaptic potentials. *Nature*. https://doi.org/10.1038/291539a0

Hazan, L., & Ziv, N. E. (2020). Activity dependent and independent determinants of synaptic size diversity. *Journal of Neuroscience*. https://doi.org/10.1523/JNEUROSCI.2181-19.2020

Hebb, D. O. (1949). Organization of behavior. (New York: John Wiley and Sons). *Journal of Clinical Psychology*.

Hell, S. W., & Wichmann, J. (1994). Breaking the diffraction resolution limit by stimulated emission: stimulated-emission-depletion fluorescence microscopy. *Optics Letters*. https://doi.org/10.1364/ol.19.000780

Henley, J. M., & Wilkinson, K. A. (2013). AMPA receptor trafficking and the mechanisms underlying synaptic plasticity and cognitive aging. *Dialogues in Clinical Neuroscience*. https://doi.org/10.31887/dcns.2013.15.1/jhenley

Henson, M. A., Roberts, A. C., Pérez-Otaño, I., & Philpot, B. D. (2010). Influence of the NR3A subunit on NMDA receptor functions. *Progress in Neurobiology*. https://doi.org/10.1016/j.pneurobio.2010.01.004

Herring, B. E., & Nicoll, R. A. (2016). Long-Term Potentiation: From CaMKII to AMPA Receptor Trafficking. *Annual Review of Physiology*. https://doi.org/10.1146/annurev-physiol-021014-071753

Holt, M. (2017). Satnav for cells: Destination membrane fusion. *Cell Calcium*. https://doi.org/10.1016/j.ceca.2017.10.001

Holtmaat, A. J. G. D., Trachtenberg, J. T., Wilbrecht, L., Shepherd, G. M., Zhang, X., Knott, G. W., & Svoboda, K. (2005). Transient and persistent dendritic spines in the neocortex in vivo. *Neuron*. https://doi.org/10.1016/j.neuron.2005.01.003

Holtmaat, A., Wilbrecht, L., Knott, G. W., Welker, E., & Svoboda, K. (2006). Experience-dependent and cell-type-specific spine growth in the neocortex. *Nature*. https://doi.org/10.1038/nature04783

Honkura, N., Matsuzaki, M., Noguchi, J., Ellis-Davies, G. C. R., & Kasai, H. (2008). The Subspine Organization of Actin Fibers Regulates the Structure and Plasticity of Dendritic Spines. *Neuron*. https://doi.org/10.1016/j.neuron.2008.01.013

Hruska, M., Henderson, N., Le Marchand, S. J., Jafri, H., & Dalva, M. B. (2018). Synaptic nanomodules underlie the organization and plasticity of spine synapses. *Nature Neuroscience*. https://doi.org/10.1038/s41593-018-0138-9

Ifrim, M. F., Williams, K. R., & Bassell, G. J. (2015). Single-molecule imaging of PSD-95 mRNA translation in dendrites and its dysregulation in a mouse model of fragile X syndrome. *Journal of Neuroscience*. https://doi.org/10.1523/JNEUROSCI.2802-14.2015

Irie, M., Hata, Y., Takeuchi, M., Ichtchenko, K., Toyoda, A., Hirao, K., … Südhof, T. C. (1997). Binding of neuroligins to PSD-95. *Science*. https://doi.org/10.1126/science.277.5331.1511

Iwasaki, H., Tanaka, S., & Okabe, S. (2016). Molecular assembly of excitatory synapses. In *Dendrites: Development and Disease*. https://doi.org/10.1007/978-4-431-56050-0_15

Izquierdo, I., & Medina, J. H. (1997). Memory formation: The sequence of biochemical events in the hippocampus and its connection to activity in other brain structures. *Neurobiology of Learning and Memory*. https://doi.org/10.1006/nlme.1997.3799

Jake F. Watson, Alexandra Pinggera, Hinze Ho, I. H. G. (2020a). AMPA receptor anchoring at CA1 synapses is determined by an interplay of N-terminal domain and TARP γ8 Jake F. Watson, Alexandra Pinggera, Hinze Ho, Ingo H. Gregerinteractions. *BioRxiv Preprint*. https://doi.org/https://doi.org/10.1101/2020.07.09.196154

Jake F. Watson, Alexandra Pinggera, Hinze Ho, I. H. G. (2020b). AMPA receptor anchoring at CA1 synapses is determined by an interplay of N-terminal domain and TARP γ8 Jake F. Watson, Alexandra Pinggera, Hinze Ho, Ingo H. Gregerinteractions. *Biorxiv*. https://doi.org/https://doi.org/10.1101/2020.07.09.196154

James, A. B., Conway, A. M., & Morris, B. J. (2005). Genomic profiling of the neuronal target genes of the plasticity-related transcription factor - Zif268. *Journal of Neurochemistry*. https://doi.org/10.1111/j.1471-4159.2005.03400.x

Jones, M. W., Errington, M. L., French, P. J., Fine, A., Bliss, T. V. P., Garel, S., … Davis, S. (2001). A requirement for the immediate early gene Zif268 in the expression of late LTP and long-term memories. *Nature Neuroscience*. https://doi.org/10.1038/85138

Kameda, H., Furuta, T., Matsuda, W., Ohira, K., Nakamura, K., Hioki, H., & Kaneko, T. (2008). Targeting green fluorescent protein to dendritic membrane in central neurons. *Neuroscience Research*. https://doi.org/10.1016/j.neures.2008.01.014

Kennedy, M. B. (2016). Synaptic signaling in learning and memory. *Cold Spring Harbor Perspectives in Biology*. https://doi.org/10.1101/cshperspect.a016824

Kerchner, G. A., & Nicoll, R. A. (2008). Silent synapses and the emergence of a postsynaptic mechanism for LTP. *Nature Reviews Neuroscience*. https://doi.org/10.1038/nrn2501

Kim, C. H., & Lisman, J. E. (1999). A role of actin filament in synaptic transmission and long-term potentiation. *Journal of Neuroscience*. https://doi.org/10.1523/jneurosci.19-11-04314.1999

Kim, E., Naisbitt, S., Hsueh, Y. P., Rao, A., Rothschild, A., Craig, A. M., & Sheng, M. (1997). GKAP, a novel synaptic protein that interacts with the guanylate kinase- like domain of the PSD-95/SAP90 family of channel clustering molecules. *Journal of Cell Biology*. https://doi.org/10.1083/jcb.136.3.669

Kim, E., & Sheng, M. (2004). PDZ domain proteins of synapses. *Nature Reviews Neuroscience*. https://doi.org/10.1038/nrn1517

Kim, J., Jo, H., Hong, H., Kim, M. H., Kim, J. M., Lee, J. K., … Kim, J. (2015). Actin remodelling factors control ciliogenesis by regulating YAP/TAZ activity and vesicle trafficking. *Nature Communications*. https://doi.org/10.1038/ncomms7781

Kopec, C. D., Li, B., Wei, W., Boehm, J., & Malinow, R. (2006). Glutamate receptor exocytosis and spine enlargement during chemically induced long-term potentiation. *Journal of Neuroscience*. https://doi.org/10.1523/JNEUROSCI.3918-05.2006

Kornau, H. C., Schenker, L. T., Kennedy, M. B., & Seeburg, P. H. (1995). Domain interaction between NMDA receptor subunits and the postsynaptic density protein PSD-95. *Science*. https://doi.org/10.1126/science.7569905

Kristensen, A. S., Jenkins, M. A., Banke, T. G., Schousboe, A., Makino, Y., Johnson, R. C., … Traynelis, S. F. (2011). Mechanism of Ca2+/calmodulin-dependent kinase II regulation of AMPA receptor gating. *Nature Neuroscience*, *14*(6), 727–735. https://doi.org/10.1038/nn.2804

Kuner, T., Wollmuth, L. P., Karlin, A., Seeburg, P. H., & Sakmann, B. (1996). Structure of the NMDA receptor channel M2 segment inferred from the accessibility of substituted cysteines. *Neuron*. https://doi.org/10.1016/S0896-6273(00)80165-8

Kuriu, T., Inoue, A., Bito, H., Sobue, K., & Okabe, S. (2006). Differential control of postsynaptic density scaffolds via actin-dependent and -independent mechanisms. *Journal of Neuroscience*. https://doi.org/10.1523/JNEUROSCI.0522-06.2006

Laube, B., Hirai, H., Sturgess, M., Betz, H., & Kuhse, J. (1997). Molecular determinants of agonist discrimination by NMDA receptor subunits: Analysis of the glutamate binding site on the NR2B subunit. *Neuron*. https://doi.org/10.1016/S0896-6273(00)81249-0

Lavenex, P., & Amaral, D. G. (2000). Hippocampal-neocortical interaction: A hierarchy of associativity. *Hippocampus*. https://doi.org/10.1002/1098-1063(2000)10:4<420::AID-HIPO8>3.0.CO;2-5

Lee, H. K., Barbarosie, M., Kameyama, K., Bear, M. F., & Huganir, R. L. (2000). Regulation of distinct AMPA receptor phosphorylation sites during bidirectional synaptic plasticity. *Nature*. https://doi.org/10.1038/35016089

Li, Y., Mu, Y., & Gage, F. H. (2009). Chapter 5 Development of Neural Circuits in the Adult Hippocampus. *Current Topics in Developmental Biology*. https://doi.org/10.1016/S0070-2153(09)01205-8

Lim, I. A., Hall, D. D., & Hell, J. W. (2002). Selectivity and promiscuity of the first and second PDZ domains of PSD-95 and synapse-associated protein 102. *Journal of Biological Chemistry*. https://doi.org/10.1074/jbc.M112339200

Lin, Y., Skeberdis, V. A., Francesconi, A., Bennett, M. V. L., & Zukin, R. S. (2004). Postsynaptic density protein-95 regulates NMDA channel gating and surface expression. *Journal of Neuroscience*. https://doi.org/10.1523/JNEUROSCI.3159-04.2004

Lisman, J., & Raghavachari, S. (2006). A unified model of the presynaptic and postsynaptic changes during LTP at CA1 synapses. *Science's STKE : Signal Transduction Knowledge Environment*. https://doi.org/10.1126/stke.3562006re11

Lisman, J., & Raghavachari, S. (2015). Biochemical principles underlying the stable maintenance of LTP by the CaMKII/NMDAR complex. *Brain Research*. https://doi.org/10.1016/j.brainres.2014.12.010

Lomo, T. (1966). Frequency Potentiation of Excitatory Synaptic Activity in the Dentate Area of the Hippocampal Formation. *Acta Physiol. Scand*.

Low, C. M., & Wee, K. S. L. (2010). New insights into the not-so-new NR3 subunits of N-methyl-D-aspartate receptor: Localization, structure, and function. *Molecular Pharmacology*. https://doi.org/10.1124/mol.110.064006

Lu, W., Shi, Y., Jackson, A. C., Bjorgan, K., During, M. J., Sprengel, R., … Nicoll, R. A. (2009). Subunit Composition of Synaptic AMPA Receptors Revealed by a Single-Cell Genetic Approach. *Neuron*. https://doi.org/10.1016/j.neuron.2009.02.027

Lu, W. Y., Man, H. Y., Ju, W., Trimble, W. S., MacDonald, J. F., & Wang, Y. T. (2001). Activation of synaptic NMDA receptors induces membrane insertion of new AMPA receptors and LTP in cultured hippocampal neurons. *Neuron*. https://doi.org/10.1016/S0896-6273(01)00194-5

Lucchesi, W., Mizuno, K., & Giese, K. P. (2011). Novel insights into CaMKII function and regulation during memory formation. *Brain Research Bulletin*. https://doi.org/10.1016/j.brainresbull.2010.10.009

MacGillavry, H. D., Song, Y., Raghavachari, S., & Blanpied, T. A. (2013). Nanoscale scaffolding domains within the postsynaptic density concentrate synaptic ampa receptors. *Neuron*. https://doi.org/10.1016/j.neuron.2013.03.009

Mammen, A. L., Kameyama, K., Roche, K. W., & Huganir, R. L. (1997). Phosphorylation of the α-amino-3-hydroxy-5-methylisoxazole-4-propionic Acid receptor GluR1 subunit by calcium/calmodulin-dependent kinase II. *Journal of Biological Chemistry*. https://doi.org/10.1074/jbc.272.51.32528

Masch, J. M., Steffens, H., Fischer, J., Engelhardt, J., Hubrich, J., Keller-Findeisen, J., … Hell, S. W. (2018). Robust nanoscopy of a synaptic protein in living mice by organic-fluorophore labeling. *Proceedings of the National Academy of Sciences of the United States of America*. https://doi.org/10.1073/pnas.1807104115

Matsuzaki, M., Ellis-Davies, G. C. R., Nemoto, T., Miyashita, Y., Iino, M., & Kasai, H. (2001). Dendritic spine geometry is critical for AMPA receptor expression in hippocampal CA1 pyramidal neurons. *Nature Neuroscience*. https://doi.org/10.1038/nn736

Matsuzaki, M., Honkura, N., Ellis-Davies, G. C. R., & Kasai, H. (2004). Structural basis of long-term potentiation in single dendritic spines. *Nature*. https://doi.org/10.1038/nature02617

Matt, L., Kim, K., Hergarden, A. C., Patriarchi, T., Malik, Z. A., Park, D. K., … Hell, J. W. (2018). α-Actinin Anchors PSD-95 at Postsynaptic Sites. *Neuron*. https://doi.org/10.1016/j.neuron.2018.01.036

Mayford, M., Bach, M. E., Huang, Y. Y., Wang, L., Hawkins, R. D., & Kandel, E. R. (1996). Control of memory formation through regulated expression of a CaMKII transgene. *Science*. https://doi.org/10.1126/science.274.5293.1678

Meguro, H., Mori, H., Araki, K., Kushiya, E., Kutsuwada, T., Yamazaki, M., … Mishina, M. (1992). Functional characterization of a heteromeric NMDA receptor channel expressed from cloned cDNAs. *Nature*. https://doi.org/10.1038/357070a0

Meyer, D., Bonhoeffer, T., & Scheuss, V. (2014). Balance and stability of synaptic structures during synaptic plasticity. *Neuron*. https://doi.org/10.1016/j.neuron.2014.02.031

Miller, S. G., & Kennedy, M. B. (1986). Regulation of brain Type II Ca2+ calmodulin-dependent protein kinase by autophosphorylation: A Ca2+-triggered molecular switch. *Cell*. https://doi.org/10.1016/0092-8674(86)90008-5

Molnár, E. (2011). Long-term potentiation in cultured hippocampal neurons. *Seminars in Cell and Developmental Biology*. https://doi.org/10.1016/j.semcdb.2011.07.017

Monyer, H., Sprengel, R., Schoepfer, R., Herb, A., Higuchi, M., Lomeli, H., … Seeburg, P. H. (1992). Heteromeric NMDA receptors: Molecular and functional distinction of subtypes. *Science*. https://doi.org/10.1126/science.256.5060.1217

Mukherjee, K., Yang, X., Gerber, S. H., Kwon, H. B., Ho, A., Castillo, P. E., … Südhof, T. C. (2010). Piccolo and bassoon maintain synaptic vesicle clustering without directly participating in vesicle exocytosis. *Proceedings of the National Academy of Sciences of the United States of America*. https://doi.org/10.1073/pnas.1002307107

Nagatsu, T., Mogi, M., Ichinose, H., & Togari, A. (2000). Cytokines in Parkinson's disease. In *Journal of Neural Transmission, Supplement*. https://doi.org/10.1007/978-3-7091-6284-2_12

Nair, D., Hosy, E., Petersen, J. D., Constals, A., Giannone, G., Choquet, D., & Sibarita, J. B. (2013). Super-resolution imaging reveals that AMPA receptors inside synapses are dynamically organized in nanodomains regulated by PSD95. *Journal of Neuroscience*. https://doi.org/10.1523/JNEUROSCI.2381-12.2013

Naisbitt, S., Eunjoon, K., Tu, J. C., Xiao, B., Sala, C., Valtschanoff, J., … Sheng, M. (1999). Shank, a novel family of postsynaptic density proteins that binds to the NMDA receptor/PSD-95/GKAP complex and cortactin. *Neuron*. https://doi.org/10.1016/S0896-6273(00)80809-0

Nam, C. I., & Chen, L. (2005). Postsynaptic assembly induced by neurexin-neuroligin interaction and neurotransmitter. *Proceedings of the National Academy of Sciences of the United States of America*. https://doi.org/10.1073/pnas.0502038102

Nguyen, P. V., & Woo, N. H. (2003). Regulation of hippocampal synaptic plasticity by cyclic AMP-dependent protein kinases. *Progress in Neurobiology*. https://doi.org/10.1016/j.pneurobio.2003.12.003

Nikonenko, I., Boda, B., Steen, S., Knott, G., Welker, E., & Muller, D. (2008). PSD-95 promotes synaptogenesis and multiinnervated spine formation through nitric oxide signaling. *Journal of Cell Biology*. https://doi.org/10.1083/jcb.200805132

O'Keefe, J., & Dostrovsky, J. (1971). The hippocampus as a spatial map. Preliminary evidence from unit activity in the freely-moving rat. *Brain Research*. https://doi.org/10.1016/0006-8993(71)90358-1

Okamoto, K., Bosch, M., & Hayashi, Y. (2009). The roles of CaMKII and F-Actin in the structural plasticity of dendritic Spines: A potential molecular identity of a synaptic tag? *Physiology*. https://doi.org/10.1152/physiol.00029.2009

Opazo, P., Labrecque, S., Tigaret, C. M., Frouin, A., Wiseman, P. W., De Koninck, P., & Choquet, D. (2010). CaMKII triggers the diffusional trapping of surface AMPARs through phosphorylation of stargazin. *Neuron*, *67*(2), 239–252. https://doi.org/10.1016/j.neuron.2010.06.007

Opazo, P., Sainlos, M., & Choquet, D. (2012). Regulation of AMPA receptor surface diffusion by PSD-95 slots. *Current Opinion in Neurobiology*. https://doi.org/10.1016/j.conb.2011.10.010

Ostroff, L. E., Botsford, B., Gindina, S., Cowansage, K. K., Ledoux, J. E., Klann, E., & Hoeffer, C. (2017). Accumulation of polyribosomes in dendritic spine heads, but not bases and necks, during memory consolidation depends on cap-dependent translation initiation. *Journal of Neuroscience*. https://doi.org/10.1523/JNEUROSCI.3301-16.2017

Ostroff, L. E., Fiala, J. C., Allwardt, B., & Harris, K. M. (2002). Polyribosomes redistribute from dendritic shafts into spines with enlarged synapses during LTP in developing rat hippocampal slices. *Neuron*. https://doi.org/10.1016/S0896-6273(02)00785-7

PALAY, S. L. (1956). Synapses in the central nervous system. *The Journal of Biophysical and Biochemical Cytology*. https://doi.org/10.1083/jcb.2.4.193

Panatier, A., Theodosis, D. T., Mothet, J. P., Touquet, B., Pollegioni, L., Poulain, D. A., & Oliet, S. H. R. (2006). Glia-Derived d-Serine Controls NMDA Receptor Activity and Synaptic Memory. *Cell*. https://doi.org/10.1016/j.cell.2006.02.051

Patterson, M. A., Szatmari, E. M., & Yasuda, R. (2010). AMPA receptors are exocytosed in stimulated spines and adjacent dendrites in a Ras-ERK-dependent manner during long-term potentiation. *Proceedings of the National Academy of Sciences of the United States of America*. https://doi.org/10.1073/pnas.0913875107

Penzes, P., Johnson, R. C., Kambampati, V., Mains, R. E., & Eipper, B. A. (2001). Distinct roles for the two Rho GDP/GTP exchange factor domains of Kalirin in regulation of neurite growth and neuronal morphology. *Journal of Neuroscience*. https://doi.org/10.1523/jneurosci.21-21-08426.2001

Pi, H. J., Otmakhov, N., El Gaamouch, F., Lemelin, D., De Koninck, P., & Lisman, J. (2010). CaMKII control of spine size and synaptic strength: Role of phosphorylation states and nonenzymatic action. *Proceedings of the National Academy of Sciences of the United States of America*. https://doi.org/10.1073/pnas.1009268107

Pierce, J. P., Van Leyen, K., & McCarthy, J. B. (2000). Translocation machinery for synthesis of integral membrane and secretory proteins in dendritic spines. *Nature Neuroscience*. https://doi.org/10.1038/73868

Plant, K., Pelkey, K. A., Bortolotto, Z. A., Morita, D., Terashima, A., McBain, C. J., … Isaac, J. T. R. (2006). Transient incorporation of native GluR2-lacking AMPA receptors during hippocampal long-term potentiation. *Nature Neuroscience*. https://doi.org/10.1038/nn1678

Popov, V. I., Davies, H. A., Rogachevsky, V. V., Patrushev, I. V., Errington, M. L., Gabbott, P. L. A., … Stewart, M. G. (2004). Remodelling of synaptic morphology but unchanged synaptic density during late phase long-term potentiation (LTP): A serial section electron micrograph study in the dentate gyrus in the anaesthetised rat. *Neuroscience*. https://doi.org/10.1016/j.neuroscience.2004.06.029

Prybylowski, K., Chang, K., Sans, N., Kan, L., Vicini, S., & Wenthold, R. J. (2005). The synaptic localization of NR2B-containing NMDA receptors is controlled by interactions with PDZ proteins and AP-2. *Neuron*. https://doi.org/10.1016/j.neuron.2005.08.016

Raghavachari, S., & Lisman, J. E. (2004). Properties of quantal transmission at CA1 synapses. *Journal of Neurophysiology*. https://doi.org/10.1152/jn.00258.2004

Ramón, M., & Cajal, J. (1934). Histología del sistema nervioso del hombre y de los vertebrados. *CSIC - CSIC Press*.

Rey, S., Marra, V., Smith, C., & Staras, K. (2020). Nanoscale Remodeling of Functional Synaptic Vesicle Pools in Hebbian Plasticity. *Cell Reports*. https://doi.org/10.1016/j.celrep.2020.01.051

Richardson, L. V., & Richardson, J. P. (1992). Cytosine nucleoside inhibition of the ATPase of Escherichia coli termination factor rho: Evidence for a base specific interaction between rho and RNA. *Nucleic Acids Research*. https://doi.org/10.1093/nar/20.20.5383

Richter, K. N., Revelo, N. H., Seitz, K. J., Helm, M. S., Sarkar, D., Saleeb, R. S., … Rizzoli, S. O. (2018). Glyoxal as an alternative fixative to formaldehyde in immunostaining and super‐resolution microscopy. *The EMBO Journal*. https://doi.org/10.15252/embj.201695709

Rizzoli, S. O., & Betz, W. J. (2005). Synaptic vesicle pools. *Nature Reviews Neuroscience*. https://doi.org/10.1038/nrn1583

Roche, K. W., Standley, S., McCallum, J., Dune Ly, C., Ehlers, M. D., & Wenthold, R. J. (2001). Molecular determinants of NMDA receptor internalization. *Nature Neuroscience*. https://doi.org/10.1038/90498

Rosenmund, C., Stern-Bach, Y., & Stevens, C. F. (1998). The tetrameric structure of a glutamate receptor channel. *Science*. https://doi.org/10.1126/science.280.5369.1596

Sacktor, T. C. (2011). How does PKM¶ maintain long-term memory? *Nature Reviews Neuroscience*. https://doi.org/10.1038/nrn2949

Santamaria, F., Gonzalez, J., Augustine, G. J., & Raghavachari, S. (2010). Quantifying the effects of elastic collisions and non-covalent binding on glutamate receptor trafficking in the post-synaptic density. *PLoS Computational Biology*. https://doi.org/10.1371/journal.pcbi.1000780

Scannevin, R. H., & Huganir, R. L. (2000). Postsynaptic organisation and regulation of excitatory synapses. *Nature Reviews Neuroscience*. https://doi.org/10.1038/35039075

Scheefhals, N., & MacGillavry, H. D. (2018). Functional organization of postsynaptic glutamate receptors. *Molecular and Cellular Neuroscience*. https://doi.org/10.1016/j.mcn.2018.05.002

Schikorski, T., & Stevens, C. F. (1999). Quantitative fine-structural analysis of olfactory cortical synapses. *Proceedings of the National Academy of Sciences of the United States of America*. https://doi.org/10.1073/pnas.96.7.4107

Schikorski, Thomas, & Stevens, C. F. (1997). Quantitative ultrastructural analysis of hippocampal excitatory synapses. *Journal of Neuroscience*. https://doi.org/10.1523/jneurosci.17-15-05858.1997

Schlüter, O. M., Xu, W., & Malenka, R. C. (2006). Alternative N-Terminal Domains of PSD-95 and SAP97 Govern Activity-Dependent Regulation of Synaptic AMPA Receptor Function. *Neuron*. https://doi.org/10.1016/j.neuron.2006.05.016

Schneggenburger, R. (1996). Simultaneous measurement of Ca2+ influx and reversal potentials in recombinant N-methyl-D-aspartate receptor channels. *Biophysical Journal*. https://doi.org/10.1016/S0006-3495(96)79782-5

Schnell, E., Sizemore, M., Karimzadegan, S., Chen, L., Bredt, D. S., & Nicoll, R. A. (2002). Direct interactions between PSD-95 and stargazin control synaptic AMPA receptor number. *Proceedings of the National Academy of Sciences of the United States of America*. https://doi.org/10.1073/pnas.172511199

Sheng, M., & Kim, E. (2011). The postsynaptic organization of synapses. *Cold Spring Harbor Perspectives in Biology*. https://doi.org/10.1101/cshperspect.a005678

Sheng, M., & Kim, M. J. (2002). Postsynaptic signaling and plasticity mechanisms. *Science*. https://doi.org/10.1126/science.1075333

Shin, O. H., Xu, J., Rizo, J., & Südhof, T. C. (2009). Differential but convergent functions of Ca2+ binding to synaptotagmin-1 C2 domains mediate neurotransmitter release. *Proceedings of the National Academy of Sciences of the United States of America*. https://doi.org/10.1073/pnas.0908798106

Shomar, A., Geyrhofer, L., Ziv, N. E., & Brenner, N. (2017). Cooperative stochastic binding and unbinding explain synaptic size dynamics and statistics. *PLoS Computational Biology*. https://doi.org/10.1371/journal.pcbi.1005668

Sjöblom, B., Salmazo, A., & Djinović-Carugo, K. (2008). α-Actinin structure and regulation. *Cellular and Molecular Life Sciences*. https://doi.org/10.1007/s00018-008-8080-8

Spacek, J., & Harris, K. M. (1997). Three-dimensional organization of smooth endoplasmic reticulum in hippocampal CA1 dendrites and dendritic spines of the immature and mature rat. *Journal of Neuroscience*. https://doi.org/10.1523/jneurosci.17-01-00190.1997

Squire, L. R. (1992). Memory and the Hippocampuss: A Synthesis From Findings With Rats, Monkeys, and Humans. *Psychological Review*. https://doi.org/10.1037/0033-295X.99.2.195

Statman, A., Kaufman, M., Minerbi, A., Ziv, N. E., & Brenner, N. (2014). Synaptic Size Dynamics as an Effectively Stochastic Process. *PLoS Computational Biology*. https://doi.org/10.1371/journal.pcbi.1003846

Stern, P., Behe, P., Schoepfer, R., & Colquhoun, D. (1992). Single-channel conductances of NMDA receptors expressed from cloned cDNAs: Comparison with native receptors. *Proceedings of the Royal Society B: Biological Sciences*. https://doi.org/10.1098/rspb.1992.0159

Stewart, M. G., Medvedev, N. I., Popov, V. I., Schoepfer, R., Davies, H. A., Murphy, K., … Rodríguez, J. J. (2005). Chemically induced long-term potentiation increases the number of perforated and complex postsynaptic densities but does not alter dendritic spine volume in CA1 of adult mouse hippocampal slices. *European Journal of Neuroscience*. https://doi.org/10.1111/j.1460-9568.2005.04174.x

Stoppini, L., Buchs, P. A., & Muller, D. (1991). A simple method for organotypic cultures of nervous tissue. *Journal of Neuroscience Methods*. https://doi.org/10.1016/0165-0270(91)90128-M

Südhof, T. C. (2012). The presynaptic active zone. *Neuron*. https://doi.org/10.1016/j.neuron.2012.06.012

Südhof, T. C., & Rizo, J. (2011). Synaptic vesicle exocytosis. *Cold Spring Harbor Perspectives in Biology*. https://doi.org/10.1101/cshperspect.a005637

Sutton, M. A., & Schuman, E. M. (2006). Dendritic Protein Synthesis, Synaptic Plasticity, and Memory. *Cell*. https://doi.org/10.1016/j.cell.2006.09.014

Swanson, G. T., Kamboj, S. K., & Cull-Candy, S. G. (1997). Single-channel properties of recombinant AMPA receptors depend on RNA editing, splice variation, and subunit composition. *Journal of Neuroscience*. https://doi.org/10.1523/jneurosci.17-01-00058.1997

Takumi, Y., Ramírez-León, V., Laake, P., Rinvik, E., & Ottersen, O. P. (1999). Different modes of expression of AMPA and NMDA receptors in hippocampal synapses. *Nature Neuroscience*. https://doi.org/10.1038/10172

Tang, A. H., Chen, H., Li, T. P., Metzbower, S. R., MacGillavry, H. D., & Blanpied, T. A. (2016). A trans-synaptic nanocolumn aligns neurotransmitter release to receptors. *Nature*. https://doi.org/10.1038/nature19058

Tang, W. J., & Gilman, A. G. (1991). Type-specific regulation of adenylyl cyclase by G protein βγ subunits. *Science*. https://doi.org/10.1126/science.1962211

Toni, Nicolas, Buchs, P. A., Nikonenko, I., Povilaitite, P., Parisi, L., & Muller, D. (2001). Remodeling of synaptic membranes after induction of long-term potentiation. *Journal of Neuroscience*. https://doi.org/10.1523/jneurosci.21-16-06245.2001

Topinka, J. R., & Bredt, D. S. (1998). N-terminal palmitoylation of PSD-95 regulates association with cell membranes and interaction with K+ channel K(v)1.4. *Neuron*. https://doi.org/10.1016/S0896-6273(00)80440-7

Van Dort, J. (2018). Aberration correction in STED microscopy. *Doctoral Thesis*.

Veyrac, A., Besnard, A., Caboche, J., Davis, S., & Laroche, S. (2014). The transcription factor Zif268/Egr1, brain plasticity, and memory. In *Progress in Molecular Biology and Translational Science*. https://doi.org/10.1016/B978-0-12-420170-5.00004-0

Vossler, M. R., Yao, H., York, R. D., Pan, M. G., Rim, C. S., & Stork, P. J. S. (1997). cAMP activates MAP kinase and Elk-1 through a B-Raf- and Rap1-dependent pathway. *Cell*. https://doi.org/10.1016/S0092-8674(00)80184-1

Walkup, W. G., Mastro, T. L., Schenker, L. T., Vielmetter, J., Hu, R., Iancu, A., … Kennedy, M. B. (2016). A model for regulation by SynGAP-α1 of binding of synaptic proteins to PDZ-domain “Slots” in the postsynaptic density. *ELife*. https://doi.org/10.7554/elife.16813

Wegner W, Steffens H, Gregor C, Wolf F, W. K. (2020). Environmental enrichment enhances precision and remodeling speed of synaptic nanoarchitecture revealed by crosstalk free two-color in vivo STED nanoscopy. *BioRxiv Preprint*. https://doi.org/10.1101/2020.10.23.352195

Wegner, W., Ilgen, P., Gregor, C., Van Dort, J., Mott, A. C., Steffens, H., & Willig, K. I. (2017). In vivo mouse and live cell STED microscopy of neuronal actin plasticity using far-red emitting fluorescent proteins. *Scientific Reports*, *7*(1). https://doi.org/10.1038/s41598-017-11827-4

Wegner, W., Mott, A. C., Grant, S. G. N., Steffens, H., & Willig, K. I. (2018). In vivo STED microscopy visualizes PSD95 sub-structures and morphological changes over several hours in the mouse visual cortex. *Scientific Reports*, *8*(1), 219. https://doi.org/10.1038/s41598-017-18640-z

Wenthold, R. J., Petralia, R. S., Blahos, J., & Niedzielski, A. S. (1996). Evidence for multiple AMPA receptor complexes in hippocampal CA1/CA2 neurons. *Journal of Neuroscience*. https://doi.org/10.1523/jneurosci.16-06-01982.1996

Westphal, V., Rizzoli, S. O., Lauterbach, M. A., Kamin, D., Jahn, R., & Hell, S. W. (2008). Video-rate far-field optical nanoscopy dissects synaptic vesicle movement. *Science*. https://doi.org/10.1126/science.1154228

Wiesner, T., Bilodeau, A., Bernatchez, R., Deschênes, A., Raulier, B., De Koninck, P., & Lavoie-Cardinal, F. (2020). Activity-Dependent Remodeling of Synaptic Protein Organization Revealed by High Throughput Analysis of STED Nanoscopy Images. *Frontiers in Neural Circuits*. https://doi.org/10.3389/fncir.2020.00057

Willig, K. I., Rizzoli, S. O., Westphal, V., Jahn, R., & Hell, S. W. (2006). STED microscopy reveals that synaptotagmin remains clustered after synaptic vesicle exocytosis. *Nature*. https://doi.org/10.1038/nature04592

Wyllie, D. J. A., Behe, P., Nassar, M., Schoepfer, R., & Colquhoun, D. (1996). Single-channel currents from recombinant NMDA NR1a/NR2D receptors expressed in xenopus oocytes. *Proceedings of the Royal Society B: Biological Sciences*. https://doi.org/10.1098/rspb.1996.0159

Ye, X., & Carew, T. J. (2010). Small G Protein Signaling in Neuronal Plasticity and Memory Formation: The Specific Role of Ras Family Proteins. *Neuron*. https://doi.org/10.1016/j.neuron.2010.09.013

Yu, N. K., Uhm, H., Shim, J., Choi, J. H., Bae, S., Sacktor, T. C., … Kaang, B. K. (2017). Increased PKMζ activity impedes lateral movement of GluA2-containing AMPA receptors. *Molecular Brain*. https://doi.org/10.1186/s13041-017-0334-7

Zhai, R. G., Vardinon-Friedman, H., Cases-Langhoff, C., Becker, B., Gundelfinger, E. D., Ziv, N. E., & Garner, C. C. (2001). Assembling the presynaptic active zone: A characterization of an active zone precursor vesicle. *Neuron*. https://doi.org/10.1016/S0896-6273(01)00185-4

Zhu, J. J., Qin, Y., Zhao, M., Van Aelst, L., & Malinow, R. (2002). Ras and Rap control AMPA receptor trafficking during synaptic plasticity. *Cell*. https://doi.org/10.1016/S0092-8674(02)00897-8

Zhu, J., Shang, Y., & Zhang, M. (2016). Mechanistic basis of MAGUK-organized complexes in synaptic development and signalling. *Nature Reviews Neuroscience*. https://doi.org/10.1038/nrn.2016.18

Ziv, N. E., & Brenner, N. (2018). Synaptic Tenacity or Lack Thereof: Spontaneous Remodeling of Synapses. *Trends in Neurosciences*. https://doi.org/10.1016/j.tins.2017.12.003

Appendix

A1. Effect of repeated imaging on PSD95 assembly area and spine head area

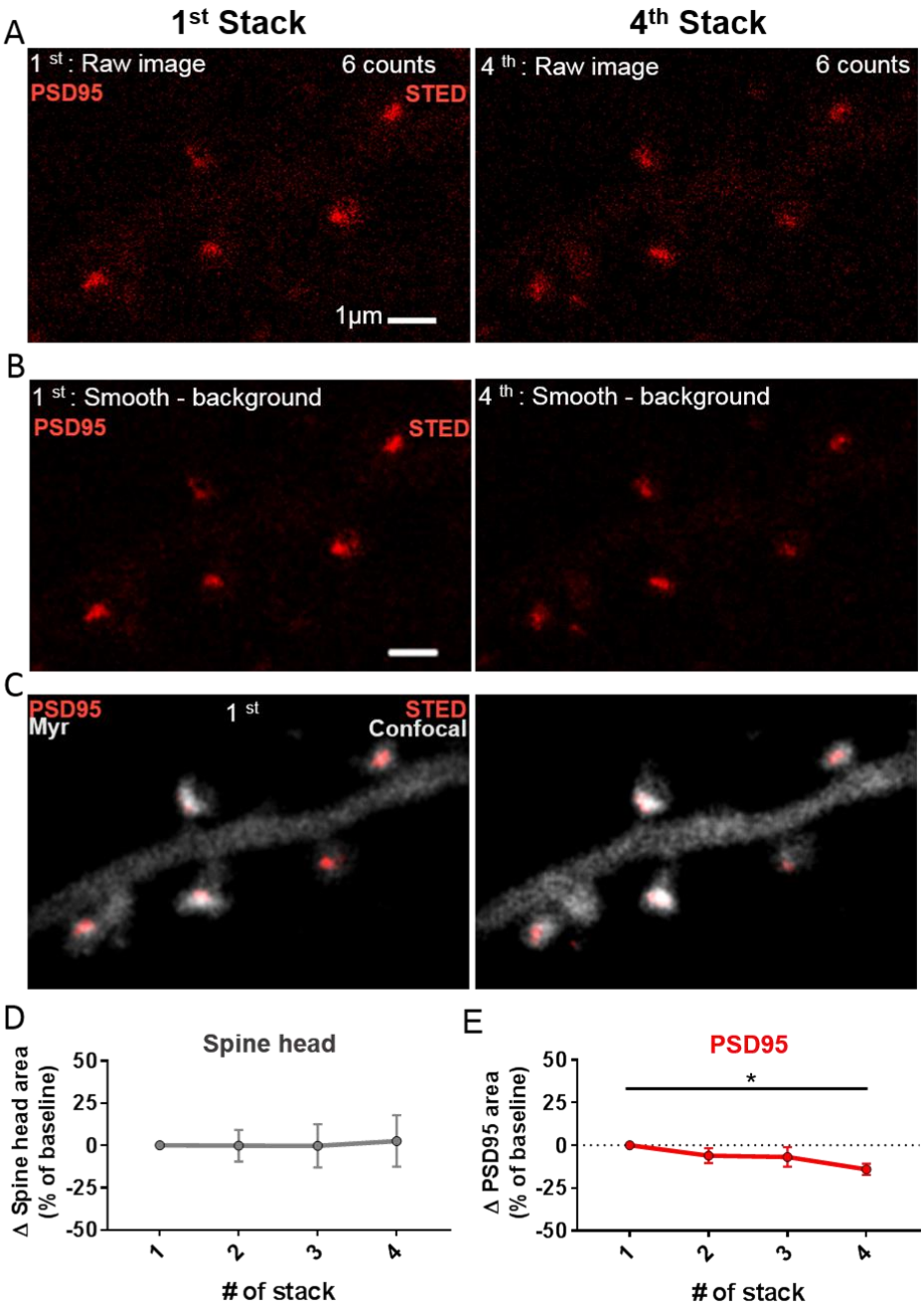

Figure A1. Repeated stack images of PSD95-fingR-Citrine and myr-rsEGFP2 during baseline. (A) Raw image of PSD95-FingR-Citrine at the first and fourth stack image with STED microscopy. Every image was taken at a 30 sec interval during a live-cell imaging of a total of 1.5 minutes in hippocampal organotypic slice. **(B)** Same as (A), but the picture has been smoothed and the background subtracted to improve the contrast. **(C)** Same picture as (B), but merge with the expression of myr-rsEGFP2 (confocal image) to reveal the spine head. **(D)** Change of spine head area after 4 stacks take with STED and confocal imaging. Every image was taken at a 30 sec interval during a live-cell imaging of 1.5 minutes. Data are represented as mean ± SD. **(E)** Same as (D) but for PSD95. Data are represent as mean ± SEM. Friedman test *p=0.017

A2. Area and morphological change of small and large PSD95

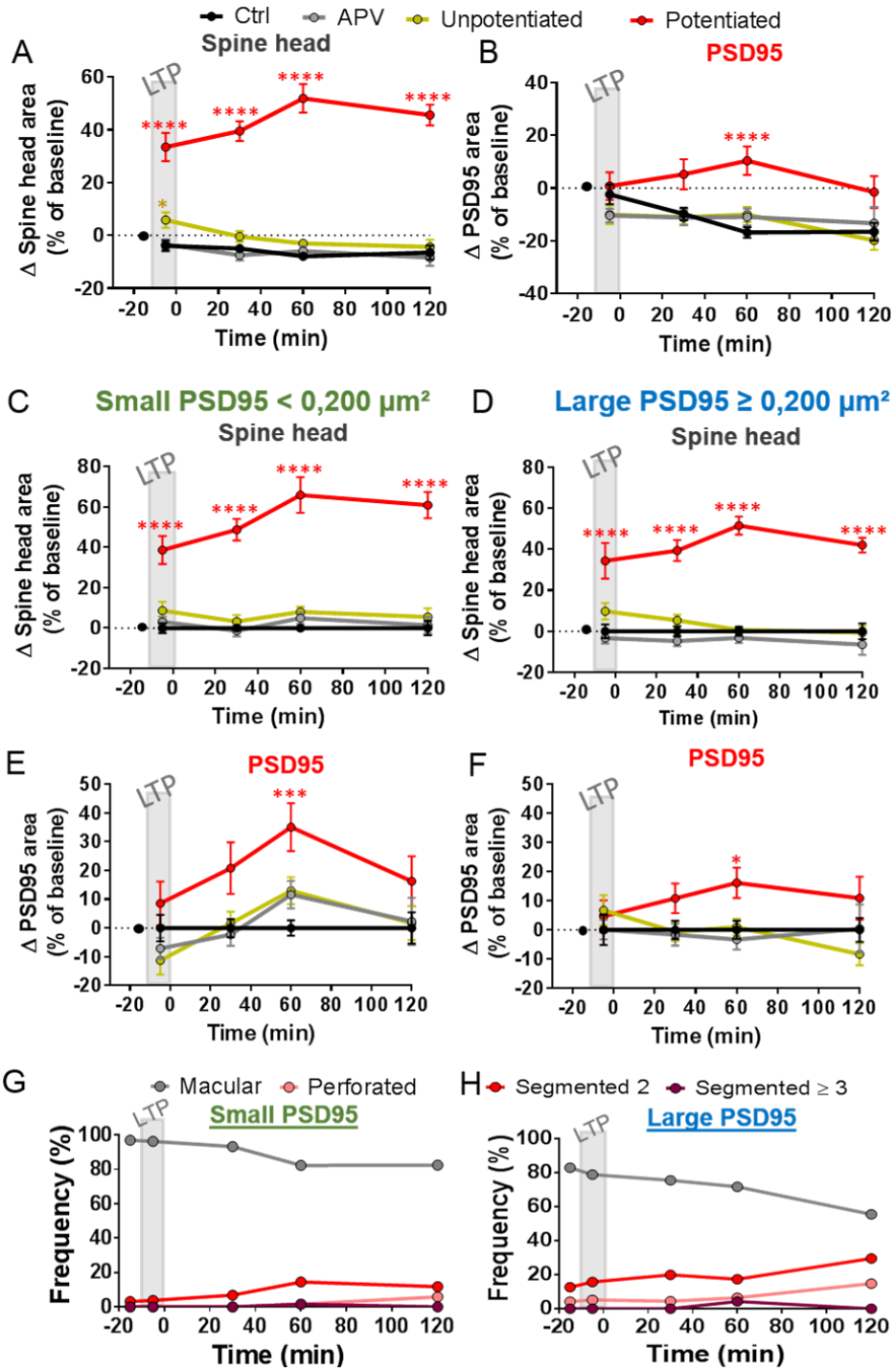

Figure A2. Area change of PSD95 and spine heads after LTP and structural change of small and large PSD95. (A) Mean changes in spine head areas in potentiated, unpotentiated spines and control condition supplement with APV following chemical LTP. Changes were compared to control (not normalize). *K-W test* with *Dunn's* post hoc showed significant differences: ****p< 0.0001. **(B)** Same as (A) but for change in PSD95 area. ****p< 0.0001. **(C)** Same as (A) but for small PSD95 and the area change were normalized to the control. ****p< 0.0001. **(D)** Same as (C) but for large PSD95. ****p< 0.0001. **(E)** Same as (C) but for change of small PSD95 area. ***p= 0.0001. Data A to F are represent as mean ± SEM **(F)** Same as (E), but for larger PSD95. *p= 0.0161. **(G)** Morphological changes of small PSD95 on potentiated spines after LTP stimulation. **(H)** Same as (G) but for larger PSD95. Number of experiments and spines are list in the table A2.

A3. Different PSD95 morphologies with their spine head area, PSD95 area, and filling ratio

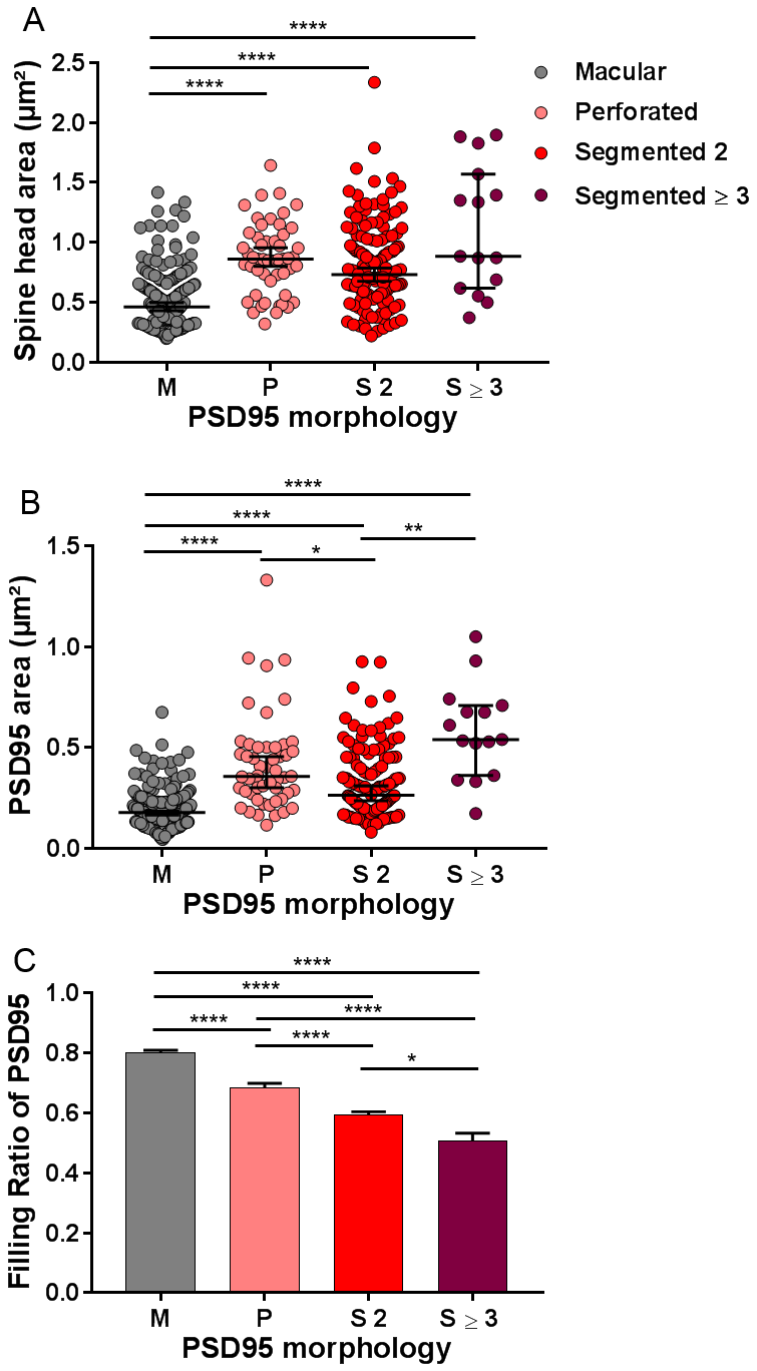

Figure A3. Spine head area, PSD95 area, and filling ratio of different PSD95 morphologies. (A) Spine head area of different PSD95 morphologies. Changes were compared between different PSD95 morphologies. *K-W test* with *Dunn's* post hoc showed significant differences: ****p< 0.0001. **(B)** Same as (A) but for PSD95 area. *p=0.0394, **p=0.0044 and ****p< 0.0001. Data A and B area presented as median ± 95%CI. **(C)** Filling ratio of different PSD95 morphologies. *K-W test* with *Dunn's* post hoc showed significant differences: *p=0.016 and ****p< 0.0001. Data are presented as mean ± SEM

A4. Macro for image analyses of 3 color staining AMPA receptor, PSD95, and phalloidin.

AMPA/PSD95/Phalloidin

```
setBatchMode(true);
input= getDirectory("Choose an input Directory");
output=getDirectory("Choose an output Directory");
run("Bio-Formats Macro Extensions");
ext1=".msr";
ext2="Det1";
ext3="Det2";
ext4="green";
// Run a loop to process image per image
//Open files
list= getFileList(input);
for (i=0; i<list.length; i++) { //Loops over files in folder
path= input + list[i];
if (endsWith(path, ext1)){ //only opens if file is ext
Ext.setId(path);
Ext.getSeriesCount(seriesCount);
for (j=1; j<=seriesCount; j++) {
run("Bio-Formats Importer", "open=["+ path +"] autoscale color_mode=Composite
view=[Hyperstack] stack_order=XYCZT series_"+j);
getDimensions(w, h, channels, slices, frames);

name=getTitle();
if (endsWith(name, ext2)) {
                                                        C1=getTitle();
                        run("Fire");
        run("Smooth", "stack");
        //run("Brightness/Contrast...");
        setMinAndMax(6, 20);
        run("Apply LUT", "stack");
        saveAs("Tiff", output+C1+"_ampa");}
if (endsWith(name, ext3)) {
                                                        C2=getTitle();
                        run("Fire");
        run("Smooth", "stack");
        //run("Brightness/Contrast...");
        setMinAndMax(10, 50);
        run("Apply LUT", "stack");
        saveAs("Tiff", output+C2+"_psd95");}
if (endsWith(name, ext4)) {
                                                        C3=getTitle();
                        run("Red Hot");
        run("Smooth", "stack");
        //run("Brightness/Contrast...");
        setMinAndMax(1, 110);
        run("Apply LUT", "stack");
         run("Smooth", "stack");
        saveAs("Tiff", output+C3+"_spine");}}}}
waitForUser ("Analysis done!!!!");run("Close All");
```

A5. Macro for image analyses of 3 color staining Bassoon, PSD95, and phalloidin

Bassoon/PSD95/Phalloidin

```
setBatchMode(true);
input= getDirectory("Choose an input Directory");
output=getDirectory("Choose an output Directory");
run("Bio-Formats Macro Extensions");
ext1=".msr";
ext2="Det1";
ext3="Det2";
ext4="green";
// Run a loop to process image per image
//Open files
list= getFileList(input);
for (i=0; i<list.length; i++) { //Loops over files in folder
path= input + list[i];
if (endsWith(path, ext1)){ //only opens if file is ext
Ext.setId(path);
Ext.getSeriesCount(seriesCount);
for (j=1; j<=seriesCount; j++) {
run("Bio-Formats Importer", "open=["+ path +"] autoscale color_mode=Composite
view=[Hyperstack] stack_order=XYCZT series_"+j);
getDimensions(w, h, channels, slices, frames);

name=getTitle();
if (endsWith(name, ext2)) {
                                                        C1=getTitle();
                        run("Fire");
        run("Smooth", "stack");
        //run("Brightness/Contrast...");
        setMinAndMax(20, 85);
        run("Apply LUT", "stack");
        saveAs("Tiff", output+C1+"_psd95");}
if (endsWith(name, ext3)) {
                                                        C2=getTitle();
                        run("Fire");
        run("Smooth", "stack");
        //run("Brightness/Contrast...");
        setMinAndMax(20, 110);
        run("Apply LUT", "stack");
        saveAs("Tiff", output+C2+"_basoon");}

if (endsWith(name, ext4)) {
                                                        C3=getTitle();
                        run("Red Hot");
        run("Smooth", "stack");
        //run("Brightness/Contrast...");
        setMinAndMax(0, 15);
        run("Apply LUT", "stack");
        run("Smooth", "stack");
        saveAs("Tiff", output+C3+"_spine");}}}}
waitForUser ("Analysis done!!!!");run("Close All");
```

A6. Imaging parameters

Table A1. Imaging parameters of the figures presented in this thesis

Figure	Pixel size	Field of view	Dwell time	Fluorescence label	Excitation power	STED power	Detection channel
	nm	µm x µm	µs		µW	mW	nm
Figure 2.2.B-C	30	30 x 30	4	Citrine/ rsEGFP	5.5	13	535/50
Figure 2.3.B	20	30 x 30	5	Alexa594/ STAR RED	38 / 18	219	620/14, 692/40
Figure 2.3.C	20	30 x 30	5	Alexa594/ STAR RED	15 / 18	219	620/14, 692/40
Figure 3.1.A-B	30	30 x 30	4	Citrine/ rsEGFP	5.5	14	535/50
Figure 3.2.B	30	30 x 30	4	Citrine/ rsEGFP	5.5	16	535/50
Figure 3.3.A-B	30	30 x 30	4	Citrine/ rsEGFP	5.5	14	535/50
Figure 3.5.A-C	30	30 x 30	4	Citrine/ rsEGFP	5.5	16	535/50
Figure 3.6.A-C	30	30 x 30	4	Citrine/ rsEGFP	5.5	16	535/50
Figure 3.7.A	20	30 x 30	5	Alexa594/ STAR RED	38 / 18	219	620/14, 692/40
Figure 3.7.B	30	30 x 30	5	Alexa594/ STAR RED	3,2 / 13	230	620/14, 692/40
Figure 3.8.A-B	20	30 x 30	5	Alexa594/ STAR RED	38 / 18	219	620/14, 692/40
Figure 3.10.A	20	30 x 30	5	Alexa594/ STAR RED	38 / 18	219	620/14, 692/40
Figure 3.11.A-B	20	30 x 30	5	Alexa594/ STAR RED	15 / 18	219	620/14, 692/40
Figure 3.12.A	20	30 x 30	5	Alexa594/ STAR RED	15 / 18	219	620/14, 692/40
Figure A1.A-C	30	15 x 15	4	Citrine/ rsEGFP	5.5	13	535/50

A7. Number of spines and experiments used for analysis

Table A2. Number of spines and number of experiments for every figure presented in this thesis

Figure	Condition	Times min after LTP	Number of spines n	Number of experiments N
Figure 3.2.C	Control	during LTP, 30, 60, 120	123, 224, 223, 101	5 and 5
	APV	during LTP, 30, 60, 120	153, 229, 201, 84	5 and 8
	Unpotentiated	during LTP, 30, 60, 120	66, 202, 196, 130	10 and 9
	Potentiated	during LTP, 30, 60, 120	46, 106, 111, 65	10 and 9
Figure 3.2.D	Control	during LTP, 30, 60, 120	121, 222, 215, 94	5 and 5
	APV	during LTP, 30, 60, 120	152, 221, 166, 70	5 and 8
	Unpotentiated	during LTP, 30, 60, 120	68, 165, 160, 90	10 and 9
	Potentiated	during LTP, 30, 60, 120	45, 103, 108, 59	10 and 9
Figure 3.2.F	Control	60	216	5 and 5
	Potentiated	60	109	10 and 9
Figure 3.3.C	Unpotentiated	before LTP, 60 min	208, 190	10 and 9
	Potentiated	before LTP, 60 min	109, 108	10 and 9
Figure 3.3.D	Unpotentiated	before LTP, 60 min	208, 190	10 and 9
	Potentiated	before LTP, 60 min	109, 109	10 and 9
Figure 3.4.A	Control	60	179	5 and 5
	Unpotentiated	60	194	10 and 9
	Potentiated	60	59	10 and 9
Figure 3.4.B	Control	60	181	5 and 5
	Unpotentiated	60	202	10 and 9
	Potentiated	60	108	10 and 9
Figure 3.5.B	Control	before, during LTP, 30, 60, 120	230,122, 223, 216, 94	5 and 5
	Potentiated	before, during LTP, 30, 60, 120	109,45,102,109,60	10 and 9
Figure 3.5.C	Control	before, during LTP, 30, 60, 120	230,122, 223, 216, 94	5 and 5
	Potentiated	before, during LTP, 30, 60, 120	109,45,102,109,60	10 and 9
Figure 3.8.D,G	Control	0, 30, 60, 120	188, 199, 222, 188	3
	LTP	0, 30, 60, 120	207, 181, 220, 213	3
Figure 3.9.A-E	Control	0, 30, 60, 120	188, 199, 222, 188	3
	LTP	0, 30, 60, 120	207, 181, 220, 213	3
Figure 3.10.B	Control	0, 30, 60, 120	188, 199, 222, 188	3
	LTP	0, 30, 60, 120	207, 181, 220, 213	3
Figure 3.10.C	Control	0, 30, 60, 120	8, 21, 31, 50	3
	LTP	0, 30, 60, 120	53, 40, 48, 73	3
Figure 3.11.C-F	Control	0, 30, 60, 120	359, 381, 421, 466	4
	LTP	0, 30, 60, 120	339, 310, 424, 371	4
Figure 3.12.B-D	Control	0, 30, 60, 120	359, 381, 421, 466	4
	LTP	0, 30, 60, 120	339, 310, 424, 371	4
Figure A1. D-E			19	4
Figure A2. A-B	Control	during LTP, 30, 60, 120	123, 224, 223, 101	5 and 5
	APV	during LTP, 30, 60, 120	153, 229, 201, 84	5 and 8
	Unpotentiated	during LTP, 30, 60, 120	66, 202, 196, 130	10 and 9
	Potentiated	during LTP, 30, 60, 120	46, 106, 111, 65	10 and 9
Figure A2. C,E,G	Control	during LTP, 30, 60, 120	92, 136, 137, 47	5 and 5
	APV	during LTP, 30, 60, 120	85, 141, 121, 60	5 and 8
	Unpotentiated	during LTP, 30, 60, 120	34, 101, 99, 69	10 and 9
	Potentiated	during LTP, 30, 60, 120	27, 60, 64, 36	10 and 9
Figure A2. D,F,H	Control	during LTP, 30, 60, 120	27, 84, 81, 52	5 and 5
	APV	during LTP, 30, 60, 120	66, 84, 67, 21	5 and 8
	Unpotentiated	during LTP, 30, 60, 120	34, 99, 97, 61	10 and 9
	Potentiated	during LTP, 30, 60, 120	19, 45, 46, 27	10 and 9
Figure A3.A-C		Macular, Perfo., Seg 2, Seg 3	243, 51, 155, 15	42

List of figures

List of tables